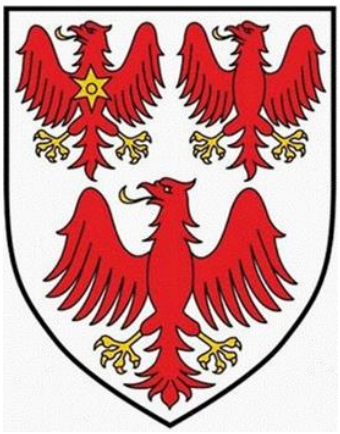
Understanding and Mitigating Metallic Anode Degradation in Divalent Battery Systems





Shengda D. Pu

The Queen's College

Department of Materials

University of Oxford

A thesis submitted for the degree of

Doctor of Philosophy

July 2022

Declaration

This thesis is submitted for the degree of Doctor of Philosophy in Materials Science at the University of Oxford in 2022. This work does not exceed the 30000 word limit and it is original. Any mention of previous work in this thesis has been properly referenced and acknowledged.

- Shengda D. Pu

Acknowledgements

Firstly, I would like to thank both of my supervisors, Sir Peter G. Bruce and Dr. Alex W. Robertson for offering me this great opportunity and for their continuous support and guidance throughout my Ph.D.

Secondly, I want to thank all PGB members and external collaborators who helped me with my Ph.D. projects: Dr. Paul Adamson, Dr. Xiangwen Gao, Dr. Robert House, Dr. Gareth Hartley, Dr. Sixie Yang, Dr. Boyang Liu, Dr. Ziyang Ning, Dr. Dominic Spencer Jolly, Dr. Chen Gong, Dr. John-Joseph Marie, Max Jenkins, Dominic Melvin, Chloe Chau, Liquan Pi, Yi Yuan, Shengming Zhang, Bingkun Hu, Zixuan Li, Dr. Jili Yue, Dr. Yuanbo Tang, Prof. Roger Reed, Prof. James Marrow, and Prof. Jun Luo et al. It has been a pleasure and an honour to work with you. In particular, I would like to thank Xiangwen Gao, Ziyang Ning, and Chen Gong. I thank Xiangwen, for the tremendous help he has selflessly given me ever since I joined PGB, both in academics and in life, and for being the big brother who has always been there for me. I thank Ziyang, for all the exciting experiments, the fun and fruitful discussions we had together, and for being a major source of joy during the gloomiest days of my Ph.D. I thank Chen, for all the valuable and glorious memories we share as research comrades: tackling the liquid-cell TEM, exploring interesting research topics, making our career plan together etc., we make an excellent team! I would also like to thank Zixuan and Bingkun for their tremendous contribution to my last paper.

My gratitude also goes to all my friends who supported me during my Ph.D. at Oxford, especially Xiangwen Gao, Ziyang Ning, Chen Gong, Yi Yuan, Liquan Pi, Shengming Zhang, Bingkun Hu, Mengjiang Lin, and Chloe Chau for being my best friends at PGB. I am very lucky to

have you guys in my life and I will always cherish our friendship. Special thank also goes to my buddy Jiajie Yang, for being an awesome friend and for all his help during the past few years. Finally, I would like to thank my wife Mandy, and my parents, I could never complete this journey without their support and love.

Abstract

The work in this thesis focuses on the metallic anode in two of the divalent battery systems: aqueous zinc batteries and calcium-ion batteries. By performing systematic studies, we aim to provide a deep understanding of their anode degradation mechanisms:

In **Chapter 3**, I looked at the aging-induced degradation in $ZnSO_4$-based aqueous zinc batteries. It was found that aging can lead to significant anode capacity loss, in some cases over 70% efficiency loss after only 24 hours. We assessed such loss with respect to various factors: aging time, anode loading, cycling rates etc. and investigated the root causes of such aging-induced capacity loss using in-situ Computed X-Ray Tomography. A paper based on this chapter, 'Decoupling and Quantifying Aging-Induced Zn Anode Degradation Processes in Aqueous Zinc Batteries' has been submitted to ***Joule*** and is now under review.

In **Chapter 4**, I explored a possible strategy to mitigate the dendrite problem in the $ZnSO_4$-based aqueous zinc batteries. By using a single-crystal (002) Zn as an ideal model anode, I promoted planar Zn deposition and defect-suppression, which largely resolved the dendrite problem and allowed excellent cell performance at high-rate and long-cycle conditions. A paper based on this chapter, 'Achieving Ultra-High Rate Planar and Dendrite-Free Zinc Electroplating for Aqueous Zinc Battery Anodes' has been published in ***Advanced Materials***.

In **Chapter 5**, I systematically studied and visualized the plating and stripping process in the $Ca(BH_4)_2$-based calcium-ion battery electrolyte using in-situ TEM. I revealed that despite calcium deposition being mostly globular, calcium dendrite formation can still occur as a result of high current density. In addition, the inhomogeneous CaH_2 layer formation can also lead to

the formation of localized ‘hot spots’ , which can induce unexpected dendrite formation at lower current densities. Two papers based on this chapter, ‘Liquid cell transmission electron microscopy and its applications’ and ‘Current-density-dependent electroplating in Ca electrolytes: From globules to dendrites’, has been published in ***Royal Society open science*** and ***ACS Energy Letters.***

Publication List

First-author Publications:

1. S D Pu†, C Gong†, A W Robertson (2020) 'Liquid cell transmission electron microscopy and its applications', ***Royal Society open science*** 7 (1), 191204. (**Chapter 2&5**)

2. S D Pu†, C Gong†, X Gao, Z Ning, S Yang, J Marie, B Liu, R A House, G O Hartley, J Luo, P G Bruce, A W Robertson (2020) 'Current-density-dependent electroplating in Ca electrolytes: From globules to dendrites', ***ACS Energy Letters*** 5 (7), 2283-2290. (**Chapter 5**)

3. C Gong†, S D Pu†, X Gao, S Yang, J Liu, Z Ning, G J Rees, I Capone, L Pi, B Liu, G O Hartley, J Fawdon, J Luo, M Pasta, C R M Grovenor, P G Bruce, A W Robertson (2021) 'Revealing the Role of Fluoride-Rich Battery Electrode Interphases by Operando Transmission Electron Microscopy', ***Advanced Energy Materials*** 11 (10), 2003118.

4. C Gong†, S D Pu†, A W Robertson (2021) 'In Situ Transmission Electron Microscopy for Studying Lithium-Ion Batteries', ***Advances in Sustainable Energy*** *(Book Chapter)*, 545-569.

5. S D Pu†, C Gong†, Y T Tang, Z Ning, J Liu, S Zhang, Y Yuan, D Melvin, S Yang, L Pi, J Marie, B Hu, M Jenkins, Z Li, B Liu, S C E Tsang, T J Marrow, R C Reed, X Gao, P G Bruce, A W Robertson (2022) 'Achieving Ultra-High Rate Planar and Dendrite-Free Zinc Electroplating for Aqueous Zinc Battery Anodes', ***Advanced Materials***, 2202552. (**Chapter 4**)

6. S D Pu†, B Hu†, Z Li†, Y Yuan, C Gong, Z Ning, C Chau, S Yang, S Zhang, L Pi, Y T Tang, J Yue, T J Marrow, X Gao, P G Bruce, A W Robertson (2022) 'Decoupling and Quantifying Aging-Induced Zn Anode Degradation Processes in Aqueous Zinc Batteries' ***Joule*** (Accepted) (**Chapter 3**)

7. C Gong†, S D Pu†, S Zhang†, Y Yuan†, Z Ning, S Yang, X Gao, J Liu, L Pi, B Liu, I Capone, B Hu, D Melvin, M Pasta, C R M Grovenor, P G Bruce, A W Robertson (2022) 'The role of an elastic interphase in suppressing gas evolution and promoting uniform electroplating in sodium metal anodes' ***Energy & Environmental Science*** (Accepted)

Co-author Publications:

1. J Mo, E C M Barbosa, S Wu, Y Li, Y Sun, W Xiang, T Li, S D Pu, A W Robertson, T Wu, Y Soo, T V Alves, P H C Camargo, W Kuo, S C E Tsang (2021) 'Atomic-Precision Tailoring of Au–Ag Core–Shell Composite Nanoparticles for Direct Electrochemical-Plasmonic Hydrogen Evolution in Water Splitting', ***Advanced Functional Materials,*** 2102517.

2. Z Ning, D S Jolly, G Li, R D Meyere, S D Pu, Y Chen, J Kasemchainan, J Ihli, C Gong, B Liu, D L R Melvin, A Bonnin, O Magdysyuk, l Adamson, G O Hartley, C W Monroe, T J Marrow, P G Bruce (2021) 'Visualizing plating-induced cracking in lithium-anode solid-electrolyte cells' ***Nature Materials*** 20 (8), 1121-1129.

3. X Xu, L Pi, J Marie, G J Rees, C Gong, S D Pu, R A House, A W Robertson, P G Bruce (2021) 'Li2NiO2F a New Oxyfluoride Disordered Rocksalt Cathode Material', ***Journal of The Electrochemical Society*** 168 (8), 080521.

4. D S Jolly, D L R Melvin, I D R Stephens, R H Brugge, S D Pu, J Bu, Z Ning, G O Hartley, P Adamson, P S Grant, A Aguadero, P G Bruce, (2022) 'Interfaces between Ceramic and Polymer Electrolytes: A Comparison of Oxide and Sulfide Solid Electrolytes for Hybrid Solid-State Batteries', ***Inorganics*** 10 (5), 60.

5. D S Jolly, J Perera, S D Pu, D L R Melvin, P Adamson, P G Bruce (2022) 'High Critical Currents for Dendrite Penetration and Voiding in Potassium Metal Anode Solid-State Batteries' ***Journal of Solid-State Electrochemistry***

6. Z Ning, G Li, D Melvin, Y Chen, D S Jolly, J Liu, J Bu, J Perera, C Gong, X Gao, S D Pu, S Zhang, B Hu, G Hartley, A Bodey, R Todd, P Grant, D Armstrong, T J Marrow, C Monroe, P G Bruce, (2022) 'Dendrite Initiation and Propagation in Lithium Metal Solid-State Batteries', ***Nature*** (Accepted)

7. X Gao, C Doerrer, B Hu, S Zhang, L Pi, S D Pu, Y Yuan, L Wang, D S Jolly, D Melvin, A W Robertson, P S Grant, P G Bruce, (2023) 'A Li6PS5Cl based solid-state cathode with high capacity, high-capacity retention and cycling efficiency at a low pressure' (under review)

8. J J Marie, J Chen, S D Pu, A W Robertson, R A House, P G Bruce, (2023) 'Room temperature, solid-state Ca-ion exchange in Na0.67Mn¬0.72Mg0.28O2' (under review)

9. B Liu, X Gao, S D Pu, C Doerrer, D S Jolly, R House, D Melvin, P Adamson, P S Grant, P G Bruce, (2023) 'The effect of volume change and stack pressure on solid-state battery cathodes' (under review)

List of Abbreviation

LIB	lithium-ion battery
NMC	nickel, manganese, cobalt oxide
LCO	lithium cobalt oxide
SEI	solid-electrolyte interphase
AZB	aqueous zinc battery
S.H.E	hydrogen standard electrode
SS	stainless Steel
XRD	X-ray Diffraction
SEM	scanning electron microscopy
EDS	energy dispersive X-ray spectroscopy
XPS	X-Ray photoelectron spectroscopy
KE	kinetic energy
BE	binding energy
WF	work function
MS	mass spectroscopy
AFM	Atomic force microscopy
FIB	Focused ion beam
EBSD	Electron backscatter diffraction
XCT	X-ray computed tomography
ZHS	zinc hydroxide sulfate hydrate
ZHO	Zinc hydroxide
CE	Coulombic efficiency

Table of Contents

Declaration i
Acknowledgements ii
Abstract iv
Publication List vi
First-author Publications: vi
Co-author Publications: vii
List of Abbreviation viii
1 Introduction & Literature Review ..... - 1 -
1.1 Lithium ion battery and its limitations ..... - 1 -
1.1.1 Lithium ion battery's brief history and current status ..... - 1 -
1.1.2 Lithium Ion Battery's Current Status ..... - 2 -
1.1.3 Challenges faced by LIBs ..... - 2 -
1.1.4 Multivalent battery systems as LIB alternatives ..... - 6 -
1.2 Aqueous zinc battery systems ..... - 9 -
1.2.1 Current Status of aqueous zinc battery research ..... - 9 -
1.2.2 Cathode for aqueous zinc battery ..... - 10 -
1.2.3 Anode for aqueous zinc battery ..... - 11 -
1.3 Anode degradation in neutral/mildly acidic AZBs ..... - 13 -
1.3.1 Corrosion ..... - 13 -
1.3.2 Hydrogen evolution ..... - 14 -
1.3.3 Zinc dendrite formation ..... - 15 -
1.3.4 Strategies for mitigating Anode degradation and their limitations ..... - 16 -
1.4 Calcium Battery Systems ..... - 21 -
1.4.1 Calcium Battery's Brief History ..... - 21 -
1.4.2 Achieving Reversible Metallic Ca Anode ..... - 22 -
1.4.3 Alternative anode options for calcium batteries ..... - 23 -
1.4.4 Cathode options for calcium batteries ..... - 24 -
1.4.5 Other calcium-ion-based battery systems ..... - 26 -
2 Experimental ..... - 28 -
2.1 Common Characterization Techniques for Batteries ..... - 28 -
2.1.1 Electrochemical Tests (Galvanostatic Cycling and Cyclic Voltammetry) ..... - 28 -
2.1.2 X-Ray diffraction (XRD) ..... - 31 -

2.1.3 Scanning Electron Microscopy (SEM), Electron Backscatter Diffraction (EBSD) & Energy Dispersive X-ray Spectroscopy (EDS) ..... - 32 -
2.1.4 X-Ray photoelectron spectroscopy (XPS) ..... - 34 -
2.1.5 Online Mass Spectroscopy (MS) ..... - 36 -
2.1.6 Atomic Force Microscopy (AFM) ..... - 36 -
2.2 Advanced Characterization Techniques for Battery Studies ..... - 37 -
2.2.1 FIB, Ion polishing machine ..... - 37 -
2.2.2 X-Ray Computed Tomography (XCT) ..... - 37 -
2.2.3 Liquid Cell Transmission Electron Microscopy (TEM) ..... - 38 -
3 Characterizing aging-induced anode degradation in aqueous zinc batteries ..... - 44 -
3.1 A Brief Background on AZB aging ..... - 44 -
3.2 Experimental conditions ..... - 45 -
3.2.1 Material Preparation ..... - 45 -
3.2.2 Coin Cell Assembly ..... - 45 -
3.2.3 X-section SEM and EDS ..... - 46 -
3.2.4 X-ray photoelectron spectroscopy (XPS) ..... - 47 -
3.2.5 XRD ..... - 47 -
3.2.6 Online Mass Spectroscopy ..... - 47 -
3.2.7 X-ray Computed Tomography ..... - 48 -
3.2.8 Degassing test ..... - 49 -
3.3 Results and Discussion ..... - 49 -
3.3.1 Quantifying anode capacity loss with respect to aging time, current density and separator ..... - 49 -
3.3.2 Identifying and quantifying capacity loss due to ZHS/ZHO formation ..... - 54 -
3.3.3 Identifying the formation of aging-induced 'inactive Zn' ..... - 58 -
3.3.4 Quantifying capacity loss due to aging-induced 'inactive Zn' formation ..... - 60 -
3.3.5 Decoupling and quantifying different aging-induced degradation processes ..... - 61 -
3.3.6 Uncovering the formation mechanism of aging-induced 'inactive Zn' ..... - 63 -
3.3.7 Reactivating the 'inactive Zn' by removing the built-up gas ..... - 67 -
3.3.8 Aging-induced degradation project summary and future work ..... - 68 -
4 Achieving ultrahigh-rate planar and dendrite-free zinc electroplating for aqueous zinc battery anodes ..... - 70 -
4.1 A Brief Background on the dendrite formation problem and related strategies in AZBs ..... - 70 -
4.2 Experimental conditions ..... - 71 -

4.2.1 Material Preparation ..... - 71 -
4.2.2 Two-electrode beaker cell assembly ..... - 72 -
4.2.3 SEM and EDS ..... - 73 -
4.2.4 EBSD of post-plating/cycling anode surface ..... - 73 -
4.2.5 FIB milling coupled with EBSD to study mergence interface ..... - 74 -
4.2.6 X-ray photoelectron spectroscopy (XPS) ..... - 74 -
4.2.7 XRD ..... - 74 -
4.2.8 Fourier Transformation Infrared Spectra (FTIR) ..... - 75 -
4.2.9 Atomic Force Microscopy (AFM) ..... - 75 -
4.2.10 Online Mass Spectroscopy ..... - 75 -
4.2.11 X-ray Computed Tomography ..... - 75 -
4.3 Results and Discussion ..... - 76 -
4.3.1 The limitations of semi-matched substrates and heterogenous deposition interface ..... - 76 -
4.3.2 The viability of using Single-Zn to Incentivize planar (002) Zn growth ..... - 78 -
4.3.3 Electrodeposition quality of planar Zn on Single-Zn anode ..... - 80 -
4.3.4 Achieving planar Zn deposition under high rate and capacity conditions ..... - 81 -
4.3.5 Testing the limit of planar Zn deposition under ultra-high-rate conditions ..... - 83 -
4.3.6 Zn islands mergence via perfect lattice stitching ..... - 85 -
4.3.7 Single-Zn anode's cycling performance ..... - 88 -
4.3.8 Single-Zn anode's post-plating aging performance ..... - 92 -
4.3.9 Possible scalable Single-Zn production by electroplating ..... - 94 -
4.3.10 Planar & dendrite-free Zn anode project summery ..... - 99 -
5 Systematic study of Ca electroplating behaviors ..... - 100 -
5.1 A Brief Background on the Ca ion batteries ..... - 100 -
5.2 Experimental Conditions ..... - 101 -
5.2.1 Electrolyte preparation and quality check ..... - 101 -
5.2.2 Liquid-Cell TEM for in-situ visualization ..... - 102 -
5.2.3 Three-electrode cell for plating & cycling for ex-situ studies ..... - 104 -
5.2.4 SEM & EDS ..... - 104 -
5.2.5 XRD ..... - 104 -
5.2.6 Mass Spectroscopy ..... - 104 -
5.3 Results and Discussion ..... - 105 -
5.3.1 The change of plating morphology over cycling ..... - 105 -

5.3.2 Calcium dendrite formation at high current density ..... - 106 -
5.3.3 Calcium globular plating at medium and low current densities ..... - 111 -
5.3.4 Current density dependent globular-to-dendritic plating morphology transition ..... - 113 -
5.3.5 Dendrite formation at lower current densities ..... - 115 -
5.3.6 Quantifying the CaH_2 SEI formation process ..... - 117 -
5.3.7 Ca electroplating systematic study project summary ..... - 119 -
6 Perspectives and Future Work ..... - 120 -
7 Bibliography ..... - 121 -

1 Introduction & Literature Review

The increasing demand for less greenhouse gas emission and for a sustainable future has been driving the exploration of greener energy resources and the development of more efficient energy storage systems. And in the center of this wave of pursuit for a large-scale energy storage solution lies the most promising candidate – battery.

1.1 Lithium ion battery and its limitations

1.1.1 Lithium ion battery's brief history and current status

Ever since that the electricity-generating electrochemical phenomenon was discovered, various types and versions of battery cells have been proposed since the early 19th century, including famous ones like the pioneering Voltaic Pile, the Lead acid battery, the Leclanche cell, the Nickel-Cadmium battery, the Edison battery etc. [1][2] And over the course of experimenting to find the battery system with ideal performance, the lithium ion battery (LIB) seems to have demonstrated its dominance in this century-long contest over other battery systems, with a good balance of high energy density, the ability to be recharged, and long life-time. [2][3]

The development of Li-based battery systems can be traced back to 1912, pioneered by the famous Gilbert Newton Lewis. [4] But it was not until more than half a century later that the first lithium-ion primary battery became commercially available. And the first reversible (i.e. secondary) LIB only became commercialized towards the end of the century in 1991 by Sony. [5]

1.1.2 Lithium Ion Battery's Current Status

A modern LIB has three key components: 1. A cathode material which can store Li ions in the discharged state, typical ones include $LiFePO_4$, $LiCoO_2$ and the NMC (Ni, Mn, Co) family; 2. An anode which can host Li atoms in the charged state, this can be done via different mechanisms like intercalation (graphite, $Li_4Ti_5O_{12}$) and alloying (Si); 3. Electrolyte that allows Li ion transport between the two electrodes during charging and discharging. [6][7]

Typical commercial LIBs can have energy density of over 200 Wh kg^{-1} (e.g. when couple with NMC cathode), this is significantly higher than the other common battery systems (Ni-Cd: 40-60 Wh kg^{-1}; Lead-Acid: 25-30 Wh kg^{-1}). They can also be easily cycled for thousands of cycles while maintaining a large portion of their original capacity. [1][3][6] Therefore, LIB is an excellent candidate for applications with high energy density and cycling stability requirements like portable devices and electric vehicles.

1.1.3 Challenges faced by LIBs

Despite having relatively well-balanced battery performance, LIB's existing status can hardly fulfill the needs from the world's pressing urge for a fully electrified future, in which batteries will not only be used for powering consumer electronics and automobiles as of today but will also be used for grid-level energy storage systems and all types of machines and modes of transports, including aviation and marine applications. And such a high expectation for batteries have raised many challenges for the existing LIB systems: [6][8]

First is LIB's energy density. While it is sufficient for most consumer electronics applications, its current energy density is not quite as satisfactory when applied on automobiles. Despite a decade of effort to improve its energy density, the battery pack is still the heaviest component on the EV. For example, a 2021 Tesla Mid-Range Model 3 weighs approx. 1780 kg, out of which battery takes 435 kg (~25%). And

to accommodate such a big battery weight while not making the EV too heavy (heavy weight will negatively impact range and performance), EV manufacturers have to make other car components lighter. This is usually jointly done by structural redesign and by using lighter materials like aluminum and plastics, which can potentially lead to compromised driving experience or even safety risks. In addition, this nearly half-a-tone battery pack powers the car for approx. 264 miles, a range value that, despite being sufficient for most users' day-to-day activities, is far from the range normally provided by a diesel/petrol car, not to mention its decay after aging and cycling. There is a clear need to improve battery's energy density to further optimize EVs' performance and reliability and to meet the requirement for possible future electrification of other modes of transportations like airplanes. However, the development of higher energy density battery has been stagnant since 2005, as shown in Figure 1.1.2.1. The goal of having 300 Wh/kg energy density has yet to be reached in LIBs without compromising other key performance metrics. This bottleneck is mostly due to the limitation brought by the fundamental properties of the materials used in LIBs.

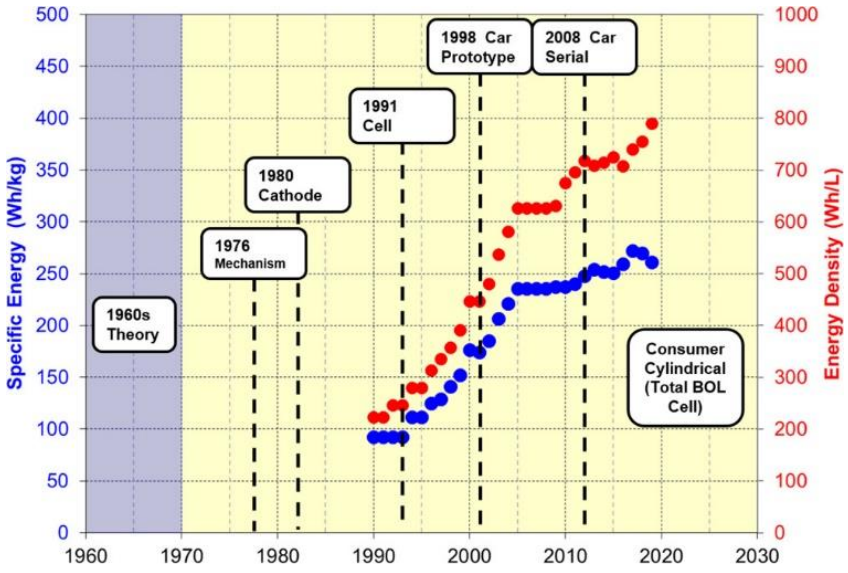


Figure 1.1.3.1 *Historical developments in LIB and consumer cylindrical cell-specific energy. Reprinted with permission, copyright American Chemical Society* [8]

$$\text{battery energy density} = \frac{\text{full battery cell's capacity} \times \text{nominal discharge voltage}}{\text{full battery cell's total volume (or weight)}} \qquad \text{(Equation 1.1.3.1)}$$

Equation 1.1.3.1 shows the factors contributing to the overall energy density of a battery. It can be seen that to achieve a high battery energy density, we can either decrease the denominator or increase the numerator of the equation. To decrease the denominator, we will need to minimize the inactive material components' content (electrolyte, separator, casing etc.), which has already been largely optimized by industry over the years, leaving minimal room for further reduction. Therefore, most researches have been focusing on increasing the numerator of the equation. This is a very material-dependent optimization which can be explored from either the cathode side or the anode side. Cathode researches have focusing on exploring materials with wide charge/discharge voltage window and increasing the elemental ratio of electrochemical active redox couples (e.g. $Co^{3+/4+}$, $Ni^{3+/4+}$ and anion redox). However, these explorations are currently largely impeded by problems like electrolyte decomposition, gas molecule formation and poor cathode structure integrity; for example, further increasing the Ni/Co proportion beyond the 811-NMC will lead to rapid cathode's degradation. These problems detrimentally compromise batteries' cycling performance. [8][9]

The anode side optimization is also deemed to be challenging. The commonly used graphite, despite allowing excellent reversibility for Li intercalation and deintercalation, only has a relatively low capacity (372 mAh g^{-1}). Many researchers have being focusing on adopting a pure Li metallic anode, i.e. making anode-free cells. The metallic Li anode has substantially higher capacity of 3860 mAh g^{-1}, however, its high reactivity has led to multiple problems like rapid electrolyte reaction and depletion, dendrite formation which lead to poor performance and safety issues. And despite various approaches proposed over the years, including artificial SEI, electrolyte modification, solid-state electrolyte etc. so far none of them could allow a metallic Li anode to have a comparable level of cycling stability as the graphite anode in order to be commercialized. [10][11][12][13][14]

The second problem of LIBs is their cost and materials scarcity. There has been a growing concern that the current LIB production level cannot meet the world's growing demand. This concern not only rise from the rapid electrification of automobiles in the past decade but is also a result of the expectation that batteries will be used as grid scale energy storage systems to store the energy harvested from cleaner energy sources (solar, wind, tide etc.). However, the production of LIBs is largely limited by lithium. It has limited reserves and its geographic distribution also suggests that its mining process is heavily geopolitically affected and therefore will likely lead to supply instability and price volatility. And for high energy cathode materials like NMC and LCO (lithium cobalt oxide), cobalt also possesses very high cost due to its low reserves and geographic distribution. Before we can find a cheap element to perfectly replace cobalt's role in high energy cathodes, its price will continue to increase due to its shortage. [7][8]

The third problem of LIBs is its safety. Li, being one of the most reactive metals on earth, can potentially combust upon contact with water or even air, and most organic electrolytes used in LIBs are also highly flammable. Either dendrite-induced/mechanically induced shorting or simply overheating could lead to thermal runaway in LIBs, a rapid exothermic process that can lead to rapid battery and device failure or worse, even fires and explosion. This can be a big risk for all applications, from consumer electronics to EV and large-scale energy storage. [11][15][16][17]

Apart from these three main issues, other commonly raised issues of LIBs include: inability for ultra-fast charging; largely compromised performance at low temperatures; cycling life and calendar life not long enough for long-term applications etc. Some of these problems are due to the intrinsic properties of the LIBs and cannot be easily addressed in the near future. [3][6][8] So rather than only relying on LIB optimization research and hope these problems can be solved, other replacement battery systems have

been proposed and developed by many researchers to solve some of these problems and to fill the large demand-supply gap left by the LIBs. [18][19][20][21][22]

1.1.4 Multivalent battery systems as LIB alternatives

It must be acknowledged that some of LIBs' shortcomings arise from its intrinsic nature which cannot be easily resolved. But these shortcomings are not necessarily applicable to other alternative battery systems, including those that utilize alternative elements, rather than Li ions, as charge carriers within the cell. These alternative systems can be further divided into monovalent metallic elements like sodium and potassium and multivalent elements like zinc and aluminum. These alternative elements are usually more abundant than lithium and therefore should have lower cost. [18][19][21][22][23]

While monovalent systems like sodium and potassium are cheaper, their cycling behaviors are quite similar to that of LIBs, and in many cases worse than LIBs, especially on the anode side. [20][23][24] For example, graphite, the most stable and commonly used anode material for LIBs, cannot be used in sodium ion batteries since it is thermodynamically unfavorable for sodium ions to intercalate between the graphite layers. [25][26] And these alternative monovalent systems cannot employ metallic anodes either, due to dendrite formation, continuous SEI formation and rapid electrolyte consumption, offering them little performance advantage over LIBs. [21][24][27][28][29]

On the other hand, battery systems based on multivalent elements are not only more abundant thus cheaper than lithium, but they are also generally believed to be safer since they are less reactive and are believed to be more compatible with metallic anodes [18][19][23][30][31][32][33], which, as mentioned previously, possess higher specific capacity than other anode materials. Such claimed compatibility is mainly due to two factors: firstly, multivalent systems are reported to be much less prone to dendrite formation during electroplating and cycling [19][32][33], largely mitigating the short-circuiting induced

safety issue and the compromised reversibility due to dendrite detachment; secondly, unlike Li, some of the multivalent systems' metallic anode suffers from less surface reaction and forms minimal SEI during cycling.[21][19]p This is believed to be because that these metals are less reactive than Li, and they are electroplated in a more uniform morphology than Li, giving rise to a flatter anode surface, which is less prone to side reactions and electrolyte depletion.

The most widely studied multivalent systems are magnesium, calcium, aluminum and zinc. Their metallic anodes often have higher specific capacity than lithiated graphite. Even on a full cell level, these systems usually exhibit excellent overall volumetric energy density higher than that of the existing LIBs systems despite having smaller potential windows[19][18][22][32][34][35][36], as shown in Figure 1.1.4.1:

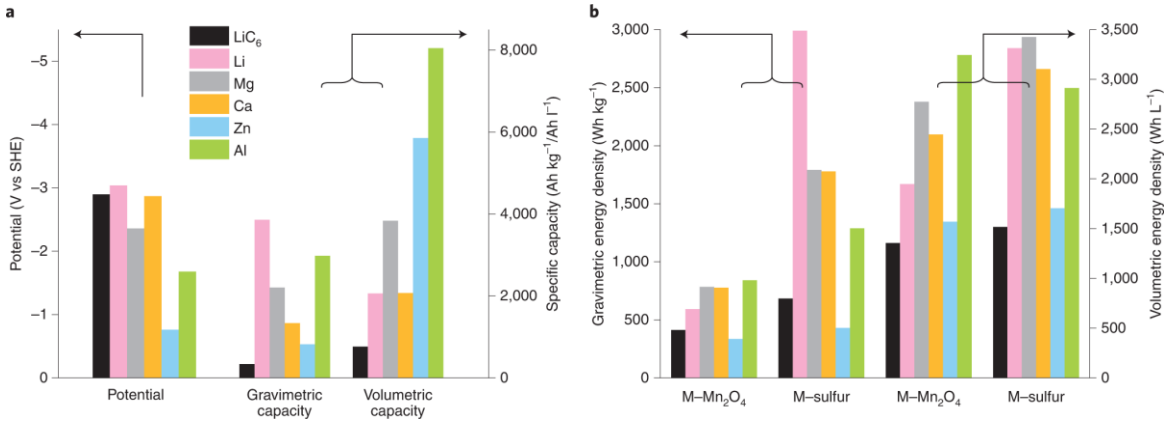


Figure 1.1.4.1 *Electrochemical characteristics comparison. a: Redox potential and gravimetric and volumetric specific capacities of lithiated graphite (LiC_6), lithium and the multivalent metals magnesium, calcium, zinc and aluminum; b: Theoretical gravimetric and volumetric specific energies of batteries with metal and LiC_6 anodes (M) and spinel Mn_2O_4 or sulfur cathodes calculated based on the weight of the cathode and the anode active materials. Reprinted with permission, copyright Nature* [35]

The combined advantages of high safety and high energy density makes these systems promising candidates as alternatives to existing LIBs. However, these systems are not as well studied and developed as the LIBs. Much of their battery behaviors, including cycling mechanism, degradation mechanism, kinetics etc. are significantly different to LIBs', and yet remain largely unexplored[18][22][34][35][37]. And there is an increasing need for this knowledge gap to be filled for future multivalent battery development, optimization, and commercialization.

This thesis focuses on aqueous zinc batteries and calcium batteries as sample systems with the aim to generate a better understanding of the multivalent metallic anodes' behavior during cycling in general. The aqueous zinc system is chosen since it is deemed by many to be the most promising candidate as the future grid-scale energy storage system since its water-compatible nature makes it safer and cheaper, unparalleled by other common multivalent systems. [38][39][40] The calcium system is chosen for its highly negative redox potential and high energy density, both of which comparable to those of LIBs, making it a good candidate as LIB alternative. Also, the reversible metallic calcium anode has only been made possible in the past five years [32][33][41][42], and its behavior has remained the least understood among all the multivalent systems. In addition, unlike magnesium and aluminum battery systems [19][43], whose electrochemical performance largely relies on the presence of Cl^- ions, which can lead to the accelerated corrosion of the batteries' metallic components [44] (casing, current collectors, etc.), the reported zinc and calcium systems can achieve outstanding performance with Cl^- free electrolytes and are therefore more commercially viable.

1.2 Aqueous zinc battery systems

Despite having relatively low energy density, zinc battery system shows the best water and oxygen tolerance among all battery systems (both monovalent or multivalent systems), which along with its low redox potential window, makes it the only battery system with metallic anode stable enough to be used directly in the aqueous solutions. [38][39][40] Aqueous zinc batteries are therefore much safer and easier to make and to recycle. In addition, AZBs do not employ high-cost organic electrolytes or scarce elements like lithium and cobalt in their cathodes, which means that their future production can be kept at a low-cost and free from geopolitical volatility even when produced at a very large scale. This makes them the perfect candidate for grid-scale energy storage systems which need to be safe and low-cost yet generally do not require low weight or high energy density. In addition, some aqueous Zn electrolytes can have up to two orders of magnitude higher ionic conductivity than most organic systems, which makes AZBs more compatible with high-rate charging/discharging conditions.

1.2.1 Current Status of aqueous zinc battery research

Conventional AZBs, like the Zn-Ni system, have historically used alkaline aqueous electrolyte systems. Despite having reasonable capacity, alkaline electrolytes are not very compatible with metallic Zn anodes, tending to suffer from problems like dendrite formation, shape deformation and surface passivation induced by oxide and hydroxide formation, which usually lead to short-circuiting and poor reversibility upon cycling. [45][46][47]

However, the research advancement in neutral or mildly acidic AZB electrolytes have sparked a new wave of interest in AZB research.[36][48][49] Despite having a smaller electrochemical window and thus lower energy density, AZBs with neutral or mildly acid electrolytes has demonstrated much improved reversibility than their alkaline counterparts. Various salts have been proposed to be used in AZB

electrolytes, including $ZnSO_4$, $ZnCl_2$, ZnF_2, $Zn(ChO_4)_2$, $Zn(NO_3)_2$, $Zn(CH_3COO)_2$, $(Zn(CF_3SO3)_2)$, $(Zn(TFSI)_2)$ etc. Electrolytes based on $ZnSO_4$, $(Zn(CF_3SO_3)_2)$ and $(Zn(TFSI)_2)$ are the most popular ones among researchers due to their reportedly high reversibility, stability and low corrosivity.[50][36][51][52][53][54][55][56][57] And in particular, $ZnSO_4$ has been given extra attentions due to its simpler structure and lower cost.

In addition to the alkaline or acidic electrolyte systems, hybrid cells with cathodes in alkaline electrolytes and anodes in acidic electrolytes have also been proposed as a strategy to improve power density of AZBs, yet their complex design and difficulty to handle have made them less commercially practical in the short term. [58]

1.2.2 Cathode for aqueous zinc battery

Out of all the multivalent systems, the zinc battery system is the most studied one, and many materials have been proposed as its potential cathode, which can be categorized into three types: 1. The manganese oxide family is so far the most studied potential cathode system for AZBs. Various structured MnO_2 (α, β, γ, δ) [36][59][60][61][62][63] and their derivatives [54][64][65][66][67][68] have been shown to be compatible with AZB. Its low-cost, abundancy and low toxicity features also align with the expectation for AZBs to be used for large-scale energy storage; 2. V_2O_5 [50][69][70][71] and its derivatives[72][73][74][75][76][77][78][79][80][81][82] are also another well studied cathode system for AZBs, appraised for their low cost and abundancy; 3. Prussian blue analogues [83][84][85][86][87][88][89][90] and polyanionic olivine-based phosphates[56][91][92][93][94] have also been demonstrated to allow reversible Zn ion insertion and have proposed as AZB cathodes. [95]

However, unlike LIB, whose cathode mostly function via a simple ion-intercalation process during charging and discharging, the proposed cathode materials for AZBs operate via various mechanisms,

including Zn ion insertion/extraction, chemical conversion reaction (α-MnO_2), H^+, Zn^{2+} co-insertion/extraction etc. [36][59][60][63][77] And many of these mechanisms are accompanied by phase changes during charge and discharge. This is partly because Zn ions are larger and yet have higher charge density, which makes their movements more kinetically challenging [95]. And therefore cathode materials usually have to undergo structural change to accommodate these large-sized ions as they move in and out. Such significant structural or phase change have led to problems like low reversibility and cathode dissolution, causing rapid cathode capacity decay [77]. So many AZB researchers these days have been focusing on exploring new materials or strategies to minimize cathode structural change during cycling while maintaining a good cathode energy density.

1.2.3 Anode for aqueous zinc battery

Compared with the cathode, AZB's anode research has attracted less attention until recently. This is mainly because there has been little incentive to find new anode materials to replace metallic Zn anode, which has been widely considered to be the golden standard for AZB anode due to its highest capacity, low cost, high abundancy, high safety and stability in water. It is also highly electrically conductive and suffers little polarization during cycling. Metallic Zn anode also acts as the Zn ion source in the full AZB cell as, unlike in LIBs, almost all AZB cathode materials do not inherently possess Zn ions. [48][49][96][97][97] [98][99][100] Therefore, it is almost impossible to finds an alternative anode material which can outperform metallic Zn in all these metrics for AZB.

Yet, so far, there has been relatively little work performed to systematically assess metallic Zn anode's performance and its relevant degradation processes during cell cycling or aging. This overlook is largely because most AZB research works, including those focusing on cathode, electrolyte or even anode, have been employing metallic Zn anodes with excess capacity for their cycling tests [101][102]. As a result,

any potential capacity loss on the anode side is not signaled in the electrochemistry performance. This has given the false impression that the existing metallic Zn anode is already stable enough for commercialization. However, recent works on zinc anode have shown that metallic Zn's water stability is only relative but not absolute. In fact, it does suffer from various degradation processes over prolonged cycling or aging in aqueous solutions[48][49][96][103][104][105] [106].

1.3 Anode degradation in neutral/mildly acidic AZBs

Compared with the alkaline electrolytes, in which metallic Zn anode undergoes a more complex reaction mechanism during cycling (Zn -> $Zn(OH)_4^{2-}$ -> ZnO during discharging and ZnO -> $Zn(OH)_4^{2-}$ -> Zn during charging), metallic Zn's mechanism in neutral/mildly acid electrolytes is much simpler (Zn -> Zn^{2+} during discharging and Zn^{2+} -> Zn during charging, similar to that in LIBs [40][99][100]). And the common issues suffered by alkaline AZB electrolytes like surface passivation (due to hydroxide and oxide formation) and anode shape change can be largely mitigated by switching to neutral/mildly acidic electrolytes for AZBs.

However, despite these improvements, AZBs based on neutral/mildly acidic electrolytes can still suffer from anode degradation, which mainly includes three types: Corrosion, H_2 evolution and Zn dendrite formation. [100][107][107][47][103]

1.3.1 Corrosion

Several works have demonstrated that corrosion does take place in neutral/mildly acidic AZB systems, evidenced by the accumulation of corrosion products during prolonged cycling or aging [48][96][104][106][108]. For example, in the most popular $ZnSO_4$ electrolyte system, multiple works have reported Zn anode decolorization or have identified via XRD the corrosion products of $Zn_4SO_4(OH)_6{\cdot}xH_2O$ and $Zn(OH)_2$ on the post-aging/cycling anode. And the corresponding corrosion process has been proposed as follow[48][96][104][106][108]:

$$Zn + 2H_2O \rightarrow Zn(OH)_2 + H_2 \quad \text{(Equation 1.3.1.1)}$$

$$3Zn(OH)_2 + ZnSO_4 \cdot xH_2O \rightarrow Zn_4SO_4(OH)_6 \cdot xH_2O \quad \text{(Equation 1.3.1.2)}$$

It is generally believed that despite not completely passivating the electrode the surface, these corrosion products are non-conformal, and their formation is usually non-uniform. This layer is then

problematic for AZB anode's long-term cycling stability as its gradual thickening can lead to high resistance and disrupt the homogeneity of electric field across the anode which accelerates the non-uniform distribution of Zn deposition and dendrite formation. And this corrosion process also gradually consumes water and $ZnSO_4$, leading to problems like electrolyte depletion, pH change and electrolyte concentration change and even salt precipitation, all of which can potentially alter the reaction environment and subsequently lead to accelerated anode capacity loss and premature cell failure.

1.3.2 Hydrogen evolution

H_2 evolution is a commonly reported issue in AZBs' studies, mostly manifested by post-cycling AZBs showing significant cell bulging and in-situ AZB mass spectroscopy showing H_2 evolution over cycling.[103][109][110][111][112] The H_2 evolution in AZBs can be either due to the corrosion process (equation 1.3.1.1), a by-product as metallic Zn gets oxidized to form hydroxide, or it can be due to a simple water reduction process:

$$2H^+ + 2e^- \rightarrow H_2 \text{ (Equation 1.3.2.1)}$$

This water reduction can take place simultaneously as the Zn reduction during AZB charging. Water's Pourbaix diagram shows that the H_2 evolution potential is calculated as E_{H2} = 0.059 x pH [49], meaning that in most neutral/mildly acidic electrolytes, the water reduction potential is similar or even higher than that of Zn/Zn^{2+}. And despite that Zn anode possess a high H_2 evolution over-potential, in some cases, for example, when the local pH became very low or if the cell was charged under high-rate conditions, under which extra high potential is applied, such H_2 evolution can still occur.

H_2 evolution is quite problematic for AZBs. Like corrosion, it also gradually consumes water and alters electrolyte concentration and pH, leading to problems like electrolyte depletion, salt precipitation and

subsequently cell failures [49][109][110][111]. H_2 evolution also causes substantial internal pressure build-up in sealed AZB cells which can lead to swelling, leaking or even exploding.

1.3.3 Zinc dendrite formation

Compared with the needle-shaped dendrite morphology of Zn formed in the alkaline electrolytes, Zn electroplated in neutral/mildly acidic electrolytes are mostly in the form of hexagonal platelets, which made many researchers believe that dendrite formation is not a problem in these systems. However, recent studies have shown that, dendrites can still form in neutral/mildly acidic electrolytes, leading to short-circuiting and cell failure over cycling [113][114][11][47].

Such dendrites are formed via a daisy-chain process. Despite being electroplated in the platelet morphology, the Zn platelets can gradually pile up and form small protrusion on the anode surface. Upon further plating, more Zn^{2+} ions will be attracted towards these surface protrusions' tips, i.e. 'hot spots' on which the electric field concentrates, leading to continuous localized Zn deposition and thus dendrite lengthening over time [49]. And this dendrite formation process is particularly accelerated when AZBs are cycled at high current densities and capacities. [47], [114]

Dendrite formation can lead to three big problems [49][109][115][116][117][118]: Firstly, the resultant surface roughening can largely increase the anode surface area, which leads to increased parasitic reactions like corrosion; Secondly, dendrites can become detached from the anode over cycling and form 'dead Zn', which leads to poor cell reversibility and anode capacity loss; Thirdly, once grown long enough, dendrites can pierce through the separator and short-circuit the battery, causing rapid and irreversible cell failure.

1.3.4 Strategies for mitigating Anode degradation and their limitations

Throughout the course to optimize AZB performance, various strategies have been devised to tackle one or more of its degradation problems, which can be categorized into three main types: Electrolyte modification, protective interface layer and anode engineering.

1. Electrolyte modification is commonly employed in LIBs for performance optimization and it is also the most commonly reported strategy to optimize AZB's anode, which can be further categorized into four sub-types: concentration modification, pH modification, electrolyte additive, and solidified/jellified electrolyte:

a. **Concentration modification**: It is well known that high-concentration electrolytes can lead to reduced side reactions and better anode reversibility in LMB [119][120][121]. Similarly, the same concept has been shown to also work in AZBs, as demonstrated in the ZnTFSI + LiTFSI system and the $ZnCl_2$ system[105][122]. High salt concentration leads to reduced H_2 evolution by reducing the amount of free H_2O molecules within the electrolyte (Equation 1.3.2.1). It can also reduce anode corrosion by altering the solvation sheath structure of Zn^{2+} ions [123] to have minimal interaction with the H_2O molecules (Equation 1.3.1.1). However, despite showing improved cycling performance, using high concentration electrolyte substantially increases the cost of and lowers the ionic conductivity of the cell. In addition, this strategy is only compatible with those AZB electrolytes using salts with high aqueous solubility (TFSI & Cl systems) and is not universally applicable to most AZB systems like $ZnSO_4$.

b. **pH modification**: changing pH can lead to substantially different plating behaviors and should be treated carefully. A high pH can effectively reduce the chance of H_2 evolution from water reduction (according to water's Pourbaix diagram [49][103]). However, when it is too high, dendrites and a passivation layer of oxide and hydroxide are more likely to form, as shown in the alkaline AZBs. On the other hand, a low pH has also been reported to promote more homogenous Zn plating in the $ZnSO_4$

electrolyte system. However, its underlying mechanism remained unexplained and a low pH level can lead to accelerated corrosion and H_2 evolution and makes the electrolyte less compatible with common battery components like metallic casing etc.

c. **Electrolyte additive**: having additives is the most commonly used attempt to solve various problems in AZBs like corrosion and dendrite formation. And both organic and inorganic additives had shown efficacy[124][125][77][126][127][128]. It has been reported that certain organic additives can effectively reduce the Zn corrosion rate by 6-30 times [126]. Additives can also mitigate dendrite formation mainly via two mechanisms: firstly, some additives can help regulate the electric field on the anode surface for more ordered & uniform plating. In some cases, for example when using highly polarized organic molecules, the additives can further electrically shield any protrusion tips, preventing them from becoming the 'hot spots' with concentrated electric field for potential dendrite nucleation [125][127]. Secondly, some additives can help change metallic Zn's surface energy [128] within the electrolyte and thus modify their plating morphology from hexagonal platelets to more globular shapes, which are less likely to form dendrites. However, additives usually lead to higher electrolyte cost. And their potential electrochemical break-down can lead to additional side reactions and by-products, which can be problematic for cells' long-term performance. In some cases, especially when excess organic additives are used, cells' rate performance will also be compromised due to poor ion diffusion kinetics and high polarization.

d. **Solidified/Jellified electrolyte**: various approaches have been attempted to solidify or jellify the AZB electrolytes[129][130][131][132][133][134]. These electrolytes are claimed to suffer from less corrosion due to reduced mobility of the salt and water molecules [129]. Their increased mechanical integrity can also potentially suppress dendrite formation to some extent [129]. On top of that, compared with liquid, solidified/jellified electrolytes are less prone to cell leakage even under stress, and yet they are flexible

enough, which makes them safer to handle and compatible with wearable devices[130][132][133][134]. However, once solidified/jellified, their Zn ion conductivity is reduced. And ensuring these electrolytes' conformality to the electrodes is maintained can be challenging, and poor contact can easily lead to localized current and dendrite nucleation. As the result, most of these solidified/jellified electrolytes cannot sustain long cycling at high rates.

2. Protective layer, i.e. artificial SEI, is also a popular strategy for mitigating anode problems [135][136][137] [138][139][140][141]. Such a layer helps minimize the direct contact between the anode and the aqueous electrolyte and therefore reduce the rate of corrosion and hydrogen evolution [135][140] [141]. Reports have also shown that it can help achieve a more uniform Zn plating via maintaining a uniform electric field during cycling which helps avoids the formation of local 'hot spots' from which dendrites are like to grow [135][137][138][139][141]. However, these layers not only add production cost to the cell, Zn^{2+} ions migration through these layers are also much slower which can lead to compromised cell kinetics which limits its rate performance. And unlike LIBs, in which SEI are formed electrochemically/chemically from the electrolyte-anode reaction and thus are self-reinstated once broken, most reported AZB protective layers are applied externally before cell assembly. And therefore, there is no guarantee that such a layer can be well maintained over prolong cycling, and localized breaking of the layer could potentially lead to 'hot spots' and thus dendrite formation.

3. Anode engineering, in comparison, is the least explored technique for AZB anode, which only became popular in recent years. This includes two types: anode shape engineering and surface texture engineering.

a. **shape engineering**: is the more conventional approach which has been previously reported in other battery systems. This is usually done by replacing the conventional flat Zn metal foil with 3D porous structures, including carbon-based (nanotubes, fibre, cloth), copper-based (foam), and MOF-based materials [142], [143][144][145][146]. It substantially increases the total surface area of the anode and therefore reduces the effective current density felt by the anode. For example, if replacing a 1 cm^2 Zn foil with a 3D structure of 100 cm^2 total surface area, when the same nominal current density of 10 mA cm^{-2} was applied for cycling, the effectively current density experience by the 3D anode is only 0.1 mA cm^{-2}. This helps mitigate the dendrite formation since dendrites are more likely to form at higher rates, and 3D structures can largely remove the risk of forming localized high-rate 'hot spots'. However, 3D structures are not only expansive and challenging to scale up, but they also largely increased the anode's volume uptake and effectively reduce the cell's energy density. Their large surface area also means that more electrolyte is needed for the cell and the increased electrolyte-anode interface can also lead to accelerated anode corrosion and hydrogen evolution.

b. **Surface texture engineering**: This is a strategy which remained little explored until recently. This strategy is more effective in zinc batteries than in other battery systems due to Zn metal's HCP crystal structure with highly anisotropic lattice parameters and surface energies along different crystal planes: (002) is the lowest surface energy face at 0.02 eV Å-2, nearly three times lower than that of the (111) and (101) faces. And therefore metallic Zn usually deposits as (002)-oriented platelets. [147]

The idea is then to modify the anode surface texture to favor Zn deposition along its (002) direction while keeping the (002) deposition parallel to the anode surface, so that a flat and planar anode can be maintained over cycling. As previously mentioned, Zn dendrites form via a daisy-chain process from the gradual pile-up of randomly orientated Zn platelets during cycling. And a texture anode surface promoting ordered planar Zn plating can largely reduce the randomly orientated Zn platelet formation

and thus reduce the chance of dendrite formation. Several approaches have been attempted to achieve this controlled Zn deposition: firstly, substrate materials with similar lattice parameter to that of (002) Zn plane, including Sn and graphene have been shown to promote (002) Zn deposition; Secondly, severe rolling of Zn foils can mechanically induce their (002) texturing, which can then be used as the anodes in AZBs to promoting more (002) Zn deposition upon cycling; Thirdly, by manipulating the electrolyte chemistry, the surface energies of zinc can be manipulated to further promote (002) Zn deposition even on incoherent anode substrates. [148]–[151][126] These attempts all have all shown improved anode performance. However, none of them could achieve near-perfect (002) Zn deposition: significant amount of non-(002) deposition, like (100) and (101), can still be observed on their post-plating anode surface. And these non-planar peaks also become more significant after prolonged cycling. This indicates that their effectiveness to promote (002) deposition is still yet to be improved. [148]–[151]

1.4 Calcium Battery Systems

Calcium-ion based battery systems have been deemed by many as a promising future LIB alternative. This is not only because of calcium's high abundancy, low cost and non-toxicity, but also its low redox potential (Ca/Ca^{2+} potential at -2.87V V.S. S.H.E.) and its ions' relatively small charge density compared with other multivalent ion systems, which make calcium batteries more suitable for high-power-density and high-rate applications [152][153][154][20]. However, calcium batteries' development has been long stagnated and only started to regain researchers' attention in recent years.

1.4.1 Calcium Battery's Brief History

The earliest attempt to utilize calcium for energy storage can be dated back to 1964, when Ca anode was coupled with Ag anode in a thermal battery system [155], after which a few more Ca-based energy storage systems were devised [156][157][158][159][160]. But all these pioneer systems were largely limited by their high operation temperature of several hundred degrees, which prohibited their wide applications.

The first room-temperature calcium battery was devised in 1980, a primary cell with Ca anode coupled with a carbon cathode and $Ca(AlCl_4)_2$-$SOCl_2$ electrolyte.[161] This work did draw some attention at the time, based on which a few more systematic studies [162][163][164][165] and electrolyte optimization works were published [166][167][168]. However, this system suffered from severe corrosion and showed no reversibility due to passivation layer formation [161][162][165][168].

While rechargeable LIBs became commercialized in the 1990s, a systematic assessment on the calcium battery system was performed by Aurbach et al [169]. By testing various permutations of common solvents (acetonitrile, tetrahydrofuran, γ-butyrolactone, propylene carbonate) and calcium salts ($Ca(Cl0_4)_2$, $Ca(BF_4)_2$, $LiAsF_6$, tetrabutyl ammonium salts (ClO_4^-, BF_4^-)), he concluded that rapid anode

passivation is a universal problem in these systems. The passivation layer (composed of $CaCl_2$, CaO, $Ca(OH)_2$, $CaCO_3$) [169][170] completely blocks these cells' plating process, prohibiting their rechargeability. And this bottleneck remained untackled for 25 years, until 2015.

1.4.2 Achieving Reversible Metallic Ca Anode

In 2015, Palacín et al. reported, for the first time, that reversible Ca plating can be achieved with $Ca(ClO_4)_2$ and $Ca(BF_4)_2$-based electrolytes at moderately elevated temperature of 75-100℃ [32]. They showed that an optimal reversibility of over 80% could be achieved in 0.45M $Ca(BF_4)_2$ in EC:PC at 100℃ using cyclic voltammetry. While an SEI composed mainly of CaF_2 was formed, the plating exhibited good stability after 30 cycles and a wide redox window of over 4V. However, the above-75℃ operating temperature and the 80% reversibility still lack practicality for large-scale adoption.

The first room-temperature, highly reversible Ca plating was realized in 2017 by Bruce et al. [33], who demonstrated that more than 50 galvanostatic cycles (1mAh cm^{-2} capacity; 1mA cm^{-2} rate) could be achieved in a 1.5 M $Ca(BH_4)_2$ in THF electrolyte, with high reversibility of over 95% and low polarization of 100 mV. And despite having formed a surface layer, the CaH_2 layer formed in this system did not seem to terminate the Ca plating and stripping process.

While having an outstanding room-temperature performance, the borohydride system is intrinsically limited by its reducing power which leads to a narrow redox stability window of only 3V. In 2019, a new electrolyte system based on fluorinated alkoxy borate salts was proposed independently by Zhao-Karger [41] and by Nazar [42]. Although it has slightly higher cycling overpotential and lower reversibility, this system benefits from a much wider redox window (up to 4.9V in some case [42]) and is compatible with most commonly used current collectors like SS (Stainless Steel), Cu and Al, unlike the borohydride system which are more dependent on using precious metal current collectors [33].

These studies sparked a new research wave on calcium batteries: more systematic studies, and optimization works were performed on these systems:

It was found that the calcium's plating morphology is highly dependent on substrate [171] and current density [172]. It has been shown that using additives (Li salt or organic ligands) can effectively change the solvation structure of the Ca ions within the electrolyte, effectively improve metallic anode's reversibility and prolong its cycle-life. [173] [31] It has been shown that SEI engineering is also a good strategy to stabilize Ca plating for prolonged cycling conditions. By introducing an artificial SEI with good stability and Ca ionic conductivity, reversible Ca plating can be achieved with previously inactive electrolytes and current collectors [174][175] and under high-rate and long-cycle conditions. [176][177]

1.4.3 Alternative anode options for calcium batteries

Just like in other battery systems e.g., LIBs, when it is difficult to achieve satisfactory performance with only a metallic anode, the compromised solution is to turn to alternative anode systems with better stability. And the two most popular approaches are alloying and intercalation.

Compared with intercalating anodes, alloying anodes usually offer higher specific capacity yet bigger volume change, i.e. structural instability, during cycling [178]. DFT simulations have indicated many promising alloy anode candidates for calcium batteries [179]. However, very few works have experimentally verified their performance, which currently only limited to Si and Sn. The Si study was performed in 0.45M $Ca(BF_4)_2$ in EC:PC at 100℃, which showed reversible calciation but suffered from large voltage hysteresis [180]. The Sn studies were performed in a multi-ion cell set-up with a $Ca(PF_6)_2$ in carbonate electrolyte, which showed excellent cycling performance (in some case 84% retention over 1000 cycles) and wide redox window (4.45V), but suffered from low coulombiccoulombic efficiency, especially at low cycling rates.[181][182][183] A few intercalation materials based on graphite and its

derivatives have been demonstrated by simulations to serve as potential anodes for calcium batteries with high theoretical capacity [27][184][185][186]. Its feasibility was verified experimentally by Park et al. who demonstrated highly reversible calcination with good capacity retention after 200 cycles.[187] However, this system exhibited relatively low specific capacity and requires the use of a co-intercalating DMAc solvent. Other than alloying and intercalation, a few simulations works have also proposed other anode systems for calcium batteries which include conversion reaction compound [188] and MXenes [189][190].

In general, Ca ions' large ion radius, along with its bivalency and high charge density, makes it rather challenging to be reversibly fitted into most anode materials commonly used in other battery systems. And due to the inconsistency in test conditions and the lack of experimental data to verify simulation results, at this stage, it is difficult to say whether alternative anode systems can offer more advantages over the metallic anode system for future commercialization.

1.4.4 Cathode options for calcium batteries

Due to the historical lack of available anode and electrolyte system with good reversibility, the cathode material exploration for calcium batteries has been largely limited to computational studies with very few experimental-based works published until recently. [152][153][191][192][193] Following the success of room-temperature reversible metallic anode, with the hope for calcium battery's commercialization reignited, more works on calcium battery cathode were published in the past 5 years. Many of these works are based on the existing research on sodium/potassium ion batteries and other multivalent systems whose ion size are comparable to that of Ca^{2+}. The most popular systems include layered oxide, phosphate and Prussian Blue Analogues, as summarized in Table 1.4.4.1 (here we only included studies

with typical calcium battery systems with organic electrolytes, and exclude the atypical ones like, Ca-S, $Ca-O_2$, dual-ion/aqueous/solid state systems etc.) :

Cathode	Counter	Electrolyte	Reversibility	Test Range		Capacity	Cycle rate	Cycle
Layered Metal Oxide								
V_2O_5[194]	Ca	1 M $Ca(ClO_4)$ in ACN	No	-1.5	0.5	N/A	50 μA cm^{-2}	N/A
V_2O_5-P_2O_5[194]	Ca	1 M $Ca(ClO_4)$ in ACN	No	-1.5	0.5	N/A	50 μA cm^{-2}	N/A
V_2O_5[195]	Ca	1 M $Ca(ClO_4)$ in ACN	No	-2	0.5	N/A	50 μA cm^{-2}	N/A
V_2O_5+PC [196]	carbon	$Ca(ClO_4)_2$ in PC	unknown	-1	1	~200	~50 mA g^{-1}	35
$CaCo_2O_4$[197]	V_2O_5	0.5 M $Ca(ClO_4)_2$ in CAN	<40%	-1.1	2.3	90	100 μA cm^{-2}	30
$Ca_3Co_2O_6$[198]	Ca	0.45 M $Ca(BF_4)_2$ in EC:PC @100 °C	No	1	3.5	N/A	C/200	N/A
Ca_xMoO_3[199]	charcoal	0.1 M $Ca(TFSI)_2$ in ACN	<85%	0.9	2.9	90	2 mA g^{-1}	12
$NH_4V_4O_{10}$[200]	Mn-bdcNH_2	1 M $Ca(ClO_4)_2 \times H_2O$ in ACN	<80%	0.01	2	75	100 mA g^{-1}	100
$Mg_{0.25}V_2O_5 \cdot H_2O$[201]	carbon	0.8 M $Ca(TFSI)_2$ in EC:DMC:PC:EMC	98.4%	-2	1.3	70	20 mA g^{-1}	500
$Ca_{0.13}MoO_3 \cdot (H_2O)_{0.41}$[202]	carbon	0.5 M $Ca(ClO_4)_2$ in CAN	~100%	-1.2	0.8	91	343 mA g^{-1}	50
$Mg_{0.15}MnO_2$[31]	Ca	0.5M $Ca[B(hfip)_4]_2$ in DME-M4B	~100%	2.1	3.6	210	100 mA g^{-1}	50
Polyanionic Phosphates								
desodiated Na_2FePO_4F[203]	carbon	0.2 M $Ca(PF_6)_2$ in EC:PC	>85%	-1.5	3	80	10 mA g^{-1}	50
$NaV_2(PO_4)_3$[204]	carbon	0.5 M $Ca(BF_4)_2$ in EC:PC after activated @ 75 °C	~100%	-0.1	0.6	70	5.85 mA g^{-1}	30
$NaV_2(PO_4)_3$[205]	carbon	1 M $Ca(TFSI)_2$ in ACN	~100%	-0.4	0.4	81	3.5 mA g^{-1}	40
$FePO_4$[205]	carbon	1 M $Ca(TFSI)_2$ in ACN	~70%	-0.4	0.4	72	7.5 mA g^{-1}	25
$Na_{0.5}VPO_{4.8}F_{0.7}$[206]	carbon	1 M $Ca(PF6)_2$ in EC/PC	>95%	-1	1.5	75	50 mA g^{-1}	500
Metal Sulfide								
TiS_2[207]	Ca	0.45 M $Ca(BF_4)_2$ in EC:PC @100 °C	>95%	1	3.4	500	C/100	1
TiS_2[207]	Li	0.1 M $Ca(CF_3SO_3)2$ in PC + DMC	>90%	1.5	3	90	50 mA g^{-1}	3
CuS[208]	carbon	0.8 M $Ca(TFSI)_2$ in EC:DMC:PC:EMC	<85%	0.4	3.1	100	100 mA g^{-1}	30
Prussian Blue Analogues								
$Na_{0.2}MnFe(CN)_6$[181]	calciated Sn	0.2 M $Ca(PF)_6$ in EC:PC	90-95%	0	4	80	10 mA g^{-1}	35
$NiFe(CN)_6$[209]	carbon	0.2 M $Ca(PF_6)_2$ in 3:7 EC:PC	>85%	-1	3	50	10 mA g^{-1}	50
$CaCoFe(CN)_6$[210]	carbon	1M$Ca(ClO_4)_2$ 3.5H_2O in ACN	99.2%	0	0.8	44.2	100 mA g^{-1}	100
$KxNiFe(CN)_6$[211]	carbon	0.5 M $Ca(TFSI)_2$ in ACN	92.0%	-1	1	50	25 μA cm^{-2}	12
$KFe^{3+}(Fe^{2+}(CN)_6)$[212]	Graphite	1 M $Ca(ClO_4)_2 \times H_2O$ in CAN	unknown	-0.07	1.37	120	125 mA g^{-1}	80
$KFe^{3+}(Fe^{2+}(CN)_6)$[213]	Ni(OH)[C_6H_4 (COOH)(COO)]	1 M $Ca(ClO_4)_2$ in ACN	95.4%	0	2	82	100 mA g^{-1}	100

$KFe^{3+}(Fe^{2+}(CN)_6)$[213]	$Ni[C_6H_4(NH_2)(COO)_2]$	1 M $Ca(ClO4)_2$ in ACN	97.0%	0	2	86	100 mA g^{-1}	100
Others								
Mo_6Se_8[214]	$CaHg_{11}$–Ca	$Ca(ClO_4)_2$ in ACN	70-80%	0.4	2.1	<10	<1 mA g^{-1}	50
PAQxS[215]	CNT	0.3M $Ca[B(hfip)_4]_2$ in DME	80.0%	1.3	3.3	100	122 mA g^{-1}	10
PTCDA[216]	carbon	saturated $Ca(ClO_4)_2$ in PC	~100%	-1.2	1	50	1000 mA g^{-1}	500

Table 1.4.4.1*: A summary of all the cathode materials reported for the conventional calcium-ion battery system including layered oxides, phosphates, Metal Sulfide and Prussian Blue Analogues.*

From table 1.4.4.1, we can see that the development of cathode materials for calcium batteries are still at their early stage. Most of the candidates suffered from problems like low capacity, low reversibility and limited rate performance and post-cycling capacity retention. This is partly because these systems are currently still at their early stage and lack optimization. And these studies used different test conditions (cell loading, electrolyte, anode, voltage window, rates, cycle number etc.), which makes it even harder to do fair quantitative comparison. Therefore, it is also quite necessary to do future studies in more standard and consistent conditions, can we then make fair comparison among different materials to draw some useful conclusions.

1.4.5 Other calcium-ion-based battery systems

Apart from the conventional battery set-ups, other systems have also been proposed including Ca-S [217][218][219][220][221] and Ca-O_2[222][223], liquid metal batteries[224][225][226], solid-state calcium batteries [227][228][229], aqueous calcium batteries [230][231][232][233][234][235][228], and dual-ion calcium batteries[236][183][182].

Ca-S and Ca-O_2 have been developed based on the concepts of Li-S and Li-O_2, which also suffer from similar problems to their Li counterparts: Ca-S suffer from Ca anode passivation and low S utilization

rates; Ca-O_2 suffer from Ca anode passivation and cathode CaO's irreversibility due to its high stability. Liquid metal batteries based on Ca metals are mainly limited by their high operating temperatures due to Ca's high melting temperature. Solid state calcium batteries so far had little experimental success mainly due to Ca ion's large size limiting its solid-state diffusion at room-temperature.

Aqueous Ca systems and dual-ion calcium batteries so far seem to stand out from these alternative systems. Aqueous Ca systems usually use $CaNO_3$ electrolyte and can achieve good reversibility and capacity retention, however their energy densities are relatively low due to low capacity and narrow potential window. Dual-ion calcium batteries represent a special system, in which both Ca cations and PF_6 anions take part in the intercalation/deintercalation process during charging and discharging. Compared with other systems, they not only demonstrated outstanding reversibility and post-cycling capacity retention, but also have high specific capacity and wide potential window[236][183][182].. However, this system is limited by the total amount of ions within the electrolyte, whose depletion is likely going to lead to rapid cell failure and its performance in lean-electrolyte conditions has yet to be tested.

2 Experimental

2.1 Common Characterization Techniques for Batteries

2.1.1 Electrochemical Tests (Galvanostatic Cycling and Cyclic Voltammetry)

Galvanostatic cycling is the golden standard for battery testing [237], which can give a good indication of a battery's reversibility, capacity retention, possible side reactions etc. A cell under galvanostatic cycling is subjected to multiple cycles of charging and discharging by applying a constant current density while the cell's potential is being measured.

A battery cell's potential is primarily determined by the nature of the electrochemical reactions taking place at the cathode and the anode, for a typical electrochemical reaction:

$$aA + bB \leftrightarrow cC + dD \quad \text{(Equation 2.1.1.1)}$$

Where A, B, C, D are different chemical species and a, b, c, d are their corresponding stoichiometric coefficients. Its potential ΔE is related to its Gibb's Free Energy ΔG:

$$\Delta G = -nF\Delta E \text{ (Equation 2.1.1.2)}$$

Where n is the charge transfer number and F is the Faraday's constant. At standard conditions this becomes:

$$\Delta G^o = -nF\Delta E^o \text{ (Equation 2.1.1.3)}$$

ΔG^o is related to ΔG:

$$\Delta G = \Delta G^o + RTlnQ \text{ (Equation 2.1.1.4)}$$

Where R is the gas constant, T is the temperature and Q is the reaction quotient, defined as:

$$Q = \frac{[C]^c[D]^d}{[A]^a[B]^b} \text{ (Equation 2.1.1.5)}$$

Combining Equation from 2.1.1.2 to 2.1.1.5, we can obtain the famous Nernst Equation:

$$\Delta E = \Delta E^o - \frac{RT}{nF} ln \frac{[C]^c[D]^d}{[A]^a[B]^b} \text{ (Equation 2.1.1.6)}$$

At equilibrium, where $\Delta E = 0 \; and \; Q = K$ (equilibrium constant), Equation 2.1.1.6 becomes:

$$\Delta E^o = \frac{RT}{nF} lnK \text{ (Equation 2.1.1.7)}$$

Applying Nernst Equation to a typical battery cell with $LiCoO_2$ cathode and graphite anode with the following reactions:

$$\text{Cathode: } CoO_2 + Li^+ + e^- \leftrightarrow LiCoO_2 \text{ (Equation 2.1.1.8)}$$

$$\text{Anode: } LiC_6 \leftrightarrow C_6 + Li^+ + e^- \text{ (Equation 2.1.1.9)}$$

$$\text{Overall: } LiC_6 + CoO_2 \leftrightarrow C_6 + LiCoO_2 \text{ (Equation 2.1.1.10)}$$

We can obtain the cathode and anode potentials:

$$\text{Cathode: } E_c = \Delta E^o{}_c + \frac{RT}{F} ln \frac{[Li^+]_l[CoO_2]_s}{[LiCoO_2]_s} \text{ (Equation 2.1.1.11)}$$

$$\text{Anode: } E_a = \Delta E^o{}_a + \frac{RT}{F} ln \frac{[Li^+]_l[C_6]_s}{[LiC_6]_s} \text{ (Equation 2.1.1.12)}$$

Where 's' and 'l' subscript indicate the species' concentration in solid phase (electrode) or in liquid phase (electrolyte). From Equation 2.1.1.11 and 2.1.1.12, we can obtain the overall voltage of the battery cell:

$$\text{Overall: } \Delta E = E^o{}_c - E^o{}_a + \frac{RT}{F} ln \frac{[LiC_6]_s[CoO_2]_s}{[C_6]_s[LiCoO_2]_s} \text{ (Equation 2.1.1.13)}$$

From equation 2.1.1.13, we can see that the potential of a battery cell is related to many factors, including the nature of electrochemical reactions at the anode and at the cathode ($E^o{}_c$ and $E^o{}_a$), temperature (T), depth of charge (chemical species concentrations at the cathode and anode).

However, this thermodynamic potential only indicates the potential at equilibrium when the cell is not operating. During the cell operation or testing, i.e. when there is a current, the overall measured cell potential V_{bat}, also contains an overpotential η:

$$V_{bat} = \eta + \Delta E \text{ (Equation 2.1.1.14)}$$

Such overpotential is due to various processes and therefore includes many components like ohmic overpotential η_{ohmic} (determined by electrolyte ionic conductivity, electronic conductivity of active materials etc.), the contact resistance $\eta_{contact}$ (determined by the resistance between electrodes and current collector), charge transfer overpotential η_{ct} (determined by the activation energy to newly form lithiated or delithiated phase), diffusion overpotential η_{diff} (determined by Li ion diffusion at the electrode-electrolyte interphase and the solid-state ion diffusion within the active materials)[238][239][240]a:

$$\eta = \eta_{ohmic} + \eta_{contact} + \eta_{ct} + \eta_{diff} \text{ (Equation 2.1.1.15)}$$

This can be perceived as the additional driving force required to overcome the obstacles (resistance from various components, energy barriers etc.) and to drive the reactions (ionization, deionization, ion diffusion etc.)

However, in this thesis, I mostly focused on anode behaviors, and employed galvanostatic cycling to look at cells' reversibility, cycle life and overpotential change. The capacity difference between the charging and discharging cycles i.e. coulombic efficiency, is indicative of how reversible is the cell, from which we can compare the performance of different electrode materials and different electrolytes, the cycle life, i.e. how many cycles can a cell sustain before failure is indicative of how rapid dendrite grows (if failure by short-circuit) or how rapid electrolyte depletes or electrode is passivated/consumed (if failure by open-circuit). The overpotential change over time is usually indicative of electrode surface change or

side reactions. For example, an increasing overpotential over cycling usually means there is a higher resistance for ion/electron transport, which could be due to surface passivation, SEI growth, electrolyte depletion etc.

Cyclic voltammetry [237], on the other hand, can be used to decouple and quantify different electrochemical processes within a cell. By sweeping the potential between the electrodes at a constant rate within a certain potential range and measuring the resultant current flow, we can identify different electrochemical processes and their corresponding redox potentials. As previously shown in Equation 2.1.1.15, overpotential η during cell operation can be due to processes like ion diffusion and charge transfer. And by running cycling voltammetry at different scanning rates, we can also better understand these processes and their kinetics [241]. In this work, I mainly cyclic voltammetry to check electrochemical systems' reversibility and to check for potential side electrochemical reactions.

2.1.2 X-Ray diffraction (XRD)

XRD is a common technique to determine the crystal structure, orientation, particle size, internal stress etc. of crystalline samples. In this work it is mainly used for compound identification and sample surface texture indication.

By using X-ray of fixed wavelength λ, we can identify different crystal planes and quantify their interplanar spacing d using Bragg's Law [242]:

$$2dsin\theta = n\lambda \qquad \text{(Equation 2.1.2.1)}$$

Where d is the interplanar spacing, θ is the incident angle of the X-ray, λ is X-ray's wavelength and n is an integer. When Bragg's law's condition is met at given incident angle θ, the constructive interference of the X-ray will lead to a spike in the received X-ray diffraction signal, from which the interplanar

spacing of a particular crystal plane can be worked out, as shown in Figure 2.1.2.1. A unique series of multiple planes identified at different incident angles with different diffraction signals can then be used to help identify the corresponding compounds and indicate their surface texture.

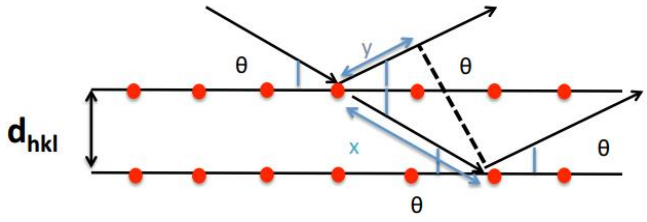


***Figure 2.1.2.1**: Bragg's Law illustration (from Imperial College London Lecture Notes)*

2.1.3 Scanning Electron Microscopy (SEM), Electron Backscatter Diffraction (EBSD) & Energy Dispersive X-ray Spectroscopy (EDS)

SEM is commonly used to image material at different magnifications, thanks to its high special resolution and large field of view [243][244]. The high spatial resolution is a result of electron's short wavelength since the highest achievable spatial resolution from any wave media is comparable to that of its wavelength. For example, in conventional optical imaging, the spatial resolution is limited to a few hundreds of nanometers as limited by visible light's wavelength. However, in SEM, the electrons can have sub-nanometer wavelength. However, it is to note that, once the wavelength is too short, the spatial resolution is limited by other factors like lens aberrations, which then is no longer comparable to the wavelength.

SEM uses an electron beam for imaging, which is generated from an electron gun. The beam was then focused into a point using a series of electromagnetic lenses and apertures, which was then used to raster across the sample surface. Once the beam hits the sample surface, it interacts with it and results

in different signals, which is then detected by the detectors and shows different information about the sample.

The most common signals include secondary electrons, back scattered electrons and characteristic X-Ray. Once an electron hits the sample surface, it can excite the atoms there. The excited atoms can either have enough energy to emit an outer-shell electron, releasing a secondary electron, or to have a lower band electron excited to a higher band, whose later relaxation then leads to the release of a characteristic X-Ray since these bands' energy level are quantized. During this reaction, the incident electrons might be deflected back away from the sample surface and detected as back-scattered electrons, despite possibly losing some energy during the deflection.

The secondary electrons usually have very low energies, so only the ones generated near the surface can be detected, therefore it is usually good for topographic imaging since it has the best spatial resolution and good surface sensitivity. The detectable depth of backscattered electrons is larger than that of secondary electrons and this depth is also atomic number dependent. Therefore, despite having lower spatial resolution, back-scattered electron imaging usually contains more compositional information. For example, it can help distinguish different phases on the surface based on their different electron scattering power. Lastly, the characteristic X-Ray is much easier to penetrate through the sample and thus its detectable depth is the largest among the three which means it has the lowest spatial resolution. However, their energies (unique for each element due to electrons' quantized energy levels) can be used to help identify and distinguish different elements within the sample. [245]

In this work we mostly used secondary electrons to look at the topography of the sample surfaces and characteristic X-Ray for element identification and mapping.

EBSD (electron backscatter diffraction)[246][247][248] is also a SEM based technique commonly used for crystalline samples. It is a diffraction technique for sample surface using backscattered electrons. A

Kikuchi diffraction pattern is generated at each spot on the scanned region using backscattered electrons, from which different phases and grains can be identify with their crystal orientation mapped out. And like in XRD, diffraction pattern can also be used to determine other crystallographic information like strain, grain size, grain boundary characteristics etc. however on a more localized scale. In this work EBSD is mainly used for characterizing surface texture of post-plating and post-cycling metallic anode surfaces.

2.1.4 X-Ray photoelectron spectroscopy (XPS)

XPS is used to measure the elemental composition and each element's chemical environment using a photoelectric effect[249][250][251]. By hitting the sample with a X-ray of known energy E, we can excite the sample material, from which the electrons are emitted. However only the electrons emitted near surface have enough kinetic energy (KE) to leave the sample to be detected. It is therefore a very surface sensitive technique. The X-ray photon energy E and emitted electron's kinetic energy (KE) is related:

$$E = KE + BE + WF \qquad \text{(Equation 2.1.4.1)}$$

Where BE is binding energy of the sample material: the difference between electron initial E and E_F. And WF is the work function of the analyzer material. The work function is defined as energy needed to remove an electron from the analyzer material surface, which can be expressed as:

$$WF = E_{vac} - E_F \qquad \text{(Equation 2.1.4.2)}$$

Where E_{vac} is the Vacuum Energy, defined as the energy level of a free-standing electron at vacuum and E_F is the Fermi Energy, which is the energy of the highest filled orbital. This is shown in Figure 2.1.4.1:

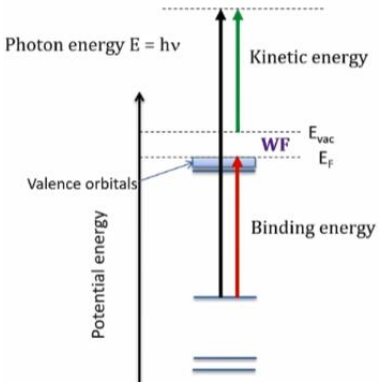


Figure 2.1.4.1*: the working principle of XPS, how KE is related to BE (from the Oxford XPS course)*

Since E and WF are constant at given test conditions, by measuring KE, we can work out BE of our sample, which is then plotted in photoemission spectrum and used to help provide information about our sample surface.

Each element has a characteristic series of atomic orbital binding corresponds to a series of core line peaks in XPS. These core lines can be used to determine the elements present on the sample surface. The peak position, i.e. chemical shift, of these core lines however gives us additional information about the chemical environment of these elements. For example, the BE of the same element in an oxide state or in a nitride state is slightly different to its BE in the metallic state. So, these peaks shifting, or splitting, can help us identify and semi quantify different chemical species on our sample surface. The resultant spectrum, however, can suffer from artifacts that arise from various processes like charging, X-ray ghost peaks, sample damage etc. The most common one is the collective peak shifting due to sample surface charging. Therefore, each obtained spectrum must be calibrated primarily with respect to the signal of adventitious carbon at 284.8 eV and double-checked using all the existing elements until all the chemical species can be sensibly assigned. In this work, XPS is mainly used to identify post-aging/post-cycling anode surface to identify SEI compositions or side reaction products.

2.1.5 Online Mass Spectroscopy (MS)

Online mass spectroscopy is a technique used to precisely quantify the amount of gas generated from a sample[252][253][254]. The sample usually sits in a sealed vial. The vial is connected to an inlet tube which allows the controlled inflow of an inert carrier gas and an outlet tube connected to the mass spectrometer which is pre-calibrated and can be used to quantify different gases evolved from the sample vial. Within the MS, different gas can be differentiated with respect to their different mass-to-charge ratio and time-to-flight within the column after being ionized and accelerated. The detector then counts the signal for each gas type for quantification. In this work, MS is mainly used to quantify the amount of residual metallic anode and some key SEI components after cycling. By titrating the post-cycling electrodes with different solution of excess amount, the resultant gas evolution is indicative of the amount of certain compound left on each electrode.

2.1.6 Atomic Force Microscopy (AFM)

AFM is a common technique to measure the surface topography and morphology of a surface[255][256][257]. By using a nanosized silicon or silicon nitride tip connected to the piezoelectric cantilever, which then raster scans in contact or tapping mode across the sample surface, the surface topography and morphology can be mapped out according to the tip's magnitude of bending to stay in contact with the sample surface. Its force curve can also give information regarding the sample surface's materials mechanical properties like hardness and elasticity etc. In this work, we mainly use its topography and morphology function to characterize post-plating anode surfaces.

2.2 Advanced Characterization Techniques for Battery Studies

2.2.1 FIB, Ion polishing machine

FIB (focused ion beam) and automated ion polishing are generally used for imaging cross-section of a sample. FIB is usually installed within the SEM. It is a localized milling technique which uses the ion beam to create a cavity from a designated region on the sample surface[258][259][260]. The cavity wall was then fine-polished with a lower-energy ion beam which can then be used for imaging, EDS mapping and EBSD. Compared with FIB, automated ion polishing is a cheaper and time-saving alternative for cross-section imaging at a larger scale. Before ion polishing, each sample was precut with a scalpel to expose a flat cross-section. However, this cross-section has a very rough surface and contains various defects generated during cutting. To remove these defects and to present a flatter cross-section before SEM imaging and EDS mapping, ion milling is usually used to fine polish the cross-section surface. Compared with FIB, an automated ion polishing machine cannot provide localized milling at designated regions and also risks damaging the existing features within the sample during scalpel cutting, however ion polishing can provide a much bigger cross-section region for SEM imaging, EDS mapping and EBSD.

2.2.2 X-Ray Computed Tomography (XCT)

XCT provides the non-destructive option to visualize the interior of the sample bulk[261][262][263][264]. A 3D tomographic image is reconstructed from many individual X-ray radiographs taken from different angles. During a radiograph scan, the whole region of interest is exposed under the X-ray beam, from which a projection image is obtained. This projection image provides the X-Ray absorption distribution information at a particular angle. The absorption amount is dependent mostly on two factors: 1. The scattering power of the different components within the sample material, 2. the thickness of these components. Therefore, simply replying on 2D radiographs is not enough to determine the component

distribution within the sample, i.e. we do not know if a localized high absorption spot is due to a regional change in composition or a regional large thickness. Therefore, to remove the thickness effect and to obtain a map which shows compositional variation and spatial distribution of these compositions within the sample, multiple radiographs are taken equiangularly from all 180º or 360º angles, which are then combined via reconstruction algorithm into a 3D tomogram. This 3D tomogram contains all the internal structure information of the scanned region which can then be resliced to provide 2D mappings of phase/composition/defect distribution with clear boundaries at any particular angle and sample depth, free from thickness effect.

2.2.3 Liquid Cell Transmission Electron Microscopy (TEM)

TEM is commonly used to characterize materials at atomic level. Figure 2.2.3.1 shows the key components of a typical TEM set-up:

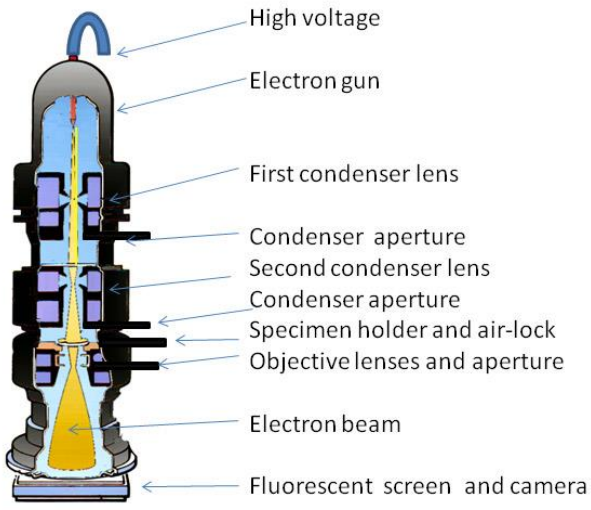


***Figure 2.2.3.1**: illustration diagram of a TEM (from drawing by Graham Colm)*

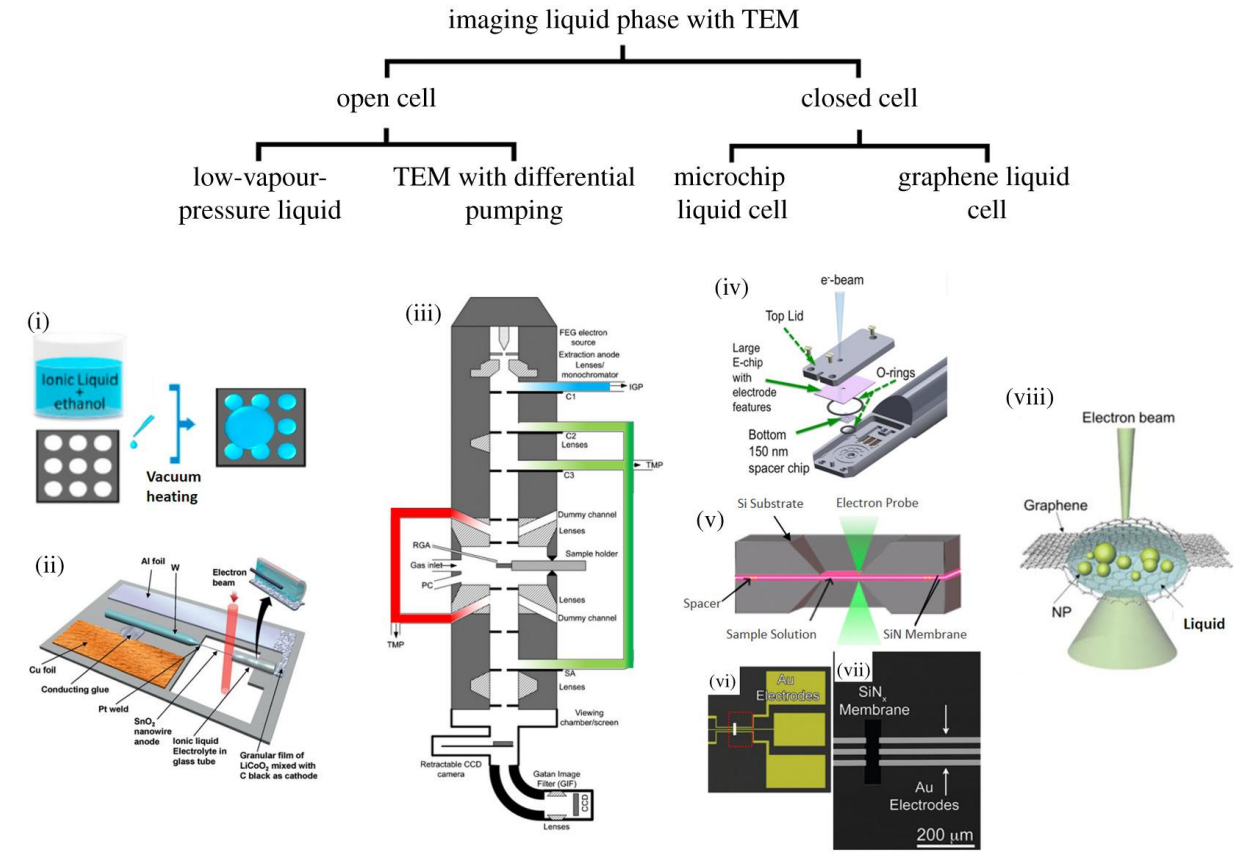
Similar to SEM, TEM also utilizes an electron beam to characterize the sample, except that SEM relies mostly on secondary or backscattered electrons generated near the surface of a thick sample while TEM

relies on the transmitted electrons across the entire thickness of a thin sample. In SEM, the resolution is defined by the beam interaction volume in which the primary electrons are scattered and deflected multiple time before generating secondary electrons, backscattered electrons, and X-rays. Backscattered electrons usually have a relatively large interaction volume, from which they will further generate more secondary electrons. And this unavoidably compromises the resolution of SEM. In TEM, however, the electron accelerating voltage is usually very high and the sample is very thin (tens of nanometers), which means that the electrons beam can easily transmit through the whole sample with minimal interaction volume. And therefore, TEM can provide a higher spatial resolution than SEM, down to atomic level. When the high-energy electron beam is transmitted, it can be elastically and inelastically scattered by the sample and the resultant beam can be collected and used for imaging. And like in XRD, the TEM electron beam will be diffracted by the crystal structure during sample interaction which provides atomic structure information like lattice defect, parameters etc.

Conventionally, TEM is only applicable to image solid materials. However, liquid phase TEM has been developed in the past three decades, which allowed the *in situ* visualization of various liquid-state specimens and processes at nanoscale, such as nanomaterial synthesis[265][266][267][268][269][270], live biological cells [271][272][273][274][275][276], battery solid–electrolyte interface (SEI) formation [277][278][279] and corrosion [280][281]. And compared with other *in situ* techniques, liquid phase TEM not only has the advantage of having high temporal and spatial resolution, it also provides direct visualization of any structural, morphological [282] or elemental distribution [283][284]changes at nanoscale. I have authored a detailed literature review on the technique in ref [xx], and below I provide a brief overview.

For TEM imaging, the microscope column needs to maintain a high vacuum, at least 10^{-5} Pa, to minimize undesired electron beam scattering and sample contamination, and the specimen needs to be thin

enough for electron beam to penetrate through. To keep the liquid thin while also unevaporated within the TEM, various techniques have been developed, including: (1) Using low-vapour-pressure liquids as an alternative [266][285][286][287][288] (2) Development of environmental TEM (ETEM) with a differential pumping system [289][285][290] (3) Encapsulating and confining the liquid into a thin layer using either Si-based chips or graphene. As shown in Figure 2.2.3.1.



advantages:
- easy sample preparation
- image with standard TEM
- high resolution
- can use a standard TEM sample holder (i)
- or electrical biasing with special TEM holder (ii)

disadvantages:
- limited liquid choice

advantages:
- easy sample preparation
- can use a standard TEM sample holder
- electrical biasing with special TEM holder
- controlled liquid flow with special TEM holder
- high resolution

disadvantages:
- special TEM required
- limited liquid choice

advantages:
- fairly easy preparation
- image with standard TEM
- wide liquid choice
- controlled liquid flow
- electrical biasing
- commercially available

disadvantages:
- compromised resolution
- special TEM holder

advantages:
- image with normal TEM
- wide liquid choice
- fair resolution
- standard TEM holder

disadvantages:
- tricky sample preparation
- no liquid flow
- no electrical biasing
- not commercialized

Figure 2.2.3.1 *Comparison of different techniques for liquid phase TEM imaging. (i) Ionic liquid films maintained inside micrometre-sized holes from surface tension, suitable for TEM imaging*[291]. *(ii) Design schematic of a miniature battery that may be imaged inside TEM, using an ionic-liquid-based electrolyte* [292]. *(iii) Schematic of differentially pumped TEM column with three different pumping stages, indicated by different coloured pipes, permitting a high pressure sample chamber* [289]. *(iv)*

Schematic of an in situ liquid TEM stage on the tip of a TEM holder [16]. *(v) Schematic of an assembled liquid cell from two silicon/silicon nitride chips* [283]. *(vi) Silicon chip with microfabricated electrodes* [278]. *(vii) Magnified SEM image of the red box region in (v), showing electrodes partially over the* SiN_x *viewing window* [278]. *(viii) Schematic of a graphene liquid cell for TEM. The specimen is encapsulated between two graphene sheets* [293].

A 'liquid cell' usually refers to the closed cell configuration based on silicon microchips as shown in Figure 2.2.3.1 iv-vii. The cell is usually in-built within the TEM specimen holder and is comprised of two silicon chips, each with a robust and electron-transparent amorphous silicon nitride (SiN) window, through which the electron beam can penetrate. The silicon chips are manufactured using lithography [294] and need to be assembled before use, as shown in Figure 2.2.3.2.

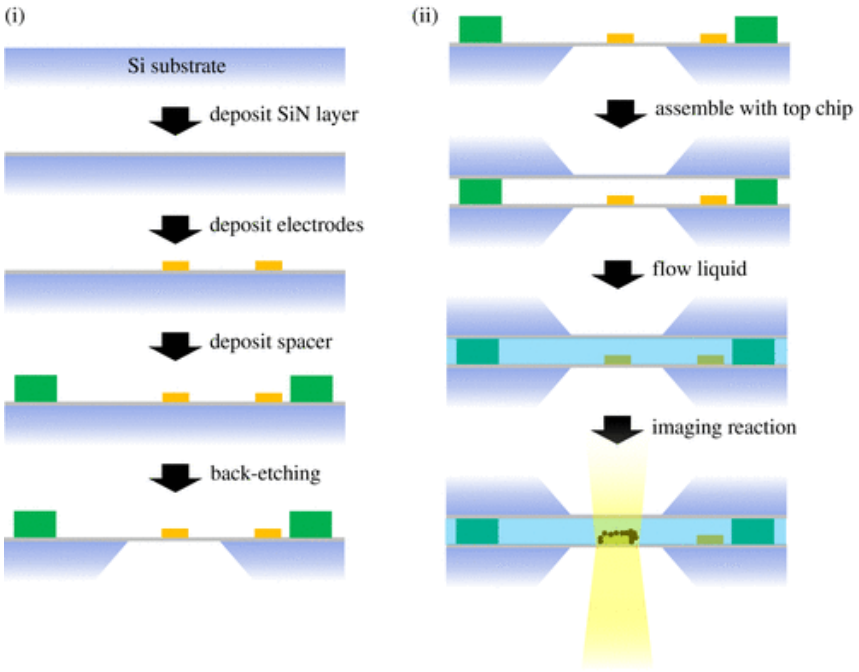


Figure 2.2.3.2 *(i) Simplified schematics of the production process of a liquid cell microchip via photolithography. (ii) Schematics of the assembly of the microchips for liquid cell TEM imaging.*

Compared with other techniques, liquid cell TEM offers a few advantages: (1) It is commercially available and is compatible with conventional TEM, which is easier to use and gives higher consistency among different experiments; (2) it can safely contain almost all types of liquid, independent of vapor pressure, which allows a wider range of systems to be studied; (3) Microfabrication allows additional capabilities including allowing liquid flow[295], temperature control [296] and electrical bias using patterned electrodes, which offers the option to conduct experiments at different conditions.

During its early stages, liquid cell TEM is mostly used for visualizing nanomaterials [265][268][270][297][298][299][300][301][302][303][304][305][306][307] and biological samples [272] [275] [294] [308][309] [310] [311]. Thanks to the advancement of chip microfabrication and cell optimization within the past 10 years, commercial liquid cells are now available with liquid flow and electrical bias, which can be used for battery research and other energy systems like fuel cells [312] and electrocatalysts [313].

It can be used for *in situ* imaging and thus understanding fundamental processes like electrode material behaviors, dendrite formation, SEI during cycling [279][16][278][314] [315] [316] [317][318] [319], and to explore the effect of additives [315][316][317][318][319]. In this study, we mainly use the liquid cell TEM for characterizing metallic anode's morphological change over cycling.

3 Characterizing aging-induced anode degradation in aqueous zinc batteries

3.1 A Brief Background on AZB aging

As previously mentioned, the aqueous zinc battery (AZB) is a promising candidate for future grid-level energy storage [45][320][30][321][322]. And in particular, neutral and mildly acidic electrolyte systems like zinc sulfate ($ZnSO_4$) [36][75][323][100] has demonstrated good performance for potential commercialization [103][49][113][39][107][324][325][326].

A key advantage of the AZB is the stability of its metallic anode. Unlike other battery systems with highly reactive metallic anodes, metallic Zn can be directly used as anode in aqueous electrolytes. However, recent works on AZB have reported Zn anode degradation over prolonged cycling and aging [103][49][104][105][96][106][48]. This problem has been largely overlooked in the past. This is because most AZB research, including those focused on cathode or electrolyte, and even investigations on the metallic Zn anode, have employed Zn anodes with excess capacity. This excess capacity is used to offer a deep zinc reservoir for replenishment of lost capacity due to cathode degradation. However, as the result of this set-up, any anode capacity loss over cycling or aging can be hardly noticed from the cell's electrochemistry data and is therefore hidden and usually overlooked: a typical commercial Zn foil used in AZB studies is of 0.25 mm thick, equivalent to an anode capacity loading of around 150 mAh cm^{-2}; much higher than that of a practical battery. And when paired with a cathode of 1 to 4 mAh cm^{-2} capacity, these full cells' cathode to anode loading ratio can be as low as 1:150, making any Zn anode capacity loss hardly noticeable even after prolonged cycling.

To achieve a higher and more commercially acceptable energy density for future practical cells, AZBs need to have a higher cathode to anode capacity ratio to optimize its anode energy density; indeed, the

metal Zn anode's theoretical capacity of 820 mAh g^{-1} (or 5854 mAh L^{-1}) [45][320][30] can only be fully utilized once a 1:1 cathode to anode ratio is reached. Therefore, when studying Zn anodes, it is important to control the anode capacity loading level, so their performance is more representative of that of commercial cells [102]. By doing so, their degradation processes and capacity loss can also be better tracked and quantified during cycling or aging, as demonstrated in lithium metal battery studies[121][327][119][121][327].

Therefore, in this work, by using a metallic Zn anode with controlled loading, we aim to better diagnose, decouple, and quantify different metal anode degradation processes that occurs during aging in zinc sulfate electrolyte, based on which improved strategies can be developed to mitigate these problems.

3.2 Experimental conditions

3.2.1 Material Preparation

Glass fiber paper (0.26 mm thick), Ti foil (0.125 mm thick) and Zn Foil (0.25 mm & rolled to 0.1 mm thick) were purchased from Sigma Aldrich and were punctured into circular disks of 19 mm diameter (Glass fiber & Ti) and 16 mm diameter (Zn) to be used in the coin cells. All other LIR 2032-coin cell components were purchased from MTI Corporation. 2M $ZnSO_4$ electrolyte was also purchased from Sigma Aldrich.

3.2.2 Coin Cell Assembly

Zn/Ti cells assembled as shown in Figure 3.2.2.1. Ti was used as the current collector as it is highly inert to Zn deposition, as it neither alloys with Zn nor acts as a galvanic cathode; a galvanic cathode such as steel greatly accelerates Zn corrosion in water [328][329][330][331]. Unless stated otherwise, tests were performed with a standard Zn capacity loading of 4 mAh cm^{-2} and a rate of 10 mAh cm^{-2}. The same

current density was used during the charging stage and the discharging stage, i.e. plating and stripping. Each test was repeated with three-coin cells to ensure results' consistency. Cells tested solely for electrochemistry data for quantification are assembled with only a single separator while all cells used for MS, XRD, Optical examination are assembled with double separators and only the separator facing the anode side was examined in these tests. This it to decouple the anode side reactions from the counter side, i.e. to avoid detecting any possible products from side reactions at the counter electrode.

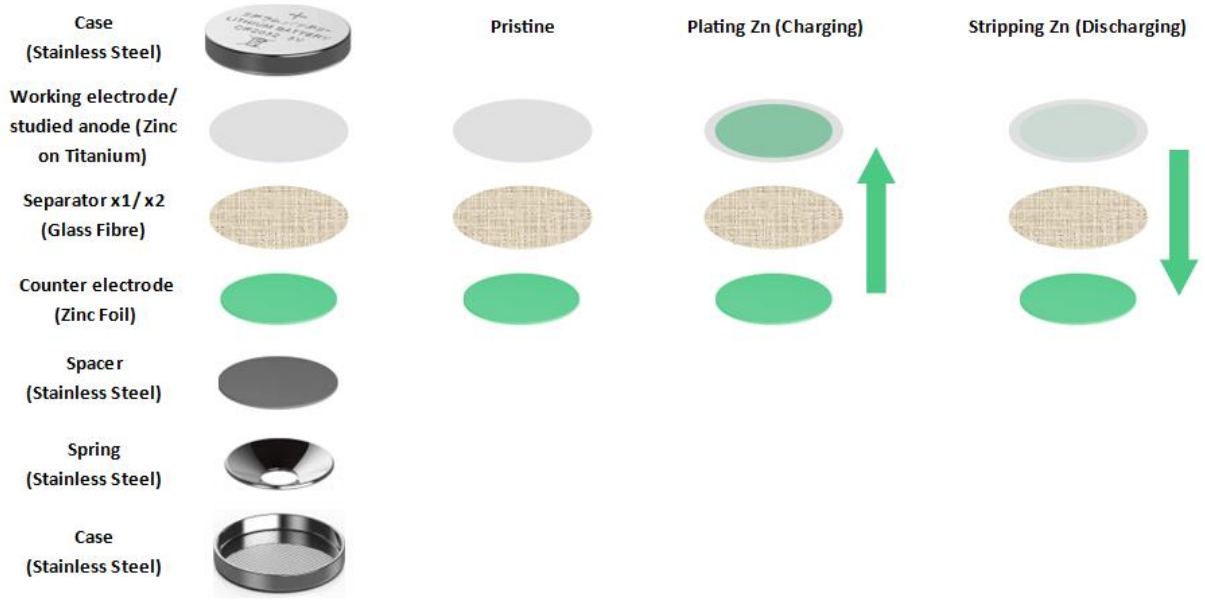


Figure 3.2.2.1 *Zn/Ti Coin cell set-up used for aging quantification, XRD, optical and MS tests. (Double separators used for XRD, optical and MS tests).*

3.2.3 X-section SEM and EDS

SEM was performed using a Carl Zeiss Merlin SEM using the secondary electron detector coupled with an energy dispersive X-ray spectroscopy (EDS) detector for element identification and mapping. A Gatan PECS II, a broad beam Ar ion mill, was used to polish the cross-section for SEM and EDS mapping.

3.2.4 X-ray photoelectron spectroscopy (XPS)

XPS measurements were conducted using a PHI5000 Versa Probe III instrument (Ulvac-PHI, INC.). An Al monochromatic source was used to generate X-ray with Power of 25W, voltage of 15kV and a beam diameter of 100 micron. A pass energy of 55 eV was set for the analyser.

An electron neutralizer gun was used to prevent any surface charge build-up. Before test, the sample surface was sputter-cleaned with an Ar+ ion source of 2kV, 1.8 µA and a raster size 3x3 mm2 for 5 seconds. The obtained spectrum was calibrated to the signal of adventitious carbon at 284.8 eV and the analysis and fitting were done using CASAXPS software.

3.2.5 XRD

XRD was performed using a Cu source Rigaku diffractometer with '2Θ' from 10 to 150 degrees with a step size of 0.01 degree.

3.2.6 Online Mass Spectroscopy

A Thermo Fischer quadrupole mass spectrometer with Ar carrier gas flown at a constant rate of 1 µl min^{-1} was used to count the gas evolution. MS is used in this study to quantify two things: 1) the ZHS/ZHO formed during aging, 2) 'inactive Zn' formed during aging.

For quantifying the ZHS/ZHO, the set-up is shown in Figure 3.2.6.1: A sealed 2-electrode cell (Zn/Ti) was connected to the MS. Electrolyte was quickly injected and 4 mAh cm^{-2} was plated into the Ti. The cell was then tilt so that only the Ti anode with Zn deposition was still left in the electrolyte (This is to minimize the aging process and the resultant H2 evolution from the counter electrode side to make sure

what we measured solely came from the aging of the anode). And by periodically counting the H_2 signal, we can calculate how much ZHS/ZHO have formed on the anode during that aging period.

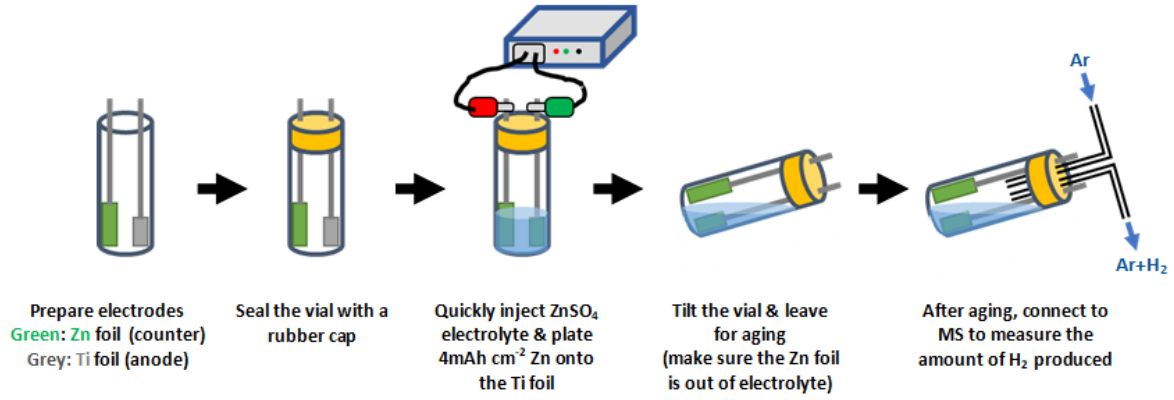


Figure 3.2.6.1 *in-situ two-electrode cell set-up connected to MS used for quantifying ZHS/ZHO formation during aging.*

For quantifying the 'inactive Zn', each post-aging-and-stripping coin cell was carefully dissembled right after discharge, the anode (with Ti) and the separator facing the anode was sealed in a vial connected to MS. And by injecting 10 mL of 10% H_2SO_4 into the vial to consume all the Zn metal, the resultant H_2 count can then be used to quantify the residual 'inactive Zn' using the following equation:

$$H_2SO_4 + Zn \rightarrow ZnSO_4 + H_2 \quad \text{(Equation 3.2.6.1)}$$

3.2.7 X-ray Computed Tomography

In situ X-ray computed tomography experiments were carried out using a Zeiss Xradia 610 Versa X-ray microscope. X-ray with an acceleration voltage of 160 kV and a power of 25 W were applied to capture

the whole Ti electrode. Since coin cell's relatively large size and metallic casing can lead to high attenuation and thus compromised resolution, in this study, Ti/Zn pouch cells with electrode diameter of 7 mm were used for XCT. For the pressured Zn/Ti pouch cell, two acrylic plates were used to clamp the poach to apply a constant pressure to the cell throughout the cycle, 3201 projections with an exposure time of 5.7 s were taken over 360° for each tomogram, resulting in a voxel size of 5.31 µm. For the pressure-free Zn/Ti pouch cell, 3201 projections with an exposure time of 4.3 s were taken over 360° for each tomogram, resulting in a voxel size of 5.08 µm. The tomogram data were reconstructed using Zeiss Scout and Scan Control System Reconstructor into 16-bit TIFF image stacks. The reconstructed images were segmented using Avizo Software. For both samples, region of interest was cropped in ImageJ, and the cropped TIFF image stacks were first transformed into raw data format, and opened and filtered by nonlocal means filter in Avizo. The rigid body movement among different in situ tomograms was then removed. Three phases, i.e. Ti, Zn, and void, were segmented out based on their different grayscale. Volume Rendering was applied to visualise the 3D segmented results.

3.2.8 Degassing test

Degassing was performed by immerging an aged and discharged cell in the $ZnSO_4$ electrolyte after a crack was deliberately made on the coin cell by grinding off its edge using a 400-grid grinding paper.

3.3 Results and Discussion

3.3.1 Quantifying anode capacity loss with respect to aging time, current density and separator

Inspired by the Cu/Li cells used in most efficiency studies for lithium metal anode [102][121][327][121], Zn/Ti coin cell were used in our study for quantifying post-aging anode capacity change. The Ti current

collector was first electroplated with exactly 4 mAh cm^{-2} of Zn, a common anode loading level in commercial batteries, which then served as our Zn anode.

After the Zn electrodeposition, the cells were left to age at ambient conditions for various amount of time before being discharged to +0.6V vs Zn/Zn^{2+} to strip all the Zn metal left on the anode using the same current density. This process is shown in Figure 3.3.1.1.

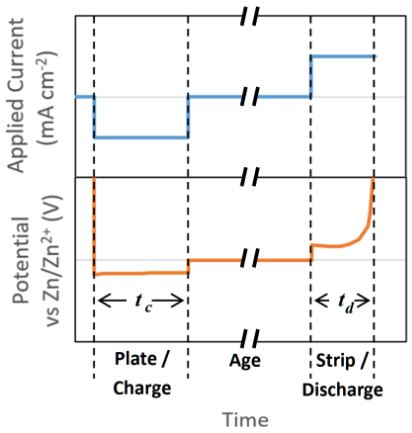


Figure 3.3.1.1 *Electrochemical test sequence for quantifying aging-induced capacity loss for Zn/Ti coin cell.*

The time spent to charge, t_c, and time spent to d ischarge, t_d can then be used to calculate the coulombic efficiency (CE), i.e. the post-aging reversibility of each cell:

$$\boldsymbol{CE = {t_d}/{t_c} \times 100\%} \qquad \textbf{(Equation 1)}$$

And the anode capacity loss due to aging, C_a, is quantified as the capacity difference between the charging and discharging processes:

$$\boldsymbol{C_a = \frac{t_c - t_d}{t_c} \times Q_{load}} \qquad \textbf{(Equation 2)}$$

Where Q_{load} is the anode loading

Firstly, by using a fixed anode loading of 4 mAh cm^{-2} and a constant change/discharge current density of 10 mA cm^{-2}, we tried to decouple and quantify the effect of aging time: it was found that none-aged cells, i.e. discharged immediately after charging without any aging time, yielded a relatively high reversibility of 99.2%. However, cells underwent 24 hours of aging before discharging, suffered a significant capacity loss of 1.03 mAh cm^{-2} (25.6%). And longer aging times led to further performance decay, with capacity loss of 1.18 mAh cm^{-2} (29.4%) after 48 hours of aging and 1.37 mAh cm^{-2} (34.2%) after 120 hours of aging. The sample charging/discharging curves are shown in Figure 3.3.1.2.

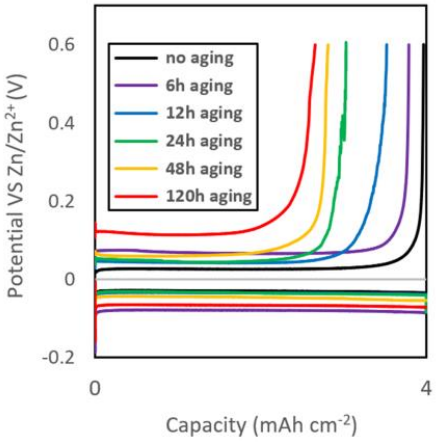


Figure 3.3.1.2 *Sample charge & discharge curves for cells aged for different lengths of time. The charge and discharge rates were 10 mA* cm^{-2}

To explore the effect of current density on the post-aging anode capacity change, we also repeated the same experiments using different current densities, which are compared in Figure 3.3.1.3.

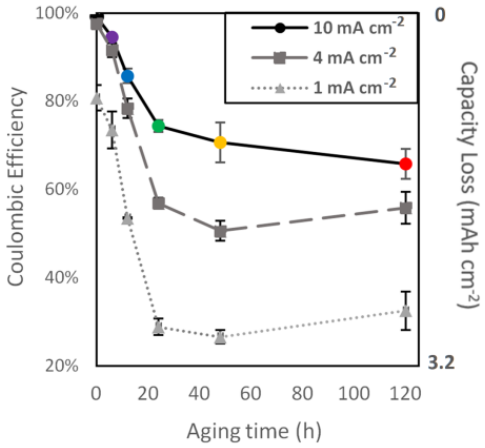


Figure 3.3.1.3 *Cells' post-aging CE and capacity loss with respect to different aging time and three different charge rates: 10 mA cm^{-2}, 4 mA cm^{-2} and 1 mA cm^{-2}. Each data point shows the average from three coin cells with error bars indicating the value variation range*

It was found that this aging-induced capacity loss was more significant in cells that were charged at lower rates: cells charged at 4 mA cm^{-2} and 1 mA cm^{-2} suffered significantly higher loss of 1.73 mAh cm^{-2} (44.1%) and 2.85 mAh cm^{-2} (71.1%), respectively after 24-hour aging. This is rather counterintuitive since in most battery systems, a low cycling rate usually leads to less parasitic reactions that can cause anode capacity loss. After careful examination of the post-charging Zn anode using SEM, we realized that this rate-dependency is likely the results of anode surface morphology, as shown in Figure 3.3.1.4:

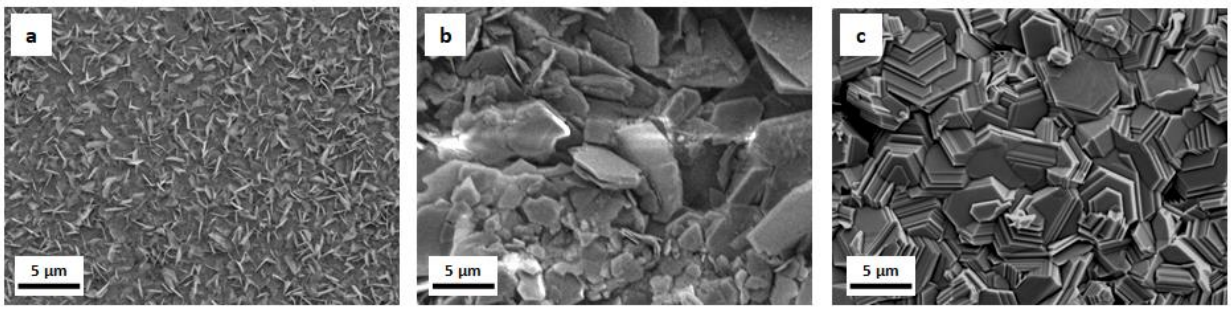


Figure 3.3.1.4 *Different Zn surface morphology deposited at different rates: a) 1 mA cm^{-2} b) 4 mA cm^{-2} c) 10 mA cm^{-2}*

Figure 3.3.1.4 shows that Zn electroplated at higher current densities exhibits a monolithic crystalline morphology with a low overall surface area while Zn plated at lower rates instead deposit as high surface area flakes, which is consistent with previous works on electroplating Zn [332]. The larger surface area for Zn electroplated at lower current density can host more aging-related parasitic reactions which is likely the cause of more capacity loss.

We also explored the effect of separator thickness on the aging-induced capacity loss, by repeating the aging tests using cells with double separators under the same loading and rate conditions: 4 mAh cm^{-2} loading with 4 mA cm^{-2} rate. It was also found that cells assembled with double separators suffered greater losses than those with one single separator when cycled and aged under the same conditions as shown in Figure 3.3.1.5. This observation is also rather unexpected since the separator thickness has never been reported to have such significant effect on the cell reversibility in any battery systems. And the reason behind this separator dependency in AZB cells will be further explained later.

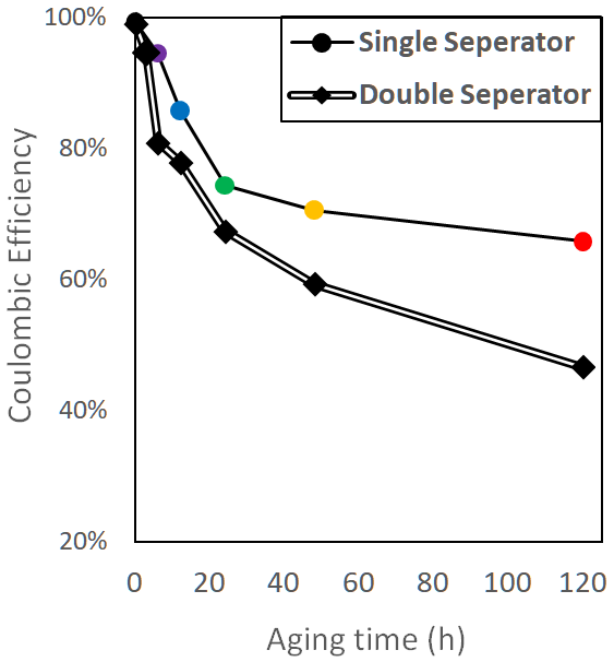


Figure 3.3.1.5 *Coin cells' post-aging CE and capacity loss (average from 3 coin-cells) with single/double separators. Charging condition: 10 mA cm^{-2} with 4 mAh cm^{-2} loading*

3.3.2 Identifying and quantifying capacity loss due to ZHS/ZHO formation

This unprecedented quantification has shown that the Zn anode capacity loss due to aging is both rapid and significant, which presents a rather pressing obstacle for the future commercialization of AZBs. To help design appropriate strategy for this issue, we first need to diagnose thus understand its underlying degradation processes.

As previously mentioned in Section 1.3, previous works have demonstrated metallic Zn anodes in in $ZnSO_4$-based AZBs suffer from dendrite formation [113][114][11][47] and corrosion [104][96][106][48][108]. Since dendrite formation is an electrochemical process that only takes place during electroplating and does not occur spontaneously by simply immersing Zn anode in electrolyte, it is unlikely the cause of this aging-dependent capacity loss we observed.

Corrosion, on the other hand, has been reported to lead to the formation of zinc hydroxide (ZHO), i.e., $Zn(OH)_2$, and zinc hydroxide sulfate hydrate (ZHS), i.e., $Zn_4SO_4(OH)_6{\cdot}xH_2O$ [96][106][48][108], on the anode surface, as previously shown in Section 1.3.1:

$$Zn + 2H_2O \rightarrow Zn(OH)_2 + H_2 \text{ (Equation 1.3.1.1)}$$

$$3Zn(OH)_2 + ZnSO_4 \cdot xH_2O \rightarrow Zn_4SO_4(OH)_6 \cdot xH_2O \text{ (Equation 1.3.1.2)}$$

The formation of ZHS and ZHO occurs at the cost of irreversible consumption of metallic Zn, potentially causing the anode capacity loss we observed. So, to confirm this hypothesis, the post-aging metallic Zn anodes were characterized using XPS:

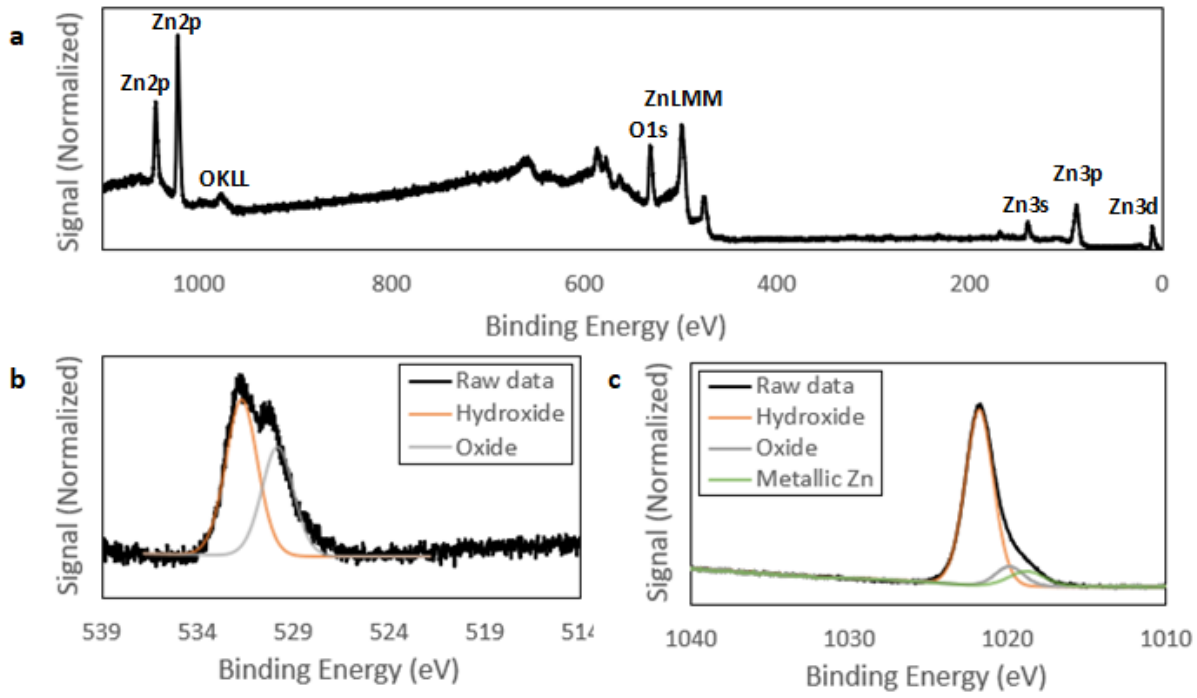


Figure 3.3.2.1 *XPS spectrum showing the surface chemistry of the plated Zn on Ti after 5 days of aging following electroplating for 4 mAh cm^{-2} at 10 mA cm^{-2}, indicating hydroxide and oxide formation due to corrosion reactions. (a) Full-range spectrum (b) O1s signal and related chemical species' peak fitting (c) Zn2p signal and related chemical species' peak fitting.*

It can be seen from Figure 3.3.2.1 that the post-aging Zn anode surface developed a significant oxygen signal which is still visible after a 5-second surface cleaning with ion sputtering. And further elemental scans on O1s and Zn2p all revealed multiple O and Zn chemical environments. By cross-referencing the existing data base, the fitting of these cutting indicates the presence of oxide and hydroxide, which suggests the formation of ZHO and ZHS.

XRD were used to further confirm their presence, as shown in Figure 3.3.2.2, which confirmed the formation of ZHO and ZHS during aging.

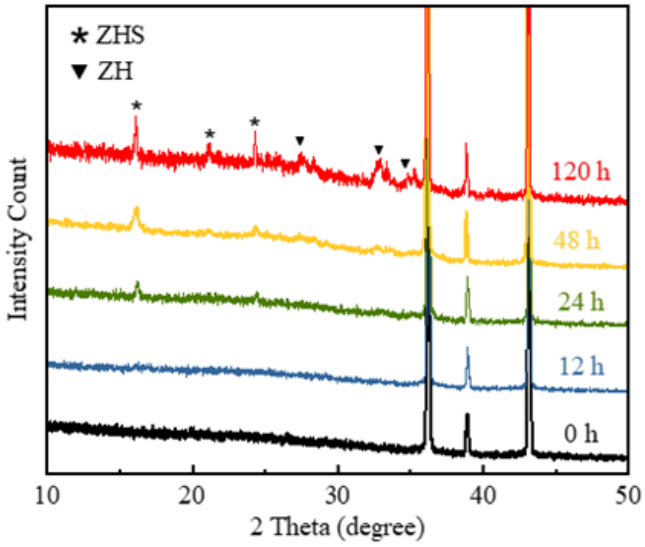


Figure 3.3.2.2 *XRD of electrodeposited Zn after different aging time, showing the gradual development of ZHS and ZHO. Charging condition: 10 mA cm^{-2} with 4 mAh cm^{-2} loading*

It can be seen from Figure 3.3.2.2 that the ZHO and ZHS signal gradually increases with increased aging time, this suggests that ZHO and ZHS will continuously growth during aging, potentially leading to the growing capacity loss we observed in Section 3.3.1.

To further quantitatively confirm that the irreversible formation of ZHS/ZHO is indeed the root cause of the significant capacity loss we observed, we employed an in-situ cell connected to the MS to periodically measure the H_2 evolution from the anode after the cell was charged and aged for different amount of time. And by using Equation 1.3.1.1, we can then accurately quantify the metallic Zn loss due to ZHS/ZHO formation with respect to different aging time. The Results is shown in Figure 3.3.2.3:

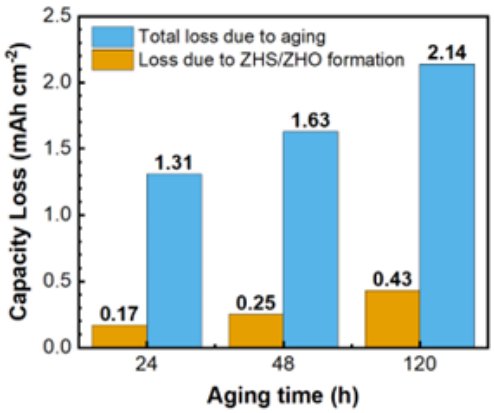


Figure 3.3.2.3 *Comparison of the Zn anode capacity loss due to ZHS/ZHO formation, measured using MS, and the total anode loss, measured electrochemically, with respect to different aging times*

Figure 3.3.2.3 shows that although the ZHS/ZHO amount increased continuously during aging, which is consistent with the previous XRD results, their their formation only contributed to less than 20% of the total anode capacity loss: only 0.17 mAh cm^{-2} (out of 1.31 mAh cm^{-2}) anode Zn loss was due to ZHS/ZHO formation after the 24-hour aging, and only 0.43 mAh cm^{-2} (out of 2.14 mAh cm^{-2}) loss was due to ZHS/ZHO formation after the 120-hour aging.

This discrepancy is also revealed from the cross-section SEM images and EDS mapping in Figure 3.3.2.4:

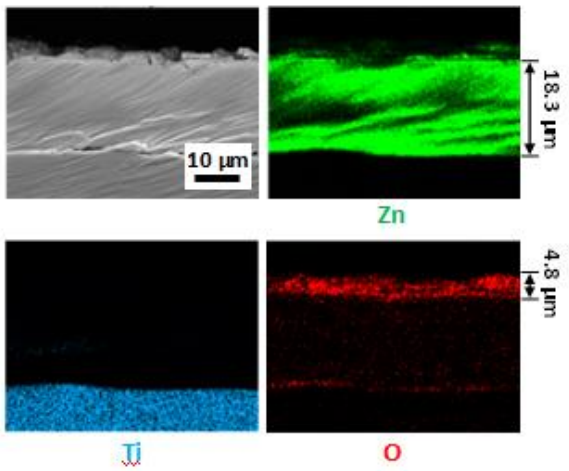


Figure 3.3.2.4 *Cross-section SEM imaging and EDS mapping (O, Zn, Ti) of plated Zn on Ti after 5 days of aging following electroplating to 4 mAh cm^{-2} at 10 mA cm^{-2}, Regions with strong O signal segregation indicates high likelihood of ZHS/ZHO formation*

Figure 3.3.2.4 shows that, even after 120h of aging, only a relatively thin layer of ZHS/ZHO (O rich region) had formed on top of the electroplated metallic Zn with a thickness of around 4.8 µm. A significant amount of metallic Zn with a thickness of 18.3 µm were preserved after the aging. This corroborates with the MS results and confirms that only a relatively small proportion of the total available Zn was consumed during aging to form ZHS/ZHO, which cannot be solely responsible for the aging-induced capacity loss we observed and therefore some other processes must have contributed to the loss.

3.3.3 Identifying the formation of aging-induced 'inactive Zn'

To explore what is the main contributor to the aging-induced capacity loss, post-aging-and-discharged cells were disassembled and examined carefully visually and via XRD:

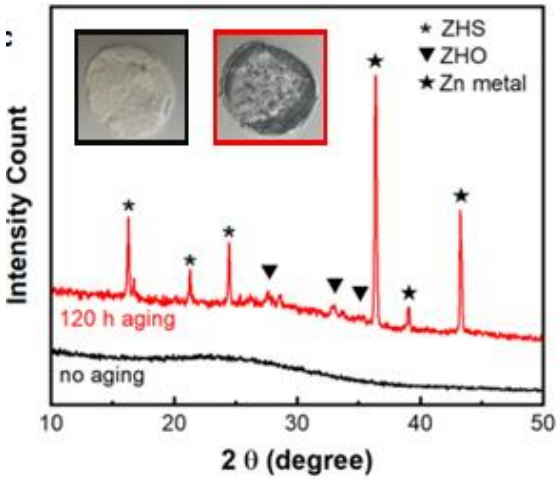


Figure 3.3.3.1 *Photographs and XRD of cell separators following stripping, with 4 mAh cm^{-2} electrodeposition at 10 mA cm^{-2}. Red border: with 5-day aging, black border: without aging.*

Figure 3.3.3.1 revealed a significant amount of residual metallic debris on the Ti current collector and the separators of the aged cells (red box) while little debris was found in the unaged cells (black box). And XRD measurements from these aged and stripped anodes on the Ti current collectors identified these residues as Zn metal. This suggests that parts of the plated zinc anode, beyond the fraction already converted to ZHS/ZHO and that had instead remained metallic, had fallen 'inactive' during the aging process and could not be stripped. These 'inactive Zn' resemble the 'dead Li' commonly reported in lithium metal batteries[15][333][334][335][336]. However, 'dead Li' in LIBs forms mostly due to dendrite formation and detachment, which only takes place during cycling and is independent of aging. Therefore, since our observed 'inactive Zn' correlates strongly with aging instead of cycling, its formation is unlikely to be due to dendrite detachment.

3.3.4 Quantifying capacity loss due to aging-induced 'inactive Zn' formation

For the first time, we have discovered the formation of aging-induced 'inactive Zn' in AZBs. However, before claiming its formation is the root cause of the significant capacity loss, again we need to quantify its amount and compare it to the aging-induced capacity loss we observed from cells' electrochemistry.

Using the titration set-up described in Section 3.2.6 and we were able to quantify the residual 'inactive Zn' in each cell after having undergone aging and electrostripping according to the following equation:

$$Zn_{(s)} + H_2SO_{4(aq)} \rightarrow ZnSO_{4(aq)} + H_{2(g)} \uparrow \qquad \text{(Equation 3.3.4.1)}$$

By measuring the H2 amount, we can calculate the amount of 'inactive Zn' which is shown in Figure 3.3.4.1:

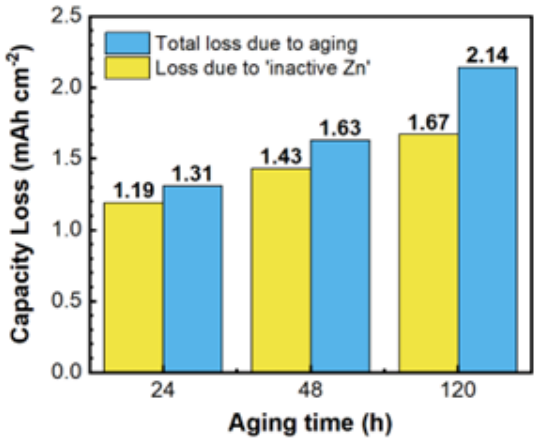


Figure 3.3.4.1 *the capacity loss due to 'inactive Zn' formation, measured using H_2SO_4 titration, and the total anode loss, measured electrochemically, with respect to aging time. All plating were performed at 10 mA cm^{-2} rate and to 4 mAh cm^{-2} capacity.*

Figure 3.3.4.1 shows that the amount of inactive Zn' formed within the aged cells are rather significant and actually account for over 80% of the total measured aging-induced capacity loss we observed: an average of 1.19 mAh cm^{-2} (out of 1.31 mAh cm^{-2}) of 'inactive Zn' was detected after 24 hours of aging,

and 1.67 cm^{-2} (out of 2.14 mAh cm^{-2} total loss) of 'inactive Zn' was found after 120 hours of aging. This confirms that the significant amount of aging-induced anode capacity loss was in fact most due to the formation of 'inactive Zn'.

3.3.5 Decoupling and quantifying different aging-induced degradation processes

Overall, using mass spectrometry, we have shown that the aging-induced capacity loss was mostly due to two degradation processes: (1) Zn loss due to ZHS/ZHO formation (Section 3.3.2), and (2) the formation of 'inactive Zn' (Section 3.3.3-3.3.4). Their percentage contribution to the loss with respect to aging time is summarized in Figure 3.3.5.1:

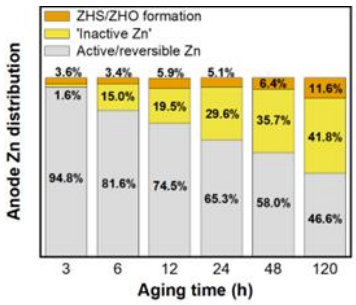


Figure 3.3.5.1 *The distribution of anode Zn after aging, between active (i.e., fully reversible) Zn, 'inactive Zn', and Zn lost to ZHS/ZHO formation, with respect to aging time, all plating were performed at 10 mA cm^{-2} rate and to 4 mAh cm^{-2} capacity.*

Figure 3.3.5.1 shows that both degradation processes take place continuously during aging, leading to increasingly compromised Zn anode reversibility with longer aging times. Between the two, the 'inactive Zn' is the more significant contributor to capacity loss, a trend that becomes especially notable after longer aging time. The ratio of Zn distributed between fully reversible (active) Zn, 'inactive Zn', and Zn locked into ZHS/ZHO compounds, changes markedly with increasing aging anode aging time. After 3

hours of aging, the Zn anode lost a total of 5.2% capacity, with 3.6% from ZHS/ZHO formation and only 1.6% from 'inactive Zn'. However, after only 6 hours of aging, 15.0% of the anode loss (out of 18.4% total loss) was due to 'inactive Zn'. And after 120 hours of aging, 'inactive Zn' contributed to a high average anode loss of 41.8% (out of 53.4% total loss).

So far, we have been using a fixed anode loading of 4 mAh cm^{-2}. To further explore and quantify these degradation processes in cells primed with various Zn capacities, four Zn anodes loads were studied, charged with capacities of 1, 2, 4, and 10 mAh cm^{-2}, and all plated at a rate of 10 mA cm^{-2}. As before, following aging these cells were discharged at 10 mA cm^{-2} until reaching a voltage threshold of +0.6V vs Zn/Zn^{2+}. The comparison among these different loadings are shown in Figure 3.3.5.2.

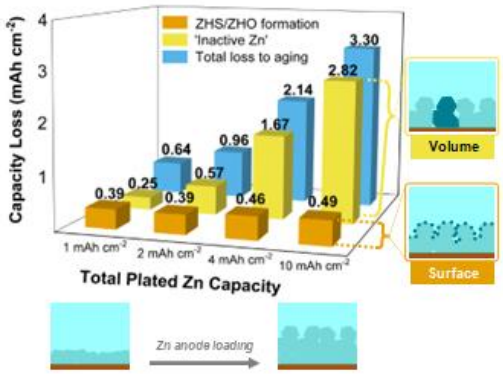


Figure 3.3.5.3 *The total capacity loss with different levels of Zn loading following 5 days of aging. Total loss consists of the loss due to 'inactive Zn' and loss due to ZHS/ZHO formation. all plating and stripping were performed at 10 mA* cm^{-2} *rate*

Figure 3.3.5.3 shows that the absolute Zn capacity loss due to ZHS/ZHO formation is roughly the same for all these tested cells regardless of the anode loading (orange bars): it merely changed from 0.39 mAh cm^{-2} to 0.49 mAh cm^{-2} when the anode loading is substantially increased by ten times from 1 mAh cm^{-2} to 10 mAh cm^{-2}. In comparison, the absolute Zn capacity loss due to 'inactive Zn' formation is much

more dependent on the anode loading. For cells with higher anode loading, Zn capacity loss is higher (yellow bars): Cells with 1 mAh cm^{-2} Zn anode loading only formed 0.25 mAh cm^{-2} 'inactive Zn' after 120 hours of aging, which increased to 0.57 mAh cm^{-2} of 'inactive Zn' in cells with 2 mAh cm^{-2} loading, 1.67 mAh cm^{-2} with 4 mAh cm^{-2} loading, and 2.82 mAh cm^{-2} with 10 mAh cm^{-2} anode loading.

This discrepancy of dependency on the anode loading indicates a key difference between the two degradation types: the capacity loss due to ZHS/ZHO is mostly anode surface dependent while the capacity loss due to 'inactive Zn' is more anode volume dependent. The ZHS/ZHO formation is an interfacial reaction between the metallic Zn anode and the $ZnSO_4$ electrolyte, which is therefore solely dependent on the interfacial surface area, and independent of the thickness of the loaded Zn; higher plating capacities lead to relatively small change in Zn surface area, instead serving to simply thicken the Zn layer deposited on the current collector. The contrasting behavior in the quantity of 'inactive Zn' formed, which instead exhibited a concomitant increase with higher loading level, suggests that its formation mechanism is a process that acts to deactivate whole volume sections of the plated anode, rather than being confined to a surface reaction by-product. And this volume dependent loss from 'inactive Zn' can only be fully explained once we understand what its root cause is.

3.3.6 Uncovering the formation mechanism of aging-induced 'inactive Zn'

To uncover the root cause of these aging-induced 'inactive Zn', X-Ray Computed Tomography (XCT) was employed to capture their formation process. A Zn/Ti pouch cell was examined in-situ with its anode closely monitored while undergoing a full cycle of charging, aging, and discharging under a constant pressure, this is demonstrated in Figure 3.3.6.1 a-h.

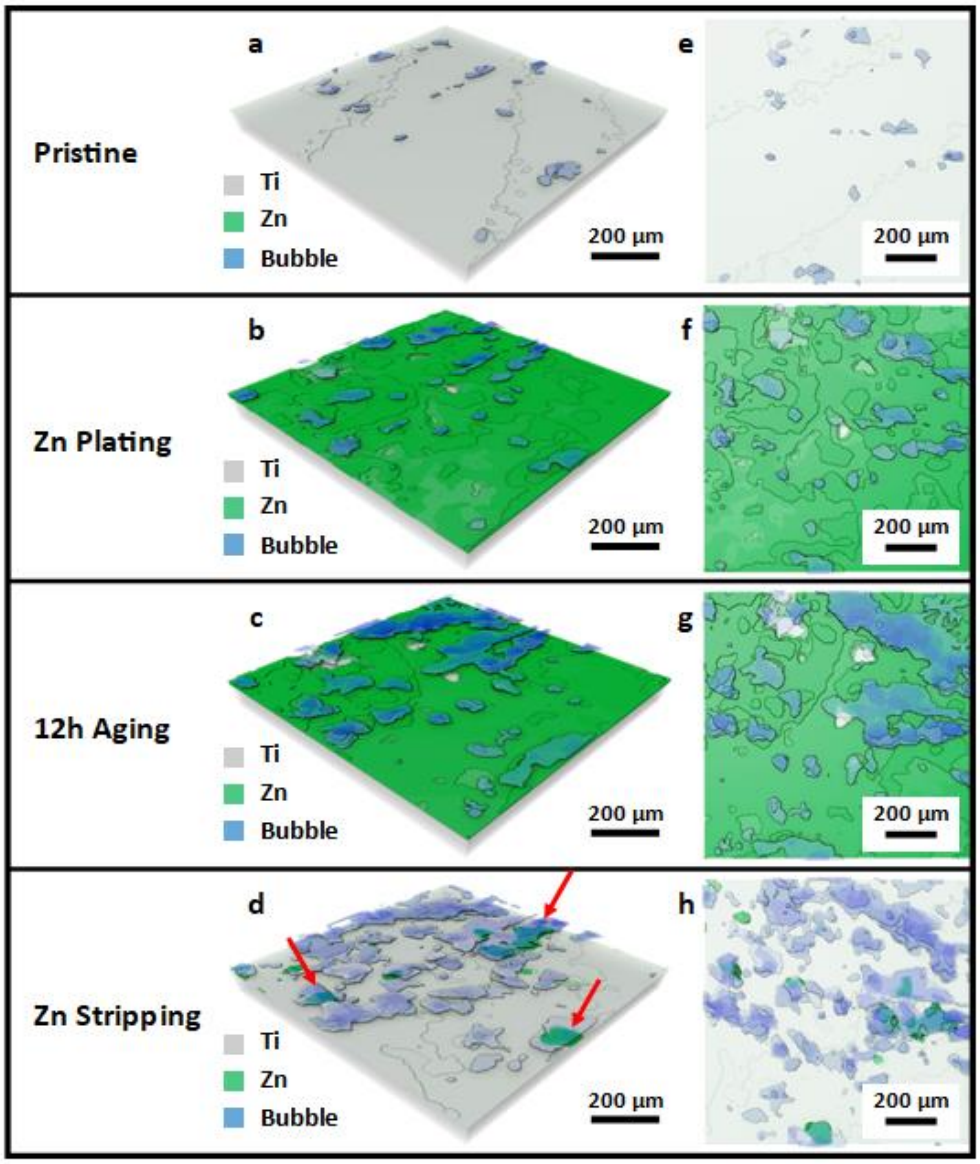


Figure 3.3.6.1 *(a-h) The anode of a pressured Zn/Ti pouch cell scanned in-situ using XCT, imaged through a full cycle of (a,e) pristine, (b,f) charging, (c,g)12 hours of aging, and (d,h) discharging. (a-d) 3D rendered images from a side view angle. (e-h) 3D rendered images from top view. Cells were charged & discharged at 10 mA cm^{-2} rate & have 4 mAh cm^{-2} anode Zn loading.*

Figure 3.3.6.1 shows that the pristine anode, after cell assembly, had a clean surface (a & e) with only a few sporadic bubbles on the Ti current collector, these are likely gas trapped within the pouch, by the

separator during assembly. This clean Ti surface allowed a uniform Zn electrodeposition upon charging (b & f). Once Zn has been electroplated onto the Ti, new gas bubbles started to form on the plated Zn (b & f), which then gradually grew and merged into larger bubbles after 12 hours of aging (c & g). These bubbles were likely H_2 formed during the anode corrosion process outlined in Equation 1.3.1.1 ($Zn + 2H_2O \rightarrow Zn(OH)_2 + H_2$). Upon discharging (Figure d & h), most of the plated Zn was unaffected by the bubbles and could be completely stripped, re-exposing the underlying Ti current collector. However, parts of the plated Zn anode, obscured underneath the larger bubbles, were unable to be stripped and became 'inactive' (marked by the red arrows in d), resulting in the residual 'inactive Zn' we observed in Section 3.3.3.

This process is more prominent in cells with lower pressure and longer aging time, as demonstrated in Figure 3.3.6.2.

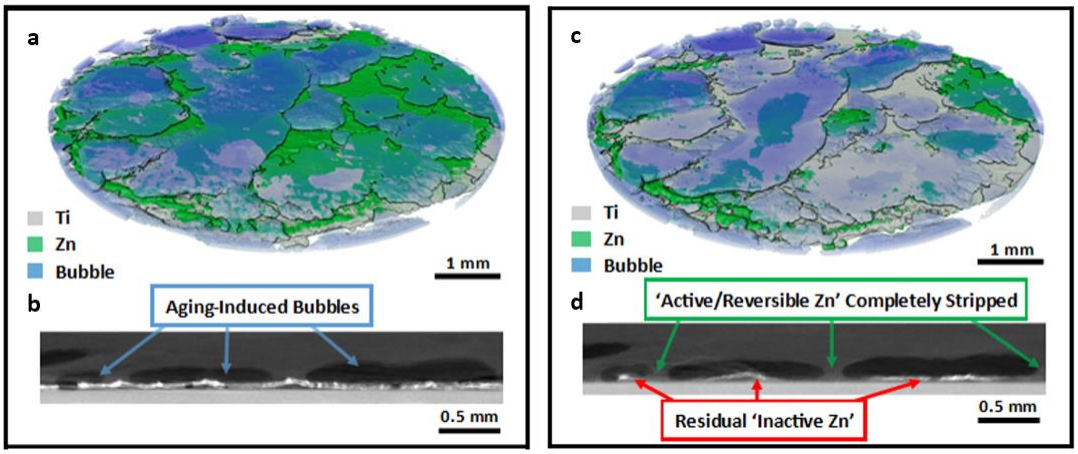


Figure 3.3.6.2 *Anode of a pressure-free Zn/Ti pouch cell (a-b) after charging and 48 hours of aging, and (c-d) after discharging. (a,c) 3D rendered images from side view (b,d) cross-sections of in situ tomography scans. Cells were charged & discharged at 10 mA cm^{-2} rate & have 4 mAh cm^{-2} anode Zn loading.*

Figure 3.3.6.2 compares the post-plating-and-aging cell's Zn anode surface before and after stripping. We can see that after 48 hours of aging in a pressure-free environment, a greater number of bubbles with larger sizes could be seen across the anode surface (a). This, after stripping, resulted in significantly more 'inactive Zn' remaining on the anode surface (c). From the cross-sections of the in-situ tomography scans, the bubble-induced 'inactive Zn' formation process can be clearly visualized: During aging, bubbles formed, grew and merged across the anode surface, physically displacing the electrolyte away from the plated Zn. These regions of the interface no longer had contact with the $ZnSO_4$ electrolyte (b). As a result, during stripping, only those regions on the anode surface where the electrode-electrolyte contact was maintained were able to remain 'active' and undergo dissolution (green arrows in d), while those areas where bubbles displaced the electrolyte, breaking the interfacial contact and ionically insulating the plated Zn from the electrolyte, could not undergo stripping. These screened areas of the anode were thus eventually left as residual 'inactive Zn' remnant on the Ti current collector (red arrows in d), causing capacity loss. This problem is more prominent at lower cell pressure when the space is less confined so the bubbles can form and merge more easily. This can also be used to help explain the difference between single-separator cells and double-separator cells: in the double-separator cells, under the same cell pressure, there is more inter-electrode space, which provides more room and freedom for bubble accumulation and coagulation.

So far we can see that, longer aging time leads to more H_2 evolution, promoting more bubble growth, while lower cell pressure results in higher bubble mobility, promoting bubble mergence into larger ones better able to screen the anode and thus increase 'inactive Zn' formation. This bubble accumulation on the Zn anode is not reversible, as the cell is sealed and the gas cannot be removed. Over repeated cycles the accumulated bubbles will reduce the effective surface area of the Zn anode available for subsequent cycling due to physically displacing the electrolyte away from the anode, which as well as causing the

isolation of 'inactive Zn', will also lead to localized points of high current density [114][11][172] during plating that will accelerate other anode issues like dendrite formation.

3.3.7 Reactivating the 'inactive Zn' by removing the built-up gas

However, after establishing that the 'inactive Zn' is the main cause of the aging-induced capacity loss, a key follow-up question is whether this 'inactive Zn' is reversible. Therefore, a degassing test was performed on a coin cell following aging and stripping. The degassing was performed simply by making a small opening by grinding the edge of the coin cell and immersing the cell in the electrolyte. The result of which is shown in Figure 3.3.7.1:

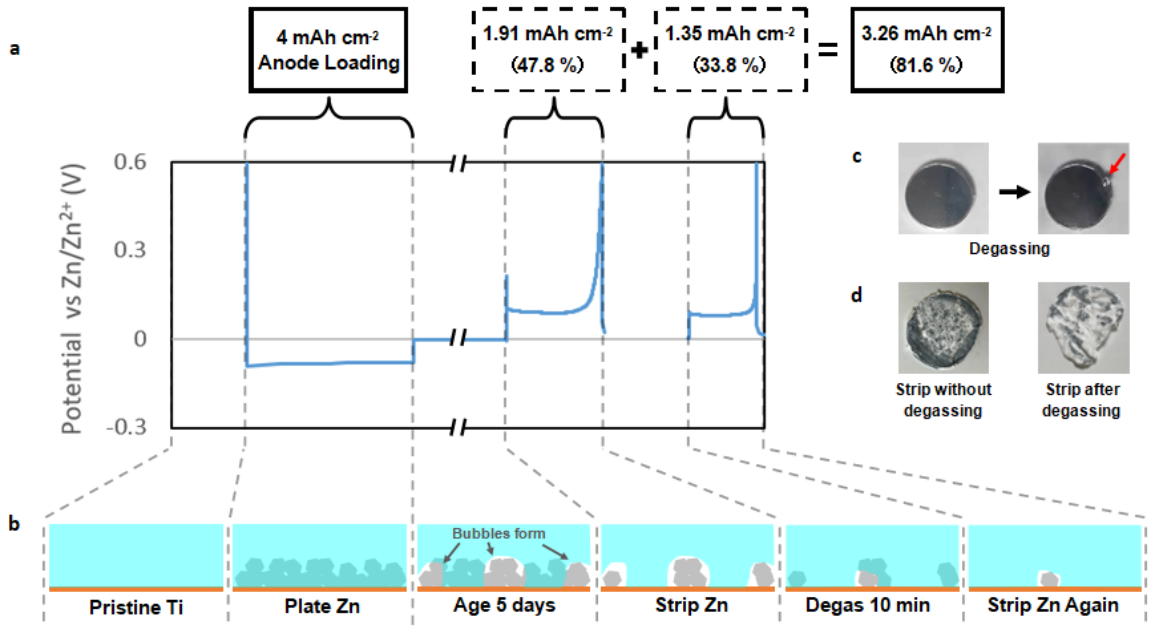


Figure 3.3.7.1 *(a) The applied test sequence for a degassing test on a Zn/Ti coin cell, including anode Zn loading, 5 days of aging, initial electrostripping, degassing and post-degassing electrostripping. The plated capacity was 4 mAh cm^{-2}, and the stripped capacities were 1.91 and 1.35 mAh cm^{-2}, respectively. (b) Graphics illustrating the test sequence in (a). (c) Optical images showing gas evolution from the cell during degassing (red arrow). (d) Optical images showing reduced quantity of 'inactive Zn' on the separator due to degassing.*

By degassing, some of the bubbles generated during aging could be removed. And parts of the anode surface which previously became depleted of electrolyte due to electrolyte displacement by bubbles was replenished with more electrolyte after degassing. Figure 3.3.7.1 shows that, after 120 hours of aging, without degassing, only 1.91 mAh cm^{-2} (CE = 47.8%) of the 4 mAh cm^{-2} plated Zn remained active which could be stripped (a). However, after the cell being degassed in the electrolyte for 10 minutes to remove some of the H_2 bubbles accumulated on the Zn anode surface.

During degassing, even without applying any external pressure, a continuous stream of bubbles escaping from the coin cell could be observed (c), this indicated that the hydrogen evolution has led to a gradual internal pressure built-up within the coin cell during aging. After degassing, an extra discharge capacity of 1.35 mAh cm^{-2} could be retrieved from the cell, raising the overall cell's post-aging CE from 47.8% to 81.6%. And by comparing the disassembled cells with and without degassing, degassed cells were found to have significantly less residual 'inactive Zn' left on their separators and Ti current collector (d).

To conclude, this degassing test confirmed the formation mechanism of 'inactive Zn' being due to gas bubble accumulation at the anode interface, displacing the electrolyte from parts of the Zn anode and impeding ionic transfer. It has also shown that releasing the accumulated gas from the cell allowed for the 'reactivation' of the 'inactive Zn', as expulsion of the gas restored the electrolyte-electrode interface and thus permitted unimpeded ionic flow (b).

3.3.8 Aging-induced degradation project summary and future work

In this project, we have decoupled and quantified the Zn anode degradation processes in $ZnSO_4$-based AZBs with respect to different charging rates, anode loadings, separator and aging times. It was found that cell aging can lead to significant anode capacity loss, in some cases over 70% efficiency loss, after only 24 hours of aging, a phenomena that has never been reported and remained largely overlooked in

the past. This aging- induced loss was aggravated by use of longer aging time, higher anode loading, and lower charging rates, and ultimately led to poor post-aging reversibility and short cell shelf life. While the loss was found to be partly from the irreversible formation of zinc corrosion products like ZHS, it was mostly observed to be due to the presence of 'inactive Zn', accounting for over 80% of the aging capacity loss. Using in-situ XCT, we revealed that 'inactive Zn' formed due to gas bubble formation and accumulation at the anode interface during aging. The trapped bubbles displaced the electrolyte from parts of the Zn anode, effectively leaving some regions ionically insulated from the electrolyte and thus unable to be dissolved during electrostripping; i.e., they were rendered 'inactive' during discharge. We demonstrated that by simply degassing the cells, these 'inactive Zn' can be 'reactivated' to restore a significant portion of the lost capacity. Our results and model have demonstrated that to mitigate aging-induced degradation, a key consideration is to minimise gas build-up on the Zn anode. This can be achieved either by limiting gas formation, such as by applying a protective layer [104][96][106][108][97][141][98][337], modifying the electrolyte[105][97][338][339] or solid/gel electrolyte [340][341][342][343][344] to impede H_2 generation from corrosion, or by removing the formed H_2, by a flow-cell or degassing mechanism, or by adding hydrogen scavengers into the electrolyte. These different strategies shall be tested and optimized in the future to mitigate this issue.

4 Achieving ultrahigh-rate planar and dendrite-free zinc electroplating for aqueous zinc battery anodes

4.1 A Brief Background on the dendrite formation problem and related strategies in AZBs

Apart from the aging-induced degradation problem as we explored in Chapter 3, dendrite formation is also a commonly observed issue in AZBs, as previously described in section 1.3.3 and it is commonly believed to be the biggest challenge that limits the AZB's cycling behaviours, causing serious problems like poor reversibility, voltage hysteresis, increased parasitic reactions, shorting-induced battery failures and other issues. [40], [99], [302] These dendritic structures, either rarefied needle or non-planar platelet deposits, preferentially form at irregular or defective areas of the electrode where the localized current density is highest and the initial nucleation event is most likely,[345] and is exacerbated by cycling at high current densities and capacities.[47], [114] Strategies for controlling and suppressing dendritic growth have revolved around manipulating the electrolyte, typically by inclusion of additives,[97], [346]–[350] or by engineering the electrode into a high surface area sponge,[351]–[353] or with a protective surface coating,[98] in order to suppress dendrite formation.

An alternative approach which has been brought up recently is anode surface texture engineering to incentivize planar Zn deposition and growth, as a flat anode morphology is ideal for preventing dendrites and for achieving high cycling reversibility.[354], as previously mentioned in Section 1.3.4. This can be achieved via the controlled deposition of (002)-orientated Zn. The (002) Zn face is the lowest surface energy face at 0.02 eV $Å^{-2}$, nearly three times lower than that of the (111) and (101) faces.[147] As a result, Zn is generally formed as flat platelets. And it has been shown that using anodes with a semi-matching crystal lattice to that of Zn, for example graphene or Sn,[148]–[151] preferential Zn electrodeposition along the (002) orientation and parallel to the anode surface can be achieved.[126]

And their reduced nucleation barrier helped foster evenly distributed nucleation events and a more uniform plated surface.[149], [150]

One thing to notice is that, despite some improvements, fully planar plating could not be achieved in these studies, i.e. significant amount of non-planar structures were still observed with these innovative Zn anodes, as revealed by their SEM and XRD results. And these non-planar structures exist mostly around the edges of the electrodeposited Zn islands and other defective regions.[148], [149] And once these non-planar deposits form, they could disturb the homogenous landscape of the anode surface, impairing the preference toward uniform planar plating upon subsequent cycling[149], and thus ultimately limiting the electrode's ability to cycle repeatedly at high rates.

This study aims to further optimize this system by minimizing the nucleation and growth of non-planar zinc deposition on AZB anodes to maximize their long term cycling stability and efficiency.

4.2 Experimental conditions

4.2.1 Material Preparation

Rolled Polycrystalline Zn plates and three Zn single crystal disks (diameter 12 mm, 5 mm thickness) facing along (002) basal plane were purchased from Good-Fellow LTD. One of the single crystal disks was machined into four quarters via slow speed copper saw. The Polycrystalline Zn plates was cut into circular pieces with 12 mm diameter to ensure its areal current distribution and current density is equivalent to that of the Zn single crystals during testing. Both Polycrystalline Zn and Single crystal Zn samples were polished. Grinding and polishing of the Zn was performed on a Struers polishing machine using these parameters: 500 grits, 1200 grits grinding followed by 9 micron, 3 micron and 1 micron diamond suspension polishing. The resultant polished samples are shown here in Figure 4.2.1.1:

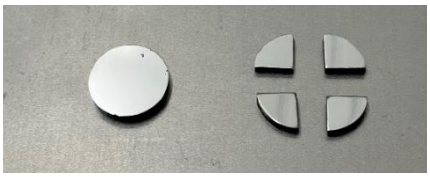


Figure 4.2.1.1 *machined and polished and single crystal Zn with (002)-orientation.*

Stainless steel, copper and Platinum foil were purchased from Sigma Aldrich. 2M $ZnSO_4$ electrolyte was also purchased from Sigma Aldrich.

4.2.2 Two-electrode beaker cell assembly

Due to the thickness of the commercial Single-Zn, it is tricky to used it as coin cell anode, therefore, two-electrode beaker cells were used in this study for plating and all electrochemical tests of different substrate materials. After polishing, Each sample was fixed onto an aluminium stub with silver-paste. The whole piece was then painted with Lacomit Varnish (Agar Scientific Limited), leaving only the centre of top surface exposed for electroplating or cycling. This is to make sure that electroplating only takes place on the (002) basal plane of the single crystal Zn and not on its side (The regions painted with Lacomit are not exposed to the electrolyte and thus are not subject to electroplating or cycling)

Galvanostatic plating and cycling was performed in a two-electrode closed beaker cell as illustrated in Figure 4.2.2.1, containing 2M $ZnSO_4$ aqueous electrolyte via a Gamry Reference 600 instrument under ambient conditions. Quarter-sized samples were used for plating-only experiments while full-size disks were used for cycling experiments. The working electrode and contour electrode were placed at 2 mm apart facing each other. A glass-fiber separator was clamped between the two electrodes during each 10 mA cm^{-2} cycling experiment. After each plating or cycling experiment, the cell was dissembled, and

each sample was removed from the lacomit and stub, and was rinsed with deionized water, acetone and isopropanol before further characterization.

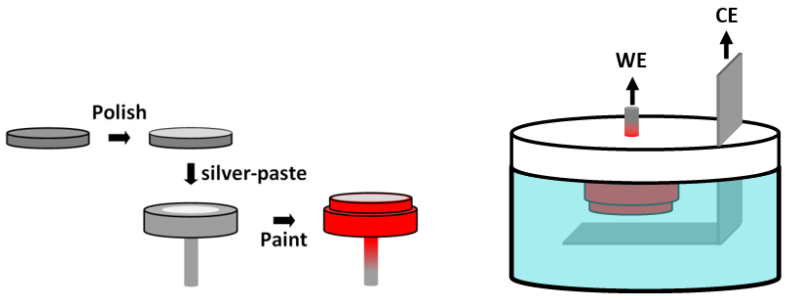


Figure 4.2.2.1 *how samples were prepared and tested in a two-electrode beaker cell.*

4.2.3 SEM and EDS

SEM was performed using a Carl Zeiss Merlin SEM using the secondary electron detector coupled with an energy dispersive X-ray spectroscopy (EDS) detector for element identification and mapping.

4.2.4 EBSD of post-plating/cycling anode surface

The samples' crystal orientation after electroplating was characterised using Zeiss Merlin field-emission gun SEM (FEG-SEM) which operates at 15 kV with a probe current of 15 nA, coupled with a BRUKER e-FlashHR EBSD detector. The wide field-of-view scan area was approximately 1.1 mm x 0.9 mm with a step size of 2.2 µm. The diffraction patterns were saved at a resolution of 320 x 240. The data analysis was carried out using the ESPRIT 2.3 software. Grain boundaries, if any, were defined by a misorientation of 10 °. Inverse pole figure along the Z-axis (out of plane), which is parallel to the epitaxial growth direction, was used to interpret the growth orientation, and thus ascertain the possibility of any polycrystalline formation.

4.2.5 FIB milling coupled with EBSD to study mergence interface

FIB sectioning, SEM imaging, energy dispersive X-ray spectroscopy (EDS), and EBSD mapping of the sectioned interface was carried out on a Zeiss Crossbeam 540 dual-beam FIB instrument. The FIB trench was milled with a beam current of 15 - 1.5 nA at 30 kV, and further polished using a smaller current of 700 pA at 30 kV to generate good surface quality for SEM imaging and EBSD. EDS mapping on the cross-sectional surface was performed using the Oxford Instrument Xmax^N 150 EDS detector at 10 kV and 1 nA, and EBSD data was acquired using the Oxford Instrument Nordlys Max detector at 20 kV, 10 nA and a step size of 400 nm. SEM images for EBSD mapping were acquired using a forescattered electron detector.

4.2.6 X-ray photoelectron spectroscopy (XPS)

XPS measurements were conducted using a PHI5000 Versa Probe III instrument (Ulvac-PHI, INC.). An Al monochromatic source was used to generate X-ray with Power of 25W, voltage of 15kV and a beam diameter of 100 micron. A pass energy of 55 eV was set for the analyser.

An electron neutralizer gun was used to prevent any surface charge build-up. Before test, the sample surface was sputter-cleaned with an Ar+ ion source of 2kV, 1.8 µA and a raster size 3x3 mm2 for 5 seconds. The obtained spectrum was calibrated to the signal of adventitious carbon at 284.8 eV and the analysis and fitting were done using CASAXPS software.

4.2.7 XRD

XRD was performed using a Cu source Rigaku diffractometer with ‘2Θ’ from 20 to 150 degrees with a step size of 0.01 degree.

4.2.8 Fourier Transformation Infrared Spectra (FTIR)

FTIR were measured with a Thermo IR spectrometer (Nicolet 6700) in a N2-filled glovebox.

4.2.9 Atomic Force Microscopy (AFM)

3D morphology was obtained by the Bruker Dimension Icon AFM. A sharp probe with tip radius of 8 nm and spring constant of 26 N m^{-2} was used for optimal lateral resolution to precisely visualize small features. The probe was calibrated on a clean sapphire sample before each AFM scan. A 20 µm × 20 µm scan area was mapped at 40 nN under the Bruker PeakForce Module for each test.

4.2.10 Online Mass Spectroscopy

A Thermo Fischer quadrupole mass spectrometer with Ar carrier gas flown at a constant rate of 0.8 µl min^{-1} was used to count the gas evolution. Online MS is used in this study to quantify the amount of 'dead Zn' formed and left in the separator due to dendrite formation during cell cycling. The separator was carefully removed from each two-electrode beaker cell after cycling. The separator was then sealed in a vial which was connected to the MS. And by injecting 10 mL of 10% H_2SO_4 into the vial to consume all the Zn metal, the resultant H_2 count can then be used to quantify the residual 'inactive Zn' following Equation 3.2.6.1.

4.2.11 X-ray Computed Tomography

XCT were mainly used in this study to check the quality and density of the Single-Zn produced by prolong electroplating on a Single-Zn substrate. The X-ray tomogram was recorded within a Zeiss Xradia 610 Versa X-ray computed tomography microscope at a 160 kV accelerating voltage and a current of 150 µA.

A total of 3201 equiangularly distributed projections were taken over 360° for the tomogram, with a pixel size of 1.76 µm. The tomogram was reconstructed using Zeiss Scout and Scan Control System Reconstructor into 16-bit TIFF images, which are parallel to the substrate Zn and the plated surface. The reconstructed volume (1.76 µm/voxel) was a cylindrical region of interest, measuring 3.504 mm high by 3.497 mm diameter, within the sample. TIFF images at the selected depths from the plated surface were shown to reveal the absence of voids away from the plated surface. The TIFF images were then converted to the raw data format, and processed using Avizo Fire (version 2020.3.1). The 16-bit Hounsfield greyscale image was filtered with non-local means filter first, and then with the plated Zn and substrate Zn segmented respectively based on the known thickness of the electroplating of 520 µm. A binary colour map was applied for the 3D volume rendering to show the interface between the plated Zn and the substrate Zn.

The TIFF images were then resliced perpendicular to the substrate Zn to show the morphology inside the plated Zn. The relative density of electroplated Zn was determined by comparing the attenuation of the plated Zn with the attenuation of 100% dense Zn [1][2]. Grey levels of the electroplated Zn at different depths were calculated as the average in sections parallel to the interface with area of 0.88 × 0.88 mm (i.e. 500 pixels). The calculated grey levels were then converted to relative density using the NIST database, which provided the attenuations of Zn and dry air at 160 keV.

4.3 Results and Discussion

4.3.1 The limitations of semi-matched substrates and heterogenous deposition interface

As previously mentioned in section 4.1, Zn electrodeposition on semi-matched substrates cannot achieve fully planar Zn deposition, with non-planar Zn formation often observed at the edge of flat Zn deposits which is aggravated after prolong cycling.

This is likely the result of the imperfect substrate-deposit interface. For semi-matched substrates, despite the similar lattice parameter can induced preferential (002) deposition by forming a semi-coherent interface, this interface still suffers from lattice mismatch, which becomes increasingly larger during Zn growth after the initial nucleation. This lattice mismatch can leads to interface stress and interface defects like dislocations or twins, making it more unstable and susceptible to non-planar deposition.

This lattice mismatch can also inhibit the merging process of individual Zn islands during electroplating and promote defect generation at inter-island interfaces. This is illustrated in Figure 4.3.2.1:

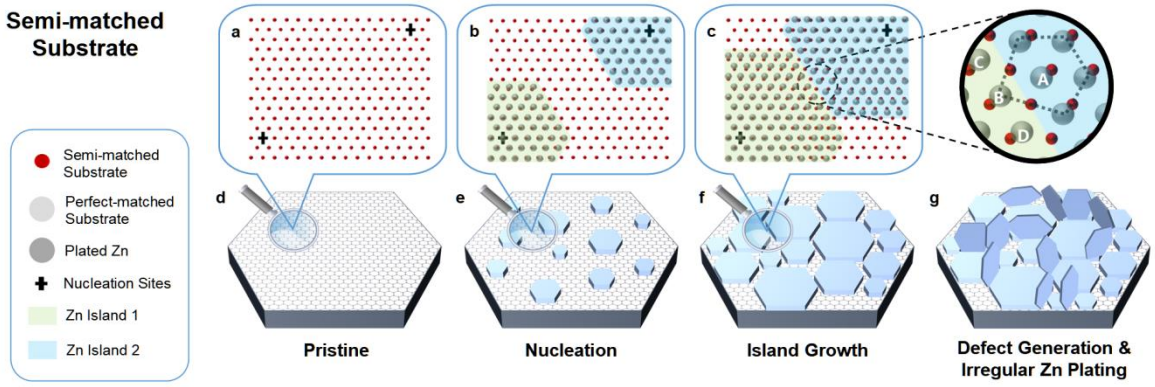


Figure 4.3.2.1 *Electroplating Zn to a semi-matched substrate, with magnified inserts (a-c) illustrating atomic arrangements and defective grain boundary formation, and (d-g) the morphological evolution*

As shown in Figure 4.3.2.1, as two Zn islands electroplated on a semi-matched grow in size, the lattice mismatch at the substrate-deposit interface gradually increases. As a result, these islands may not form a perfect hexagonal closed-pack (HCP) lattice structure upon encounter (c, insert): Atom A from island 1 will bond with atom B from island 2, but not atom C or D due to the inter-atomic distance. The lattice mismatch prevents them from forming a perfect hexagon-shaped HCP (002) basal plane at their interface. This imperfect interface, i.e. a grain boundary, will lead to defective regions forming in

between these islands, i.e. grains,[355]–[358] leaving them susceptible to other side-reactions and non-planar Zn growth, as evidenced in previous studies on semi-matched substrates[148]–[150]. Such defect and dendrite formation induced by an imperfect interface have been reported in other metallic anode battery systems[359], [360].

4.3.2 The viability of using Single-Zn to Incentivize planar (002) Zn growth

Based on the understanding on Section 4.3.1, we believe that an optimal and ideal substrate that can be used to induce (002) planar Zn deposition is the one that bears minimal lattice mismatch with Zn's (002) face and inherently possess minimal surface defects so that stress free Zn deposition with minimal defects can be maintained even after prolonged cycling.

And what substrate can better match the lattice parameters of the (002) Zn than (002) Zn itself? Based on this criteria, we have decided to study (002)-oriented single crystal Zn as a potential anode to optimize planar Zn deposition for AZBs. A (002)-oriented single crystal Zn substrate not only has the perfect lattice matching, it is also free of grain boundaries and contains minimal other defects like dislocations etc. In addition, since most proposed AZB cathode materials do not inherently possess Zn ions, Single-Zn anode can also act as a Zn ion source in AZB full cell operations while for lattice-similar anode substrates, some amount of Zn needs to be pre-plated on them before they can be used in full cells.

To verify that Single-Zn can be used as a substrate to induce planar Zn deposition, electroplating was performed on the (002) surface of polished single-crystal Zn ('Single-Zn') whose resultant surface was then compared with Zn deposition using other substrate materials like 316-stainless steel, copper, platinum, poly-crystalline Zn ('Poly-Zn'). All the plating was performed under a relatively moderate

condition with 0.5 mAh cm^{-2} capacity and 2 mA cm^{-2} current density. The results are shown in Figure 4.3.2.1:

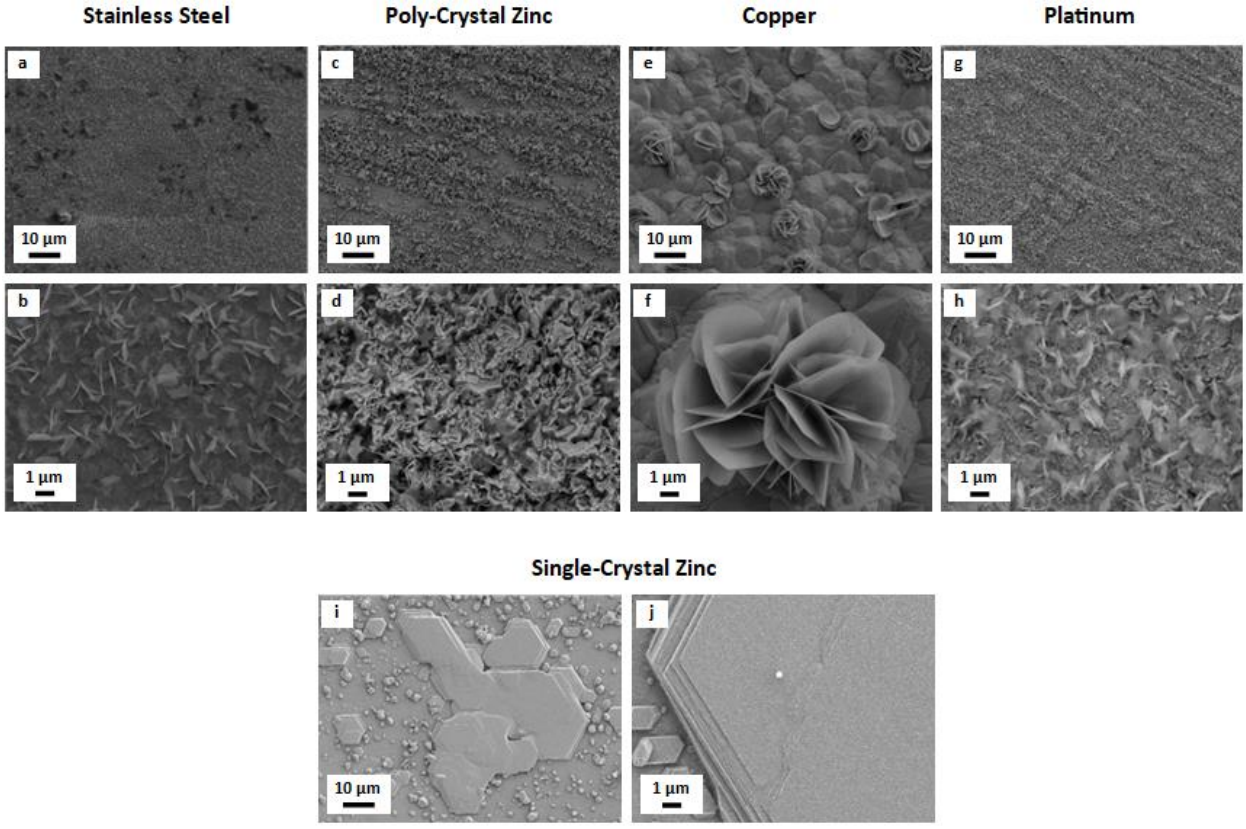


Figure 4.3.2.1. Morphology of electroplated zinc on different anode substrates. *Low and high magnification SEM images of Zn electroplated on (a,b) stainless steel, (c,d) Poly-Zn, (e,f) Copper (g,h) Platinum (I,j) Single-Zn at 0.5 mAh cm^{-2} at 2 mA cm^{-2}*

SEM imaging in Figure 4.3.2.1 revealed the Zn deposited on stainless steel, copper, platinum, and Poly-Zn all exhibited a randomly orientated, flaky morphology that frequently extended outward from the electrode surface (a-h). The flower-like Zn deposition on copper foil (Figure 4.3.2.1 e&f) was particularly interesting and is believed to be due to Zn platelets preferentially depositing at the grain boundaries, especially at the triple points of the copper foil. In comparison, Zn plated on the Single-Zn electrodes

produced flat and smooth hexagonal islands that all exhibited the same rotational alignment (i,j) This post-plating surface morphology difference among three substrates: Stainless steel, Poly-Zn and Single-Zn is further examined using AFM, as shown in Figure 4.3.2.2:

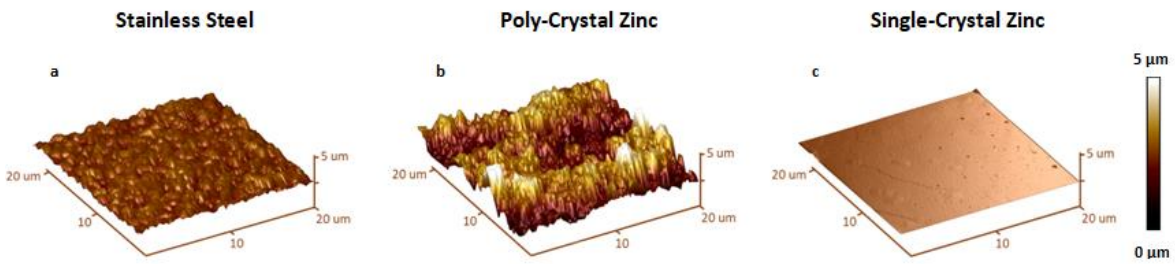


Figure 4.3.2.2 *AFM surface profiles of zinc plated on (a) stainless steel, (b) Poly-Zn, and (c) Single-Zn at 0.5 mAh cm^{-2} at 2 mA cm^{-2}*

Figure 4.3.2.2 the irregular non-planar Zn deposition on Stainless Steel and Poly-Zn had led to severe roughening of the electrode, as shown by atomic force microscopy (AFM) imaging (a,b). These highly uneven deposition morphologies will facilitate dendrite growth upon further plating or cycling.[48], [95], [114], In comparison, Post-plating Single zinc anode remained flat and planar and showed no sign of dendrite initiation.

4.3.3 Electrodeposition quality of planar Zn on Single-Zn anode

To check the Zn plating quality on Single-Zn anode, the electrodeposition interface was examined using SEM coupled with FIB cross-sectioning and EDS mapping, as shown in Figure 4.4.3.1:

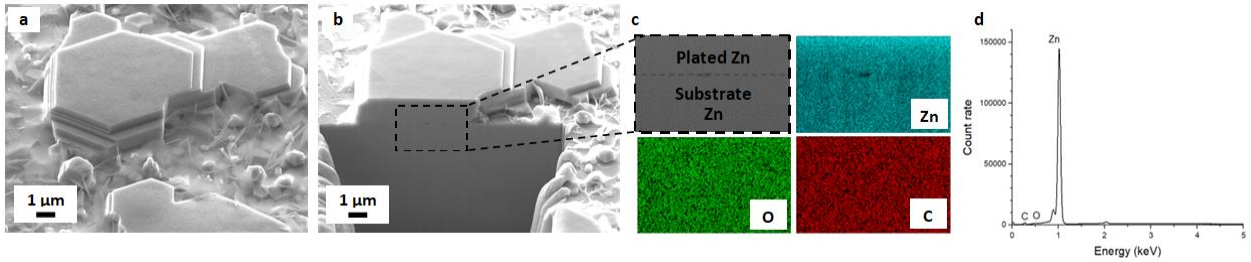


Figure 4.3.3.1 *Cross-sectional SEM imaging and EDS mapping of the interface between electroplated Zn and the Single-Zn substrate. (a) before FIB milling (b) after FIB milling (c) EDS elemental mapping of the Zn, O and C (d) EDS spectrum showing the total count of different elements: C Kα = 2.0 × 10^5; O Kα = 2.2 × 10^5; Zn Lα = 2.3 × 10^6.*

Figure 4.3.3.1 revealed no distinguishable defects or any C or O segregation (common inclusion containing elements) between the electroplated Zn and the substrate Zn. These interfacial qualities, along with the rotational alignment of the hexagons shown in Section 4.3.2, strongly suggest that the Zn islands formed coherent, epitaxial metallic bonds with the Single-Zn substrate.

4.3.4 Achieving planar Zn deposition under high rate and capacity conditions

After verifying that planar (002) deposition can indeed be achieved using a Single-Zn anode, the next step is to ascertain its performance consistency and limits under higher capacities and current densities, conditions under which Zn anodes are known to be more susceptible to dendrite formation.[47], [114]

We first increased the plating current density from 2 mA cm^{-2} to 10 mA cm^{-2} and the plating capacity from 1 mAh cm^{-2} to 8 mAh cm^{-2}, the SEM imaging and the EBSD results are shown in Figurer 4.3.4.1:

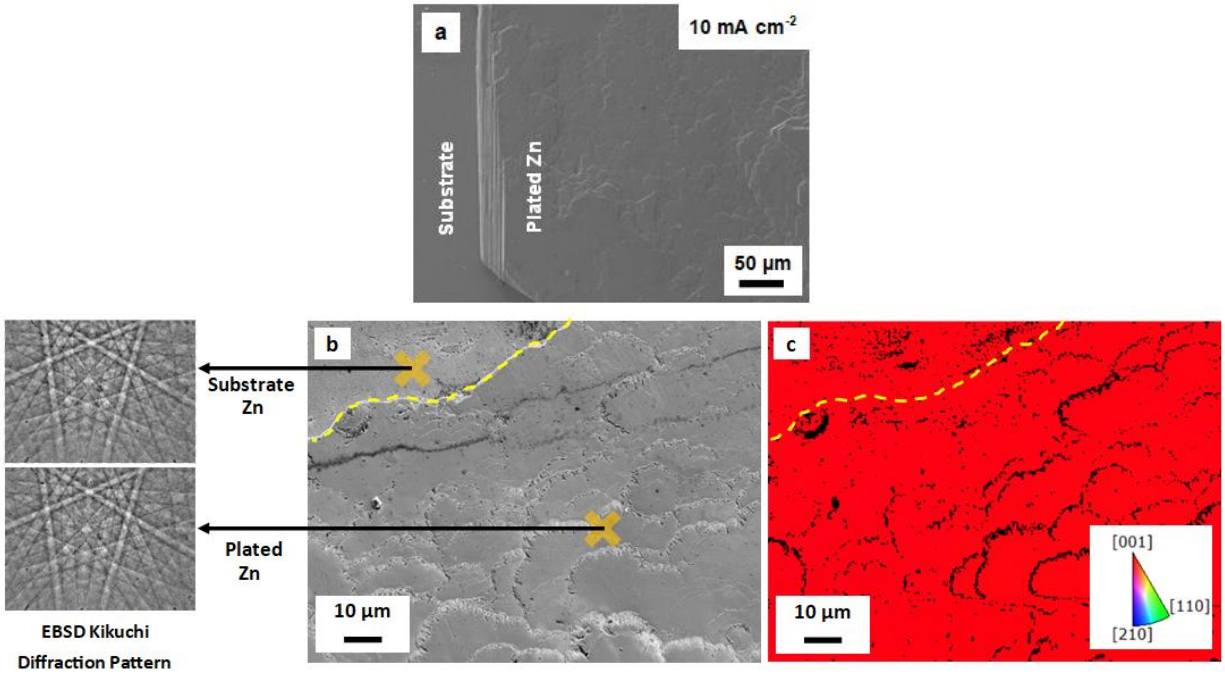


Figure 4.3.4.1 *SEM imaging and EBSD mapping on substrate Zn and plated Zn following electroplating for 8 mAh cm^{-2} at 10 mA cm^{-2}.*

The SEM imaging (a) shows that the layered planar Zn deposition was perfectly maintained after we increased the plating rate and capacity. And to confirm the plated crystal orientation, we employed extended field-of-view electron backscatter diffraction (EBSD). EBSD mapping requires a flat specimen, typically polished smooth, and thus is not usually suitable for characterization of electrodes post-plating. However, as our Single-Zn electrodes were uniformly plated with smooth planar Zn, we were able to perform EBSD, which shows that the plated Zn only exhibited one crystal orientation, which matches that of the underlying Single-Zn substrate, confirming the consistent (002) planar deposition induced by the single-Zn crystal.

4.3.5 Testing the limit of planar Zn deposition under ultra-high-rate conditions

While keeping the plating capacity at 8 mAh cm^{-2}, we further increased the plating rate to test its high-rate limits all the way until an ultra-high rate of 200 mA cm^{-2} was applied, as shown in Figure 4.3.5.1:

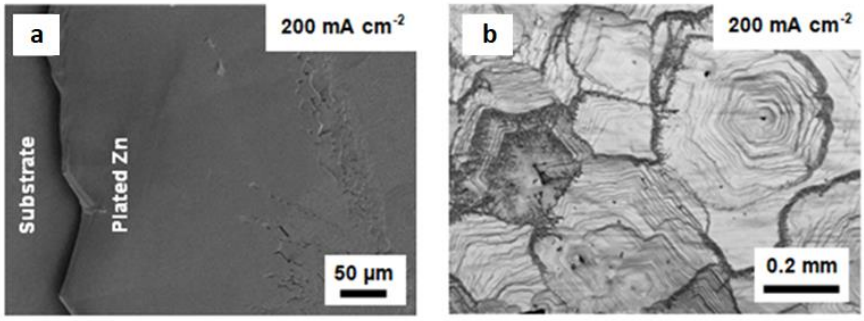


Figure 4.3.5.1. *SEM and optical imaging of electroplated Zn on Single-Zn for 8 mAh cm^{-2} at 10 mA cm^{-2}.*

Figure 4.3.5.1 shows that the electroplated Zn remained planar with no dendrite growth even under an ultra-high electroplating current density of 200 mA cm^{-2}, a record that has not been reported in AZBs or any other battery systems without employing porous 3D anodes.[142], [143] (3D electrodes substantially reduce the effective current density by increasing the effective surface area). This quality of such plating was further examined using XRD and extended field-of-view EBSD mapping, as shown in Figure 4.3.6.2:

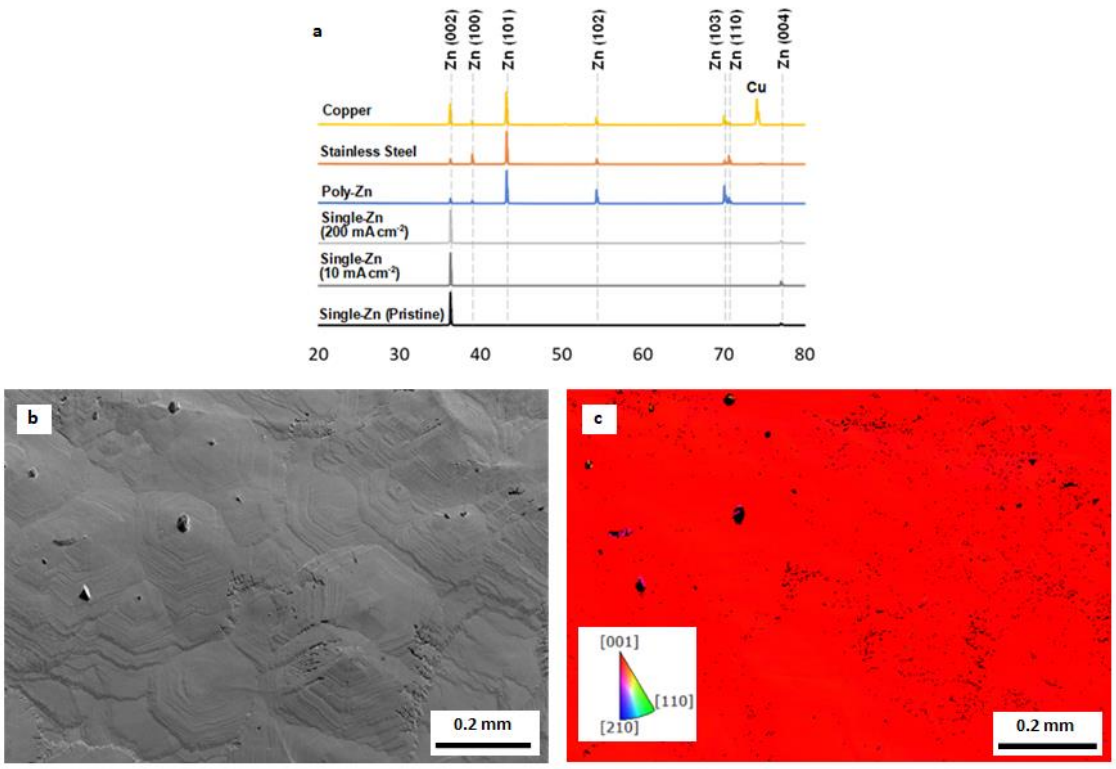


Figure 4.3.5.2 *(a) XRD of the electroplated Zn on various electrode substrates. (b-c) Low magnification EBSD orientation map of Single-Zn electrode after 200 mA cm^{-2} Zn plating with a capacity of 8 mAh cm^{-2}*

Figure 4.3.5.2 shows that the XRD pattern remained unchanged after plating at even 200 mA cm^{-2} (a), proving that minimal non-planar Zn formed during the electrodeposition. In comparison, electroplating on stainless steel, copper and Poly-Zn all resulted in significant Zn growth along other crystal orientations, including (100), (101) and (110), which are known to be more susceptible to dendrite formation and corrosion.[126] Extended field-of-view EBSD mapping (b-c) further confirmed that electroplating on Single-Zn was consistently planar across the entire electrode, exhibiting a single crystal orientation of (002).

4.3.6 Zn islands mergence via perfect lattice stitching

It has been shown that under low-capacity conditions, the electroplated Zn could not cover the entire Single-Zn substrate surface and they are deposited as individual islands (Figure 4.3.3.1). To better understand the plating morphology evolution as we increase the deposition capacity, a series of plating were performed under the same rate but with different plating time i.e. to different capacity, as shown in Figure 4.3.6.1:

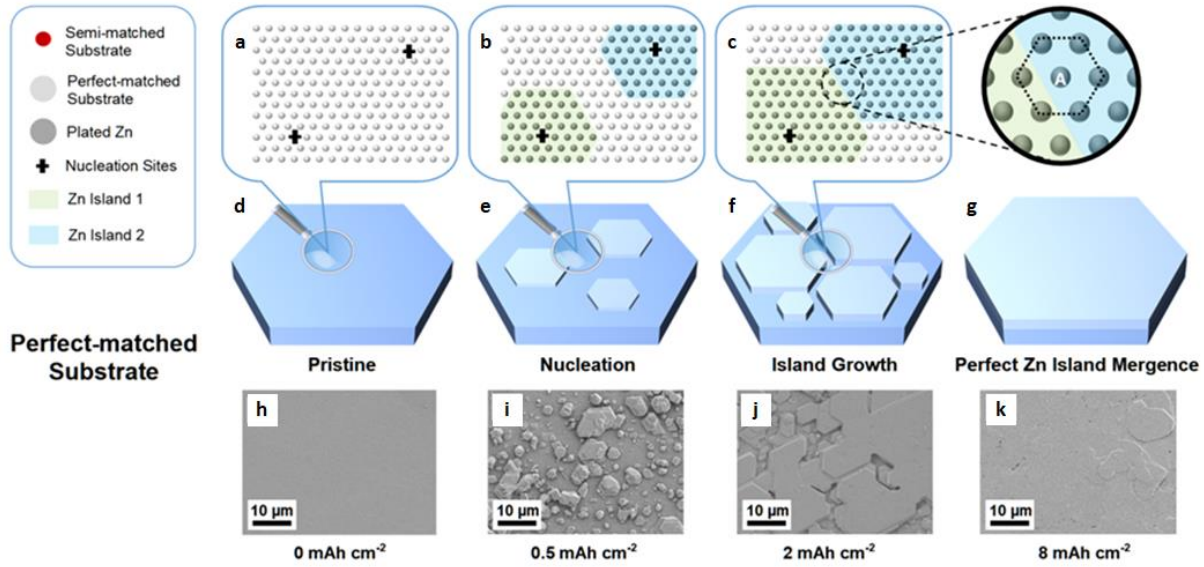


Figure 4.3.6.1 *Electroplating to a perfect-matched substrate, with magnified inserts (a-c) illustrating atomic arrangements and inter-island stitching, and (d-g) the morphological evolution. (h-k) SEM of electroplated Zn on a Single-Zn anode at increasing capacities at 2 mA cm^{-2} plating rate*

Figure 4.3.6.1 shows that, after the initial nucleation (b,e,i), these discrete hexagonal Zn islands uniformly thicken and expand (c,f,j), and eventually merge together into a single grain upon extended electroplating (g,k), maintaining a relatively planar and uniform surface after electroplating.

However, different to the plating at lower rates, the Zn deposition morphology at higher rates seems to be in the form of multiple individual hexagonal pyramidal islands, as shown in Section 5.3.5. To examine the crystallographic relation between different islands, FIB coupled with cross-section imaging and EBSD was performance on the interface of three different islands, as shown in Figure 4.3.6.2:

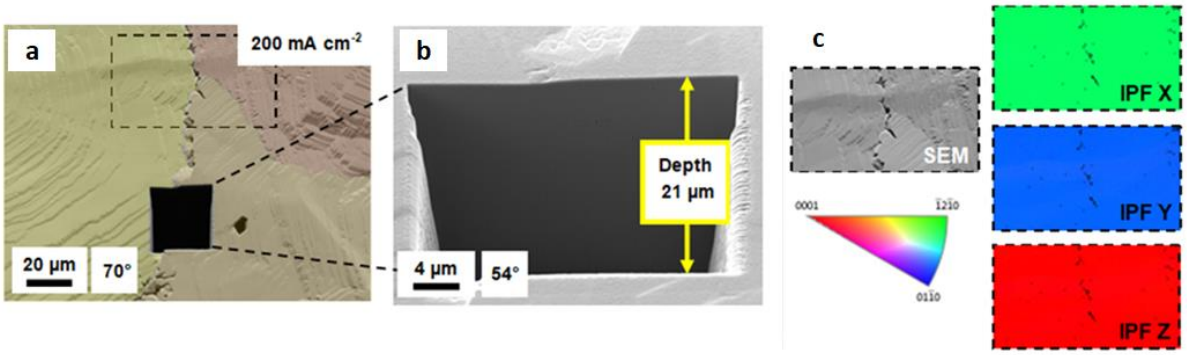


Figure 4.3.6.3 *(a) SEM image of three merged electroplated Zn islands on Single-Zn. (b) SEM image of a FIB cross-section through the interface between two merged Zn islands (the dark square in a). (c) EBSD orientation maps acquired from across the intersection of three islands (the dashed region in a). All plating experiments were performed at a rate of 200 mA cm^{-2} and to a capacity of 8 mAh cm^{-2}*

Figure 4.3.6.3 a shows the triple point of three individual pyramid islands formed due to ultra-high-rate Zn plating on Single-Zn, as outlined using different colors. The interface between two of the islands has been examined by imaging its cross-section using FIB-milling (b), which showed no significant cracking or void formation between the islands upon mergence. This 21 µm deep cross-section also revealed the exceptional plating quality of the Zn metal at this high current density, with no internal occlusions or defects. Figure 4.3.6.3 c shows the EBSD mapping of the crystal orientation at the triple point between three merged Zn islands as marked out by the black square in Figure 4.3.6.3 a. The uniformly colored mapping along all three directions have confirmed that no out-of-plane Zn crystal orientation formed at the interface upon mergence and no twinning was generated to accommodate any lattice mismatch.

This shows that, despite multiple individual hexagonal pyramidal Zn islands were formed due to the ultra-fast plating kinetics at high-rate conditions, these islands can still merge together into a single crystal.

These results show that, using single-Zn anode planar, Zn deposition can be achieved with minimal defect and excellent high-rate performance well beyond that achievable by other substrates. This is due to two key advantages: (i) With a single-crystal Zn anode, a stress-free interface with minimal defect can be well-maintained along the entire (002) crystal plane throughout plating. The stress-free, homoepitaxial Zn-on-Zn plating offers the lowest energy barrier and thus is optimal for promoting epitaxial lateral planar Zn growth. This is evidenced by the low nucleation overpotential for plating on Single-Zn, as well as the mass transport limit not being reached even at plating currents up to 250 mA cm^{-2}, as shown in Figure 4.3.6.3. (ii) The uniform orientation of the substrate, due to being a single crystal, and its perfect lattice matching with the Zn deposit, allow individual plated islands to merge together into a larger single grain, maintaining perfect inter-grain atomic stitching upon mergence without forming grain boundaries or other inter-island defects.

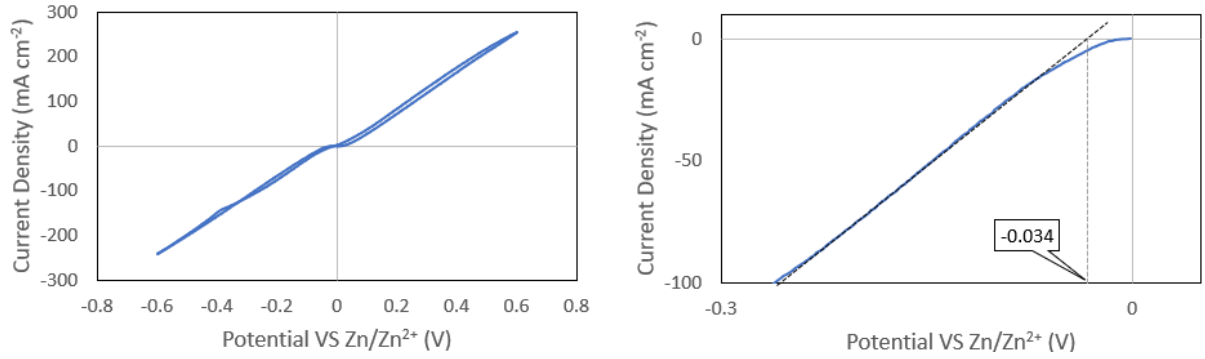


Figure 4.3.6.3 *Cyclic voltammetry of a three-electrode cell (Single-Zn working electrode, Poly-Zn counter and reference electrodes) from -0.6 to +0.6 V vs. Zn/Zn^{2+} at a scan rate of 20 mV s^{-1} alongside a magnified view near the origin, showing the overpotential for nucleation on Single-Zn.*

4.3.7 Single-Zn anode's cycling performance

To confirm that this perfect epitaxial deposition is not only well maintained after a single electroplating but also over prolonged cycling, we conducted further electrochemical evaluation of the Single-Zn anode's cycling performance.

The Single-Zn was first cycled in a symmetric cell for 100 cycles at a current density of 10 mA cm^{-2} with 1 mAh cm^{-2} capacity, a test condition commonly used in AZB studies [114], [135], [302]. For comparison, a Poly-Zn/stainless steel cell and a Poly-Zn symmetric cell were cycled under the same conditions, the cycling data and the post-cycling separators are shown in Figure 4.3.7.1:

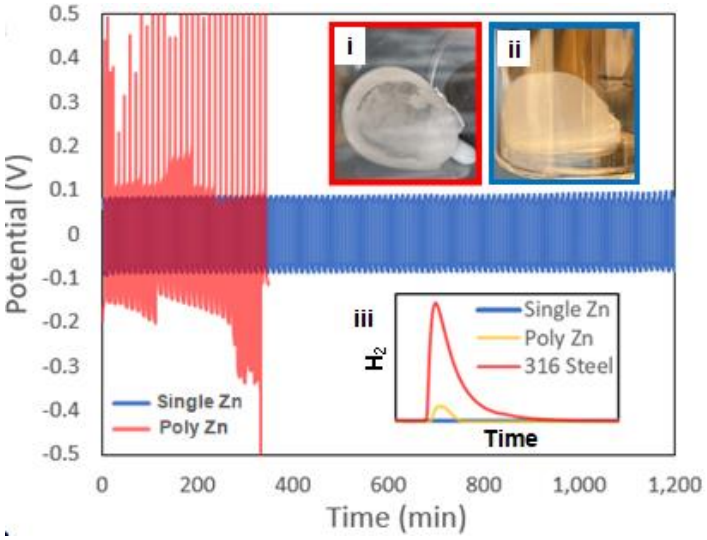


Figure 4.3.7.1 *Galvanostatic cycling of a Poly-Zn/stainless steel cell (red) and a Single-Zn symmetric cell (blue) at 10 mA* cm^{-2}*. Insets: (i) The Poly-Zn/stainless steel cell separator, with significant 'dead Zn' accumulation (dark areas). (ii) The Single-Zn symmetric cell separator. (iii) Online mass spectrometry of hydrogen evolution from the cycled separators following titration with* H_2SO_4 *solution*

It can be seen from Figure 4.3.7.1 that the Single-Zn cell's cycling overpotential showed no significant change over the 100 cycles (blue). However, the Poly-Zn/stainless steel cell developed a significant plating overpotential after only 30 cycles (red).

In addition, a significant amount of electrically isolated 'dead Zn'[48] were found in the separator after disassembling the Poly-Zn/Stainless steel cell (inset i), indicating Zn dendrite formation and detachment during cycling. In comparison, no sign of 'dead Zn' was found on the separator of the Single-Zn symmetric cell after cycling (inset ii). By titrating the separators with H_2SO_4 solution and detecting H_2 evolution via on-line mass spectrometry, [172], [336] we could quantify the residual 'dead Zn' in the Poly-Zn/stainless steel cell and the Poly-Zn symmetric cell to be 0.73 mAh cm^{-2} and 0.032 mAh cm^{-2}, while no hydrogen evolution signal indicative of 'dead Zn' was picked up from the Single-Zn symmetric cell (inset iii).

The post-cycling surfaces of Single-Zn and Poly-Zn anodes were also examined using SEM and XRD as shown in Figure 4.3.7.2:

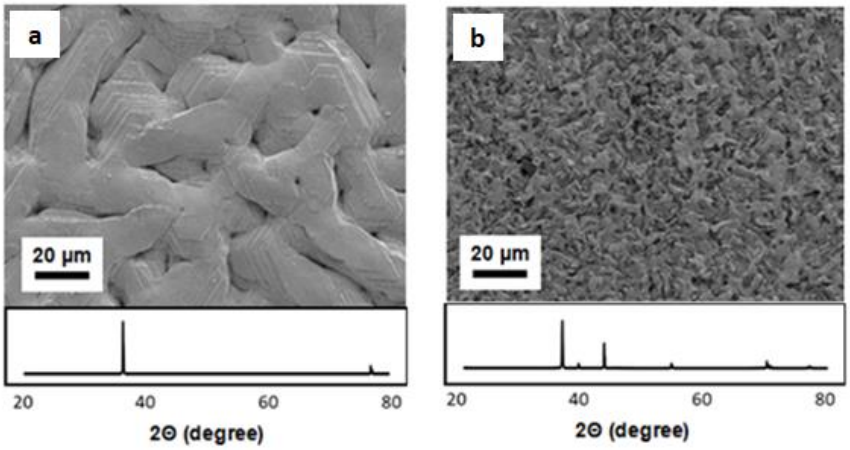


Figure 4.3.7.2 *SEM images and accompanying XRD spectra of (a) the Single-Zn anode and (b) the Poly-Zn anode after 100 cycles at 10 mA cm^{-2}, 1 mAh cm^{-2} per cycle*

Figure 4.3.7.2 shows that Single-Zn anode perfectly maintained its planar (002) crystal orientation after 100 cycles despite some localized grooving observed on the metal surface and showed no sign of dendrite formation (a). While in comparison, post-cycling Poly-Zn anode showed a much rougher surface morphology (b). The Single-Zn's unchanged post-cycling crystal orientation is further confirmed using EBSD as shown in Figure 4.3.7.3:

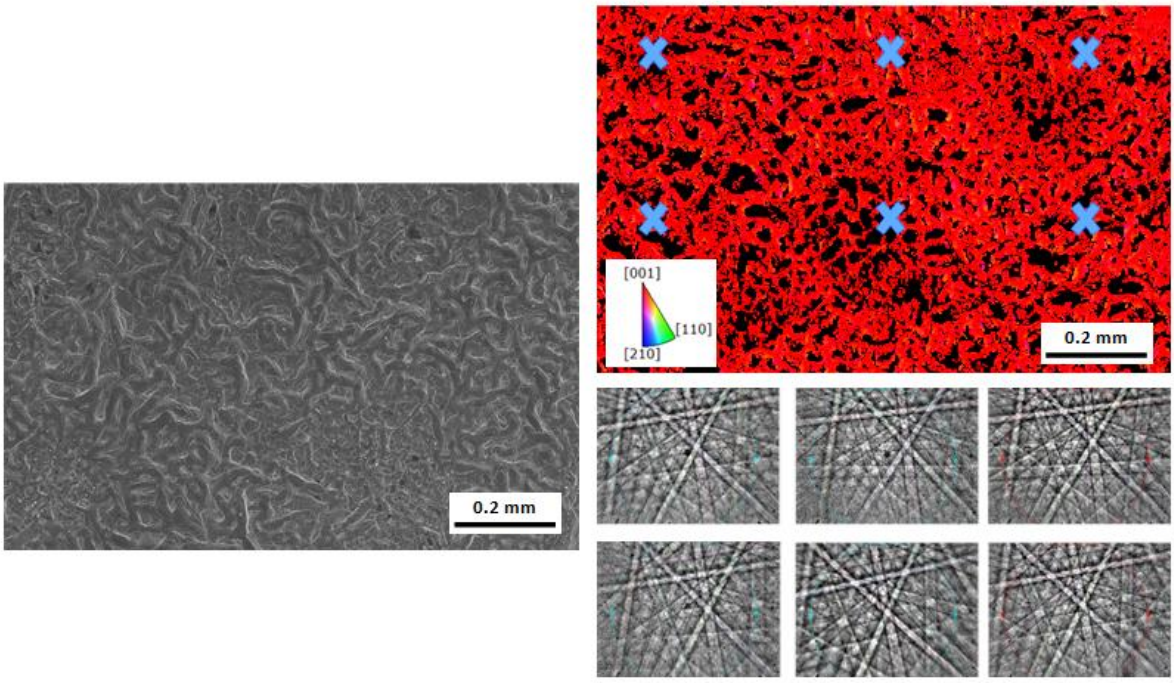


Figure 4.3.7.3 *Post-cycling EBSD mapping. SEM image, EBSD map, and local Kikuchi diffraction patterns taken from the points indicated by the blue crosses on the map after 100 cycles at 10 mA* cm^{-2}.

The uniform red-colored mapping and the consistent Kikuchi patterns obtained from different locations shown in Figure 4.3.7.3 indicates that the Single-Zn anode largely maintained its planar (002) orientation post-cycling.

We then further tested the Single-Zn anode's performance under a higher rate (50 mA cm^{-2}) and higher capacity (4 mAh cm^{-2} per cycle) condition which ran for 1,200 cycles. The results are shown in Figure 4.3.7.4:

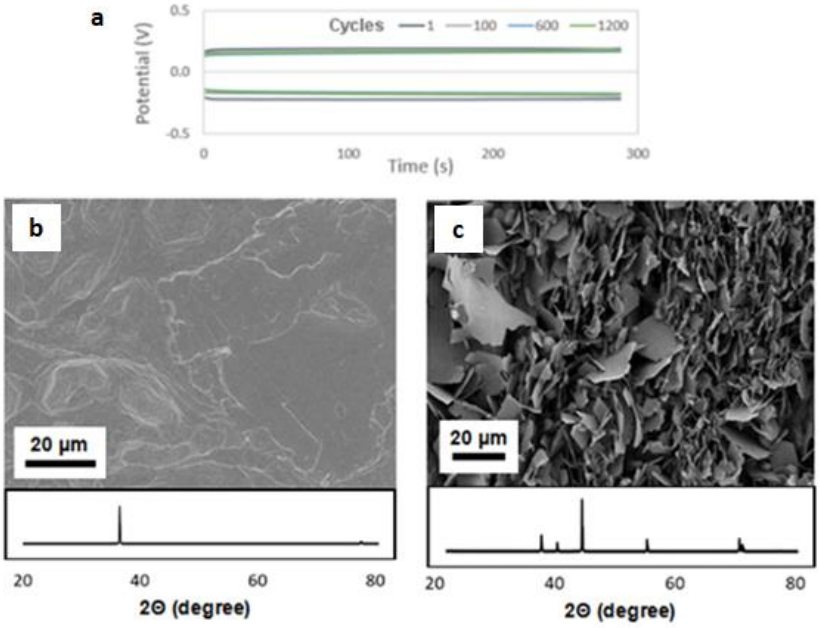


Figure 4.3.7.4 *(a) Cycling plots of plating and stripping overpotentials from a symmetric Single-Zn cell cycled for 1,200 cycles at 50 mA cm^{-2} with 4 mAh cm^{-2} per-cycle capacity. SEM images and accompanying XRD spectra of (b) the Single-Zn anode after 1,200 cycles at 50 mA cm^{-2}, 4 mAh cm^{-2} per cycle and (c) the Poly-Zn anode after 200 cycles at 50 mA cm^{-2}, 1 mAh cm^{-2} per cycle*

Figure 4.3.7.4 shows that no significant plating/stripping overpotential was observed after 1200 cycles at such a higher rate and capacity condition (a) and the planar anode surface could also be well maintained (b). In comparison, when cycled under the same rate and at a lower capacity of 1 mAh cm^{-2} per cycle, a Poly-Zn anode exhibited a highly flaky morphology after cycling (c), which will likely lead to more dendrite formation and detachment and thus more anode capacity loss and lower efficiency.

4.3.8 Single-Zn anode's post-plating aging performance

We have also tested Single-Zn's performance to resist aging degradations - reactions – corrosion and hydrogen generation reactions – commonly seen in AZBs during aging[361],[39]. For comparison, A stainless steel and a Single-Zn anode were both electroplated with Zn from 2M $ZnSO_4$ to a capacity of 8 mAh cm^{-2} and left to age in the same electrolyte under ambient conditions, as shown in Figure 4.3.8.1:

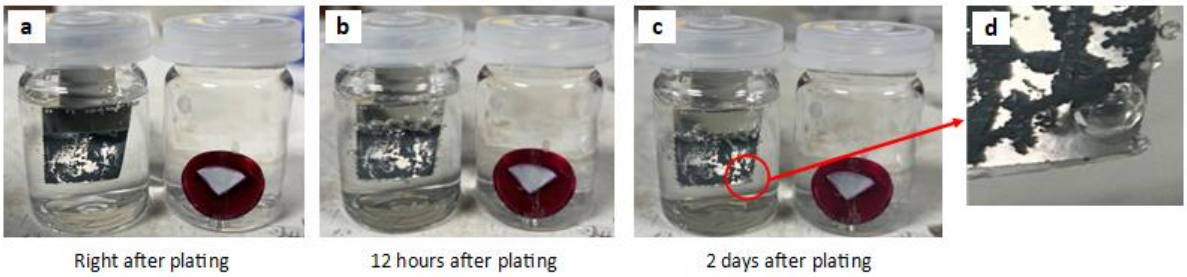


Figure 4.3.8.1. *Comparison of the plated Zn on stainless-steel and on Single-Zn anodes. 8mAh cm^{-2} Zn was electrochemically plated onto SS (left vial) and Single-Zn (right vial) and left to age at ambient conditions in 2M $ZnSO_4$ for (a) 0 min; (b) 12 hours; (c) 2 days. (d) is the magnified image from (c).*

Figure 4.3.8.1 shows that the Single-Zn anode suppresses unwanted side (left vial: stainless steel, right vial: Single-Zn). Bubble formation and discoloration can be readily observed from the stainless steel anode even right after plating, which are indicative of metal corrosion and hydrogen generation. This worsened over time, with extensive bubble formation seen around the whole stainless steel anode after 12 hours of aging. After two days of aging, evidence of plated Zn delaminating from the steel anode due to the aggressive hydrogen gas generation was observed (d). Such Zn detachment into inactive 'dead Zn' would reduce cell capacity. In comparison, Zn plated onto the Single-Zn anode showed minimal discoloration throughout the aging process, and experienced much less bubble formation. We attribute the Single-Zn anode's robustness to aging to its flat electroplating morphology, minimizing the exposed surface area for side reactions to occur upon, and the elimination of the formation of other crystal

orientations like (100), (101) and (110), which have been reported to be more susceptible to corrosion.[126] Whereas Zn plated on stainless steel presents a significantly rougher structure with various crystal orientations exposed to the electrolyte, making it more vulnerable to corrosion attack. However, Single-Zn was not completely immune to aging side reactions, with some discoloration observed, and XPS (surface sensitive) revealing additional chemical species indicative of some oxide and hydroxide formation on the metal surface as shown in Figure 4.3.8.2. Additional corrosion mitigation strategies like protective layer [106], [108], [135], [141], electrolyte modification [97], [105], [338] etc. can also be employed to further optimize this system.

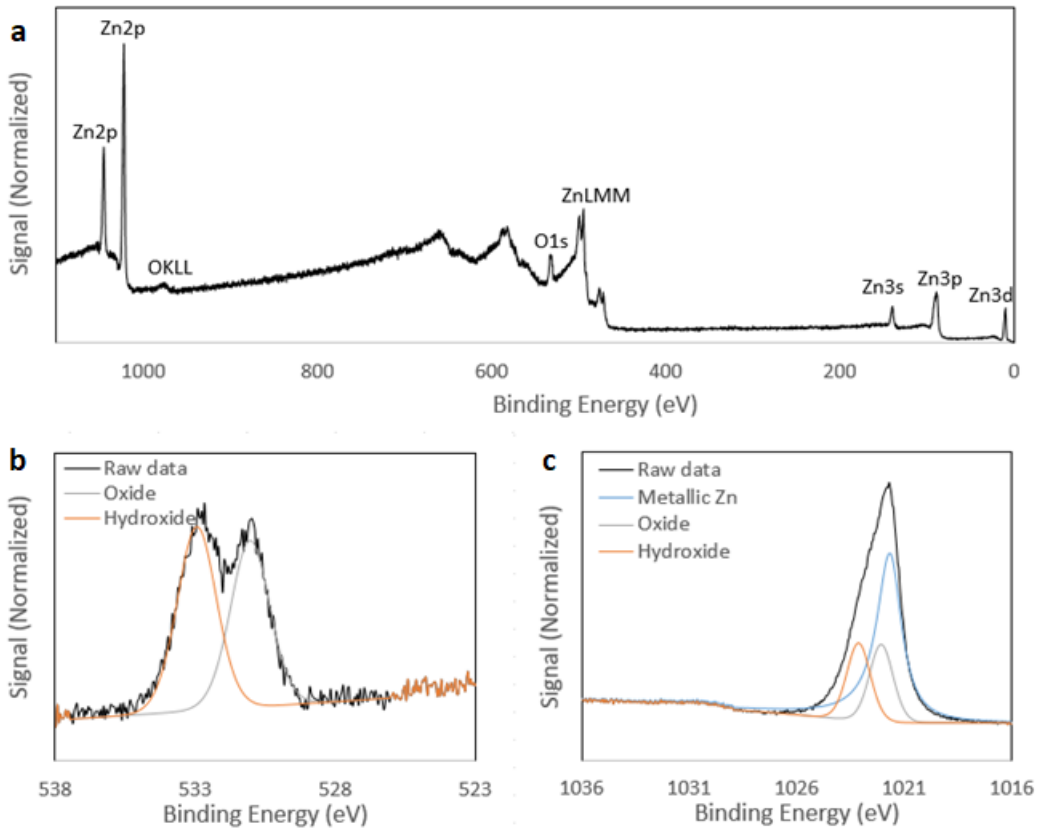


Figure 4.3.8.2. *XPS spectrum showing the surface chemistry of the plated Zn on Single zinc after 2 days of aging, indicating hydroxide and oxide formation due to corrosion reactions. (a) Full-range spectrum (b) O1s signal and related chemical species' peak fitting (c) Zn2p signal and related chemical species' peak fitting*

4.3.9 Possible scalable Single-Zn production by electroplating

The current method used for Single-Zn production, the Czochralski approach [362], is rather complex and expensive. (A thumb-nail sized specimen of 1.5 grams costed several hundred pounds) Inspired by the planar deposition results shown previous, we believe that our high-rate epitaxial electrodeposition system could also be used as a scalable method to grow Zn single crystals with significantly reduced production cost. The existing Roast-Leach Electrowin (RLE) for commercial Zn metal production produces polycrystalline Zn metal via the electrolysis of purified $ZnSO_4$ solution, itself made from roasting and leaching ZnS-containing ore. This can be readily modified for single-Zn production with little additional cost, as shown in Figure 4.3.9.1:

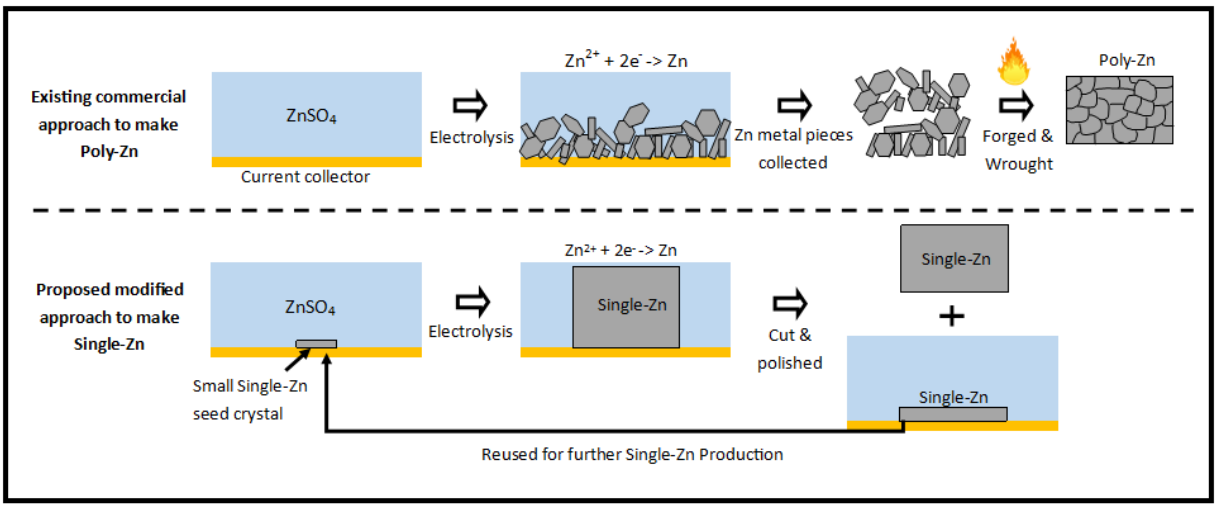


Figure 4.3.9.1 *Existing commercial approach by the Roast-Leach Electrowin (RLE) process to make Zn metal on a large scale (top process) and how it can potentially be modified to adapt for Single-Zn production.*

As demonstrated in Figure 4.3.9.1, RLE can be modified that, rather than directly plating on current collectors, we can use a Single-Zn crystal as a seed from which a larger Single-Zn crystal can be grown and harvested by Zn epitaxial electroplating. To test its feasibility, we decided to do a small

demonstration on a smaller scale: a significant amount of Zn (0.52 mm thickness, equivalent to 304 mAh cm^{-2} capacity) was electroplated onto the Single-Zn substrate at a rate of 30 mA cm^{-2} from $ZnSO_4$ solution. The post-plating sample surface is shown in Figure 4.3.9.1:

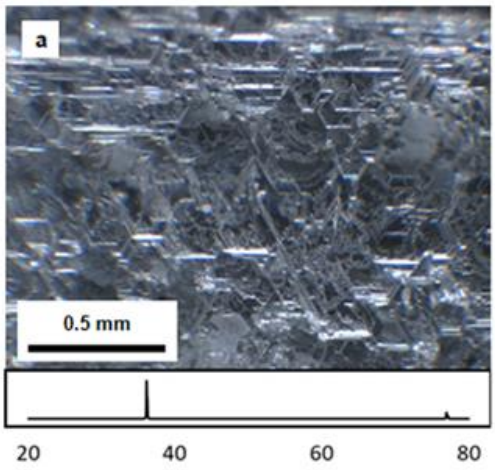


Figure 4.3.9.1 *Optical microscopy image and XRD of the Single-Zn surface following Zn electroplating to 0.52 mm depth on Single-Zn at* a rate of 30 mA cm^{-2}

Figure 4.3.9.1 shows clearly resolved planar Zn crystal with well-defined hexagonal shapes on the top surface of the electroplated Zn. This indicates that the (002) crystal orientation was well maintained after plating and the metallic Zn was plated epitaxially. This is further confirmed with XRD (inset), which shows no new peak had emerged after plating. This is further confirmed with with extended-field-of-view EBSD, as shown in Figure 4.3.9.2:

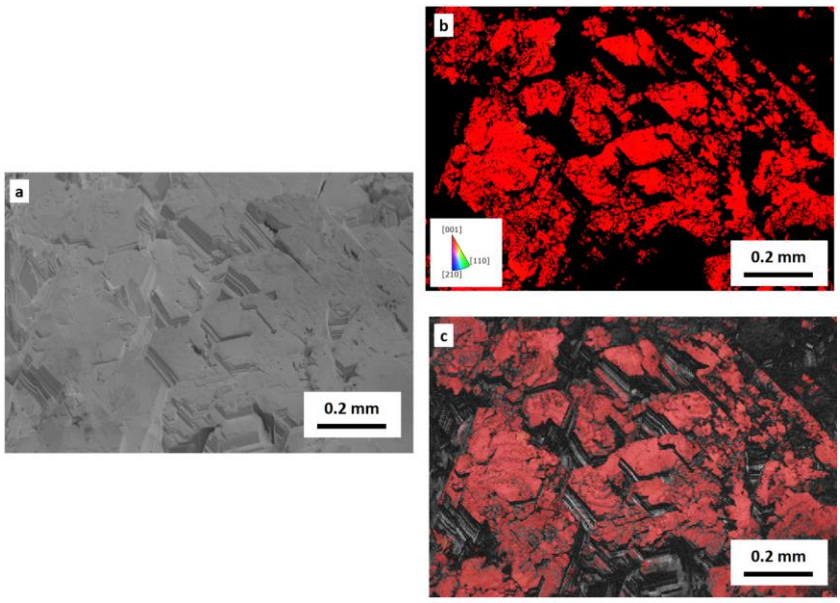


Figure 4.3.9.2. *SEM and EBSD mapping of high-depth 0.52 mm electroplated Zn on single crystal Zn electrode. (a) SEM image. (b) IPFZ map. (c) Pattern quality map.*

The uniformly colored mapping in Figure 4.3.9.2 indicates that the plated metal Zn only possesses a single crystal orientation, consistent with the XRD results.

To check the internal quality of the thick electroplated Zn layer, we used attenuation contrast X-ray computed tomography (XCT), as shown in Figure 4.3.9.3:

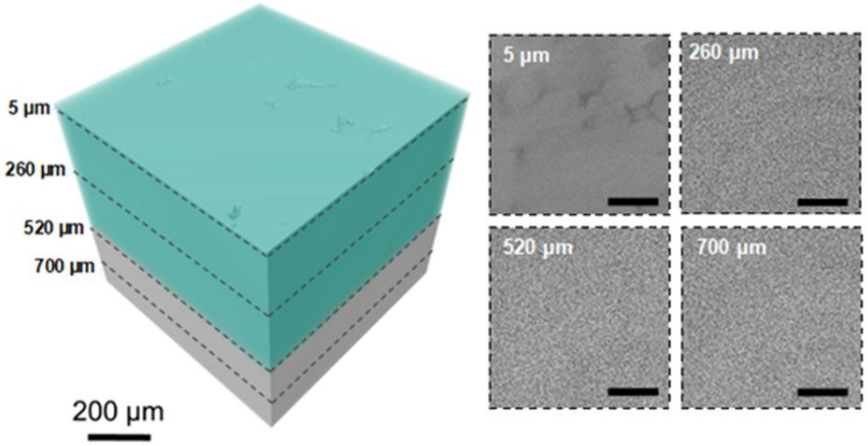


Figure 4.3.9.3 *Volume-rendered XCT image of the plated Zn and Single-Zn substrate, with parallel 2D slices extracted at different depths from the surface (5, 260, 520 and 700 µm). The lower grey region indicates the substrate, the upper turquoise area the plated Zn. Scale bars are 200 µm.*

Figure 4.3.9.3 shows the 3D rendered XCT image and the accompanying 2D image slices taken parallel to 5, 260, 520, and 700 µm beneath the interface reveal the morphology inside of the sample bulk. The lack of internal feathers from the 3D volume rendering and the 2D slicing demonstrated that the bulk Zn deposition was free of large defects and showed no significant difference to the substrate Zn itself, apart from the sporadic grooves in close proximity to the plated Zn surface, which are likely the residual unclosed gaps between individual plated Zn islands.

To further check the plating quality, the sample's virtual cross-sectional image and an average greyscale profile of the sample are shown in Figure 4.3.9.4:

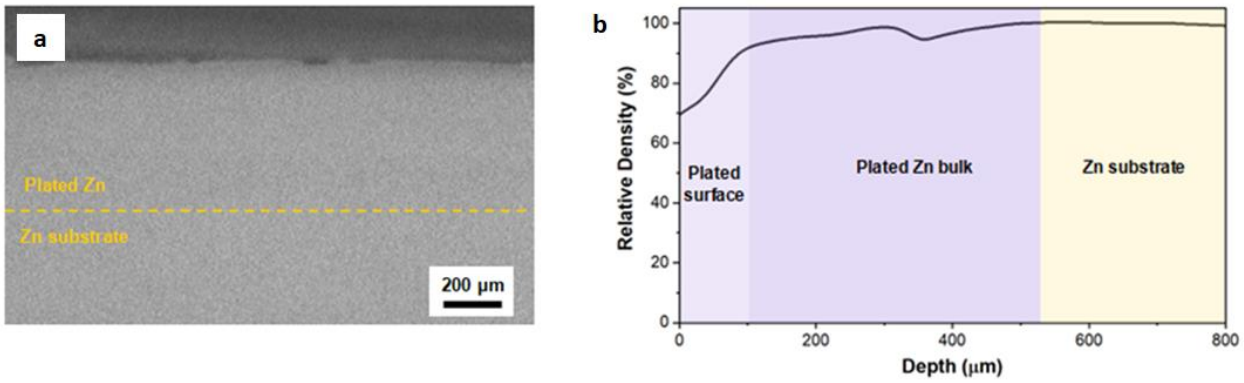


Figure 4.3.9.4 *(a) Virtual cross-sectional image slice of the plated Zn interface with the Single-Zn substrate. (b) Calculated relative density profile over the volume in Figure 4.3.9.3.*

The virtual cross-sectional image slices resolved no interfacial defects or inhomogeneities between the substrate Zn and plated Zn (a), suggesting the excellent epitaxial nature of the electroplating with defect-free metallic bonding. The average greyscale profile of the volume rendered $0.88 \times 0.88\ mm^2$ region from the plated surface to inside the substrate is indicative of the relative density of plated Zn (b). It can be seen that, apart from the region close to the plated surface (less than 100 µm), where Zn island mergence may be incomplete, the bulk of the plated Zn shares comparable greyscale intensities with the 100 % dense substrate Zn, suggesting the electroplated Zn has perfect crystallinity with minimal voids formation. A small dip in attenuation, however, can be observed around 360 µm beneath the surface. We attribute this localized dip in density to relatively more inhomogeneous nucleation occurring at the start of plating, when the over-potential will be highest. [354], [363] Overall, these results confirmed that single crystal Zn can be densely produced with no significant interior defects by epitaxial electrodeposition. The resultant single crystal Zn is of high quality, comparable to commercial crystals produced via the Czochralski method,[362] which confirmed this method can potentially be further developed for making good quality single crystals at a much lower cost, similar level to the production

cost of the polycrystalline Zn, i.e. several GBP per kilogram. However, this method's production speed and crystal quality consistency still need to be tested at larger scale.

4.3.10 Planar & dendrite-free Zn anode project summery

We have shown that, by employing single-crystal (002) Zn as an ideal model anode, without any additional architecture, electrolyte, or interface modification,[30], [99], [324] the dendrite problem can be resolved and excellent cell performance can be achieved in AZBs, thanks to defect-suppression: the lack of grain boundaries in the single-crystal, the perfect homoepitaxial lattice matching with plated Zn, and the sole expression of only the (002) face, effectively excludes the formation of the defective regions that act as the nucleation sites for irregular Zn deposition. This allows excellent planar and dendrite-free Zn electrodeposition to be achieved at an unprecedented high rate of 200 mA cm^{-2}. And this dendrite-free epitaxial surface is well maintained after prolonged cycling (>1,200 cycles) at 50 mA cm^{-2} with a per-cycle capacity of 4 mAh cm^{-2}. This presents a new strategy to preventing dendrites in aqueous zinc batteries and potentially in other battery systems as well.[11], [29], [172], [364], [365] We also demonstrated that epitaxial electrodeposition can be used as a simple and scalable method to grow high quality Zn single crystals, which substantially lowers its cost. Our findings present a reliable strategy for solving one of the fundamental challenges in AZBs – dendrite growth at the metal anode – and if partnered with a suitably robust cathode[36], [54], [77], [103], [366] would yield a compelling high-rate, safe, and economic grid-level storage capability. However, a key problem with using single-Zn anode is its current high cost. Therefore, for the next step, we should be looking at ways to reduce its cost and looking at cheaper alternative materials and approaches to achieve such textured planar deposition.

5 Systematic study of Ca electroplating behaviors

5.1 A Brief Background on the Ca ion batteries

Apart from zinc ion batteries, other multivalent systems based on Mg, Ca and Al have also attracted significant interest in recent years.[22], [33], [43], [367], [368] Compared with metallic Li anode, these metallic anodes have much higher natural metal abundancy, and are reported to be less prone to dendrite formation,[33], [41], [43], [171], [368]–[372] potentially due to their lower self-diffusion barriers.[21], [22], [373] Among them, the Ca-ion system has demonstrated significant potential to replace LIBs. It has a comparable volumetric capacity and energy density to Li, and compared with other multivalent systems like Mg, it also has the advantages of lower reductive potential, lower charge density.[22]

While its development has been historically slow in part due to anode surface passivation from the formation of $CaCl_2$, $Ca(OH)_2$, or $CaCO_3$, which block Ca ion diffusion,[32], [169], [374], [375] there have been a few recent breakthroughs in electrolyte research that mitigates this issue [152], [153], [376], [377] and have demonstrated promising Ca-based electrolytes that are capable of plating and stripping with relatively high efficiency at moderately elevated[32] or room-temperatures.[33], [41], [42]

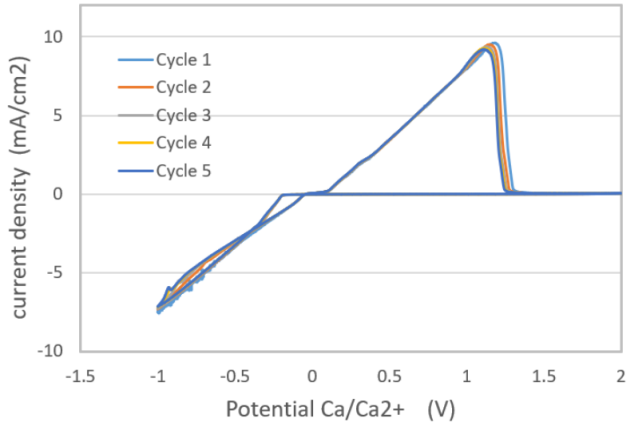
However, since research into Ca-ion electrolytes is still at an early stage, little work has been done to systematically study their plating and stripping processes. In order to better evaluate the performance of metallic Ca anodes, and to provide a deeper understanding of this system for future optimization, we have conducted this work which studies its plating and cycling behaviors under various conditions using in-situ TEM.

5.2 Experimental Conditions

5.2.1 Electrolyte preparation and quality check

The Ca-ion based electrolyte was prepared as 1 M $Ca(BH_4)_2$ dissolved in tetrahydrofuran (THF), as per the work of Wang *et al*.[33] This electrolyte was selected since it was the only room-temperature reversible Ca-electrolyte at room temperature when I started this project in 2018 and it also has the highest reported coulombic efficiency and forms minimal by-products compared with other Ca-ion based systems.[32], [169], [374], [375] The 1 M concentration was chosen since it is a commonly used concentration for LIB electrolytes, and using higher concentrations will usually risk blocking the liquid cell TEM system.

Before running any test on it, the quality of the electrolyte was first tested using cyclic voltammetry in a standard three-electrode cell (Ca as the reference electrode, Pt as the working and the counter electrode). The result is shown in Figure 5.2.1.1;



Cycle No.	Cycle 1	Cycle 2	Cycle 3	Cycle 4	Cycle 5
Coulombic Efficiency	88.6%	87.8%	87.5%	87.6%	87.3%

Figure 5.2.1.1 *cyclic voltammetry and calculated coulombic efficiency of each cycle using the 1 M $Ca(BH_4)_2$ Ca-electrolyte.*

Figure 5.2.1.1 shows that despite being lower than the reported 94% by Wang [33] (possibly the result of using a lower concentration [32], [378] or skipping the pre-reduction process), a relatively high coulombic efficiency of almost 90% was achieved in our electrolyte. This indicates our electrolyte has good cyclability and is representative enough for our plating morphology study.

5.2.2 Liquid-Cell TEM for in-situ visualization

We employed the JEOL JEM-3000F FEGTEM, coupled with a Protochips Poseidon 510 liquid-cell electrochemical transmission electron microscopy (TEM) holder for the in-situ TEM experiments. The TEM JEOL 3000, operated at 300 kV, was set to use a 50-micron condenser aperture and a spot size 2. The details of this in-situ are discussed by Unocic *et al.*[379] and is also illustrated by the schematics shown here in Figure 5.2.2.1:

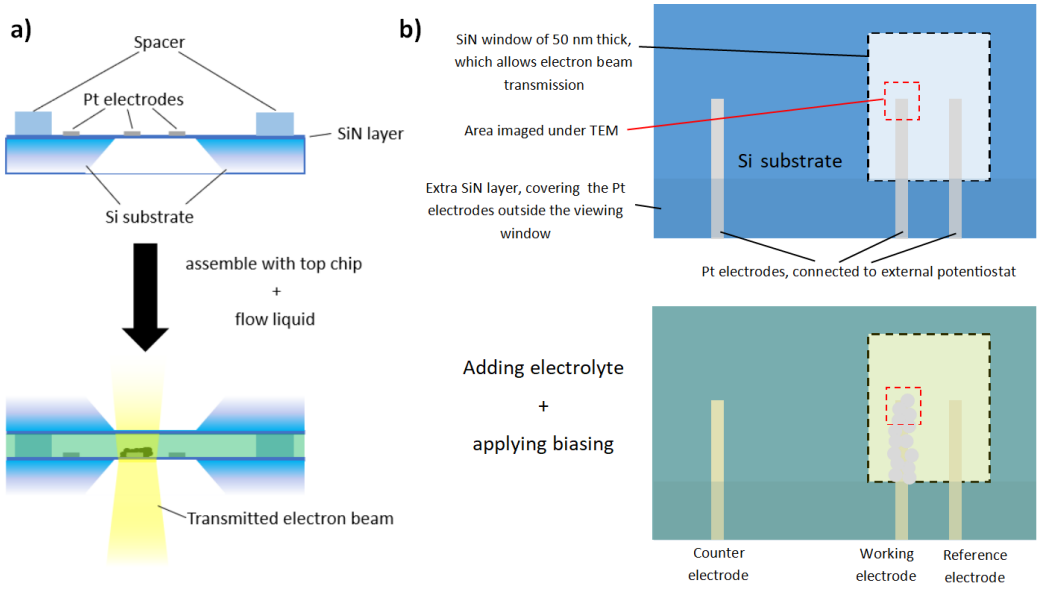


Figure 5.2.2.1. Illustrative schematics of the in-situ TEM liquid-cell. *(a) Side-on cross-section views of the cell assembly. One Si chip has patterned electrodes. (b) Top-down view of the electrode geometry, showing the working and reference electrodes situated on the electron-transparent SiN window.*

Figure 5.2.2.1 shows that the in-situ cell uses two silicon chips to seal the liquid electrolyte, screening it from the TEM column vacuum (Figure S2a). The chips are pre-fabricated with an electron transparent SiN window. A thin layer of electrolyte was confined between the two windows with a 120 nm spacer. A flow rate of 400 µl h^{-1} was used during system purging and a flow rate of 80 µl h^{-1} was used during TEM imaging. The in-situ galvanostatic electrochemical study was performed by applying constant current between the working and counter Pt electrodes patterned on the chip via a Gamry Reference 600, during which any change on the work electrode was imaged with TEM and recorded. After the TEM imaging, the cell was then purged with tetrahydrofuran (THF) for 2 hours before taken back to the glovebox and disassembled. The post-mortem chip was then studied using SEM.

Three different current densities were used for the in-situ TEM study, 1, 10 and 100 mA cm^{-2}. 20 and 50 mA cm^{-2} were also performed within the same set-up but only looked at post-mortem with SEM. The driven current density is calculated as the total current applied by the potentiostat, divided by the exposed Pt electrode surface area measured with scanning electron microscope (SEM) images. Due to the small size of the electrode this current density could be exaggerated, and the real current density could be smaller due to any electrode roughness and porosity increasing its effective area.

It has been shown that TEM imaging can lead to beam damage on the samples including heating, electrostatic charging, atom displacement and sputtering etc.[380] In battery studies, it can lead to problems like unwanted reduction of active materials, decomposition of electrolyte etc.[381] To minimize any beam effect which can potentially lead to unwanted reactions, TEM imaging was performed at a low electron dose rate of ≤ 0.04 electrons $Å^{-2}$ s^{-1} at all times, [16] which was checked using a Faraday cup, we also minimized the total continuous imaging time to no more than 150 s, and then beam blanked between experiments to minimize beam damage and allow electrolyte replenishment.

5.2.3 Three-electrode cell for plating & cycling for ex-situ studies

For ex-situ samples, galvanostatic plating and cycling was performed in a standard three-electrode cell (Ca as the counter and reference electrode, Pt as the working electrode) was used for Ca metal deposition and cycling experiments via a Gamry Reference 600 instrument under ambient conditions.

5.2.4 SEM & EDS

SEM was performed using a Carl Zeiss Merlin SEM using the secondary electron detector coupled with an energy dispersive X-ray spectroscopy (EDS) detector for element identification and mapping.

5.2.5 XRD

X-ray diffraction was performed using a Rigaku MiniFlex 600 in a nitrogen environment glovebox. with '2Θ' from 20 to 80 degrees

5.2.6 Mass Spectroscopy

A Thermo Fischer quadrupole mass spectrometer with Ar carrier gas flown at a constant rate of 0.8 µl min^{-1} was used to quantitatively compare the amount of Ca:CaH_2 within the Ca deposit. For every study, galvanostatic plating was performed on a Pt foil as the working electrode and a Ca plate as the counter electrode. After plating, the Pt foil was washed with THF, dried, sealed in a vial then connected to the MS. 1 ml of 1M D_2SO_4 in D_2O (dideuterosulfuric acid solution) was added into the vial containing the deposited electrode. The Ca:CaH_2 ratio within the deposit can be found from the amount of D_2 and DH gas detected using DEMS, according to the following reaction:[33]

$$Ca+D_2SO_4 \rightarrow D_2 + CaSO_4$$

$$CaH_2 + D_2 \rightarrow 2HD + CaSO_4$$

5.3 Results and Discussion

5.3.1 The change of plating morphology over cycling

Cyclic voltammetry was initially used in the in-situ TEM experiments within the range of -3V and +1V V.S. Platinum. The results are shown in Figure 5.3.1.1:

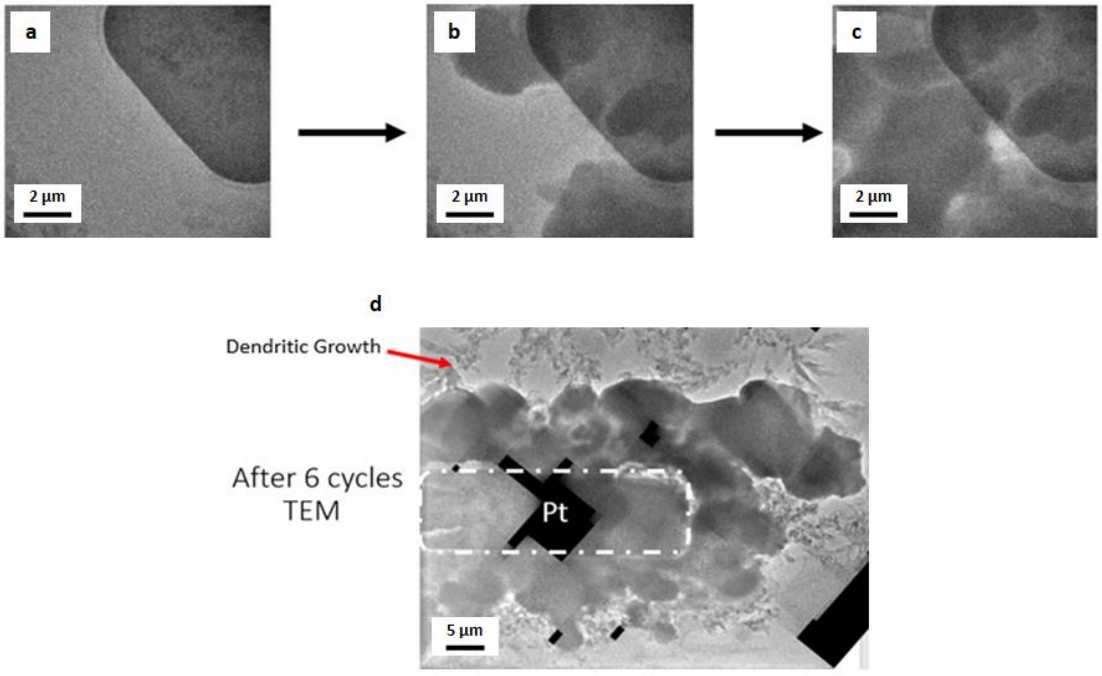


Figure 5.3.1.1 *In-situ electrochemical TEM using cyclic voltammetry, a-c: the initial Ca deposition captured in-situ, d: overall Ca deposition morphology after 6 cycles*

Figure 5.3.1.1 a-c shows that during the initial plating process, the deposited Ca metal was mainly in the form of globules, which is consistent with the previous belief that multivalent battery systems' metallic deposition are less prone to dendrite formation [33], [41], [43], [171], [368]–[372]. However, after running 6 cycles and purging the cell, we also looked at the overall Ca deposition morphology outside the field of view for in-situ imaging, where we observed a clear transition: a dendritic morphology actually formed on top of the globular structure, as indicated in c. This in rather interesting and we believe it could be the result of different current density. Since during cyclic voltammetry, an increasingly bigger negative over potential was applied. This increasingly large driving force for Ca electrodeposition on the working electrode led to a higher Ca^{2+} ion diffusion and charge transfer rate, which resulted in a higher plating current density.

5.3.2 Calcium dendrite formation at high current density

To verify that dendrite formation is the result of high current density, we first imaged the Ca plating morphology at a 100 mA cm^{-2} current density using the in-situ TEM. Galvanostatic cycles were performed. For each cycle, a negative bias was applied for 15 seconds, followed by a positive bias for another 15 seconds. The load curve of the first two cycles together with the relevant TEM images are shown in Figure 5.3.2.1:

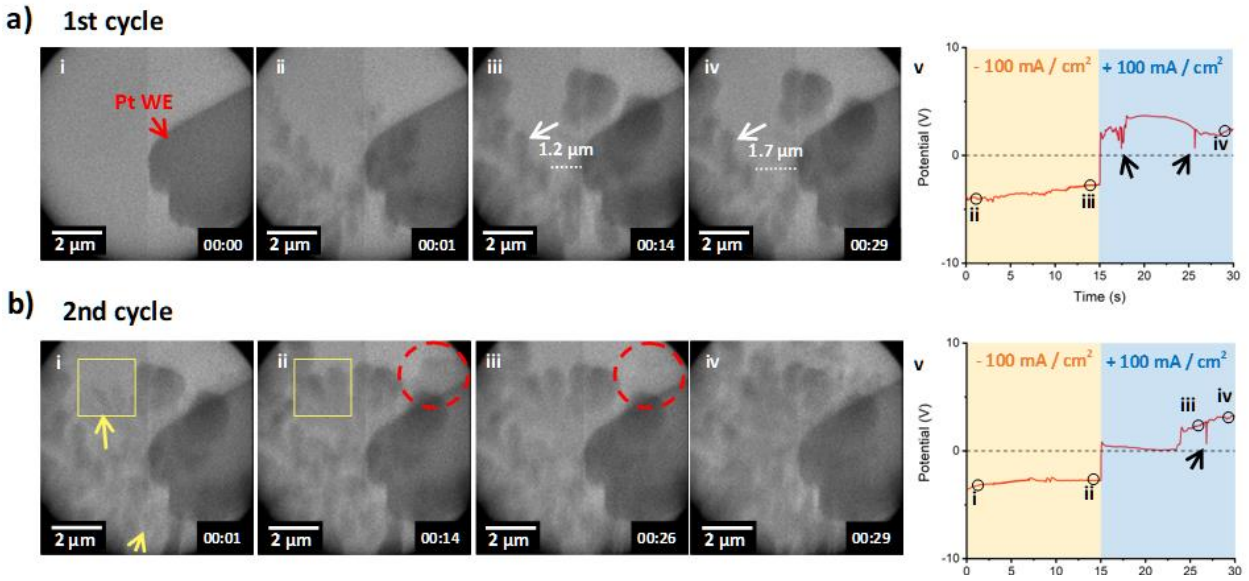


Figure 5.3.2.1 *Dendritic growth from Ca electrolyte under high current density. In-situ electrochemical TEM of (a) the first galvanostatic cycle and (b) the second galvanostatic cycle.*

Figure 5.3.2.1 shows the cycling behaviors of the first two cycles (a is the first cycle, b is the second cycle), the load curve for each cycle is shown in v while i to iv shows the Ca plating morphology on the working electrode at each corresponding spot on the curve. The lightest-colored region correspond to the electrolyte and the dark-colored rod, as indicated by the red arrow in Figure 5.3.2.1 1 a I, is the Pt working electrode. The deposited Ca metal has a color lighter than the Pt, but darker than the electrolyte. These different features can be more clearly distinguish and tracked in the real-time movies, which has been published.[172] From Figure 5.3.2.1 1 a i and ii, it can be seen that as soon as the negative potential was applied, a sharp dendrite nucleated from the tip of the Pt electrode and rapidly grew out of the field of view within less than a second, as shown in Figure 5.3.2.1 1 a ii. This dendritic growth has not been reported in Ca-ion systems,[33], [171] but is similar to previous studies in Li-ion systems with a similar cell setup.[16], [278] Upon reversing the current, some Ca dendrites gradually detached from the Pt electrode and drifted away, whose displacement is indicated by the white arrows

in Figure 5.3.2.1 a iii and iv. This corresponds to the stripping process and formation of 'dead calcium'.[33] Just like the 'dead lithium' observed in Li-ion batteries,[12] these 'dead calcium' are electrically isolated from the electrode, resulting in inactive Ca deposits that cannot be stripped away, and thus reduced coulombic efficiency. Also of interest are the features denoted with black arrows at 17 and 26 seconds in Figure 1a v, which are indicative of short-circuit events. This suggests that the two Pt electrodes, 200 microns apart, had been bridged by the deposited Ca metal within 17 seconds, suggesting a rapid dendrite growth rate of at least 11.7 $\mu m\ s^{-1}$.

In the second cycle (Figure 1b), sharp dendrites nucleated from the gaps unoccupied by the existing Ca dendrites, as indicated by the yellow arrows in Figure 1b i. Upon reversing the current, Ca stripping was observed, indicated by the red circles in Figure 1b ii and iii, as a Ca deposit gradually reduced in size and finally disappeared. With continued application of the reversed bias, more dendrites formed on top of the existing Ca deposits, originating from outside the field of view away from the working electrode, causing another short-circuit (black arrow, Figure 1b v). This suggests that these dendrites were from plating on the counter electrode, and grew across to the working electrode. As more dendrites formed, such short-circuit events became more frequent, demonstrated in the 3rd and 4th cycles' load curves, as shown in Figure 5.3.2.2:

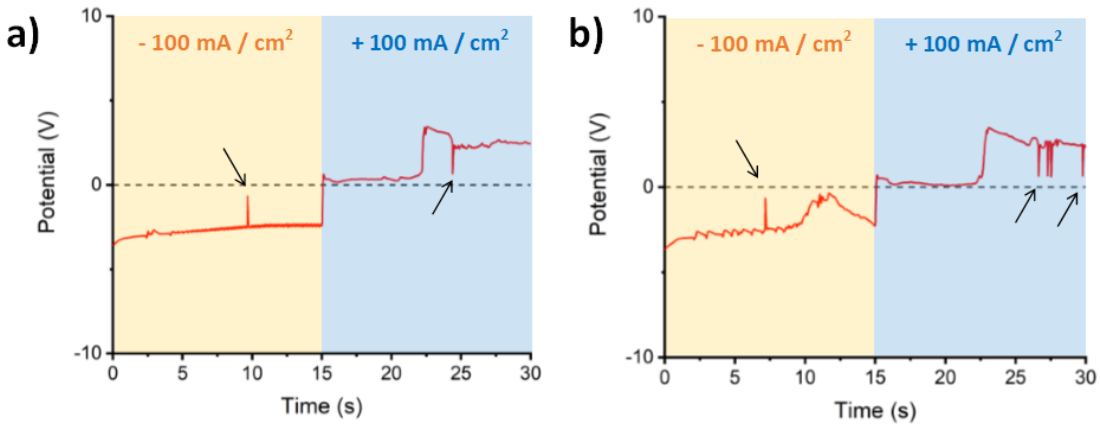


Figure 5.3.2.2 *Third and fourth cycles of high current density cell. (a) Third and (b) fourth galvanostatic cycles for the cell cycled at - 100 mA cm^{-2} for 15 s then + 100 mA cm^{-2} for 15 s. Black arrows indicate short-circuit events. Each plating/stripping had a total passed charge of 18 µC.*

In some situations, it can be challenging to distinguish different features with liquid cell imaging. This is due to the nature of liquid cell TEM, in which the contrast of the imaged specimen is not only dependent on the material's density but also on its thickness.[381] Therefore, it is quite useful to employ other techniques to future confirm our results. Here, after four cycles, the liquid-cell was purged by flowing tetrahydrofuran (THF), disassembled in an argon glovebox, and the post-mortem Ca deposit examined under SEM *via* an environmental transfer unit, screening it from air exposure, as shown in Figure 5.3.2.3:

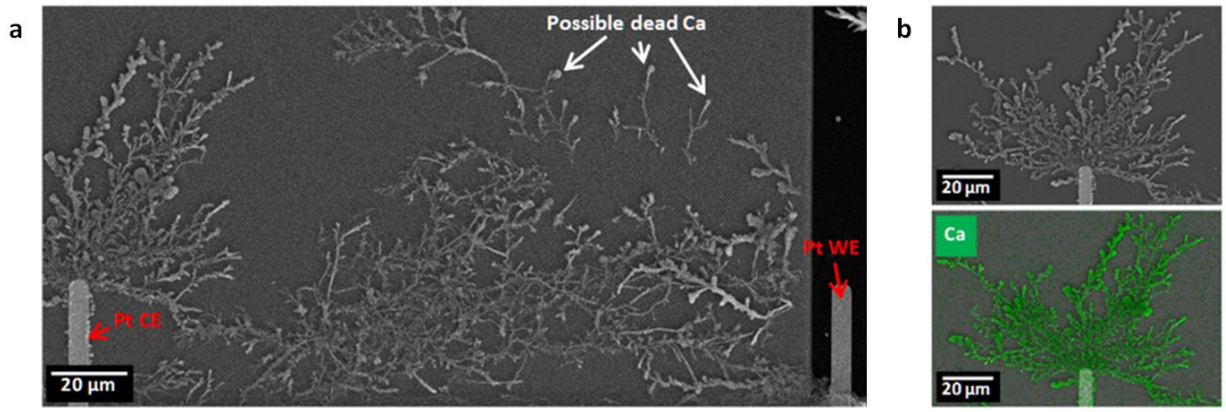


Figure 5.3.2.3 *(a) SEM image of the disassembled cell after an in-situ TEM experiment, showing the short circuiting between the two electrodes from Ca dendritic growth. (b) SEM and EDS mapping of the counter electrode.*

Figure 5.3.2.3 clearly shows that the deposited dendrites have bridged between the working and counter Pt electrodes, which further confirmed the origin of the short-circuit events. (Note: most of the Ca deposit on the working electrode was unavoidably lost during cell disassembly). In addition, some Ca dendrites were detached from the rest of the deposit and the electrodes, as indicated by the white arrows. These are likely to be 'dead calcium' dendrites, as per our previous observation under in-Situ TEM. The dendrites formed at the Pt counter electrode were characterized by energy-dispersive x-ray spectroscopy (EDS) mapping, confirming these dendrites to consist of Ca. More SEM images with higher magnification of the dendrite are shown in Figure 5.3.2.4, which reveal the characteristic branching fractal structure, comparable to those reported in other metallic systems.[382]–[384]

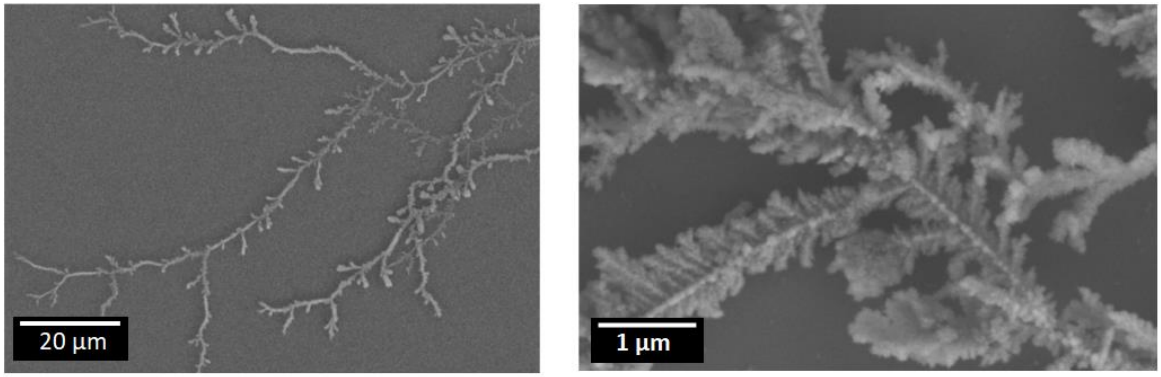


Figure 5.3.2.4. *SEM images showing the dendrite morphology plated at 100 mA cm^{-2}.*

5.3.3 Calcium globular plating at medium and low current densities

To verify that the dendrite formation was the result of high current density and for comparison, We performed further in-situ TEM studies at lower 1 mA cm^{-2} and 10 mA cm^{-2} current densities, which are more representative current densities for a practical cell. The results are summarized in Figure 5.3.3.1:

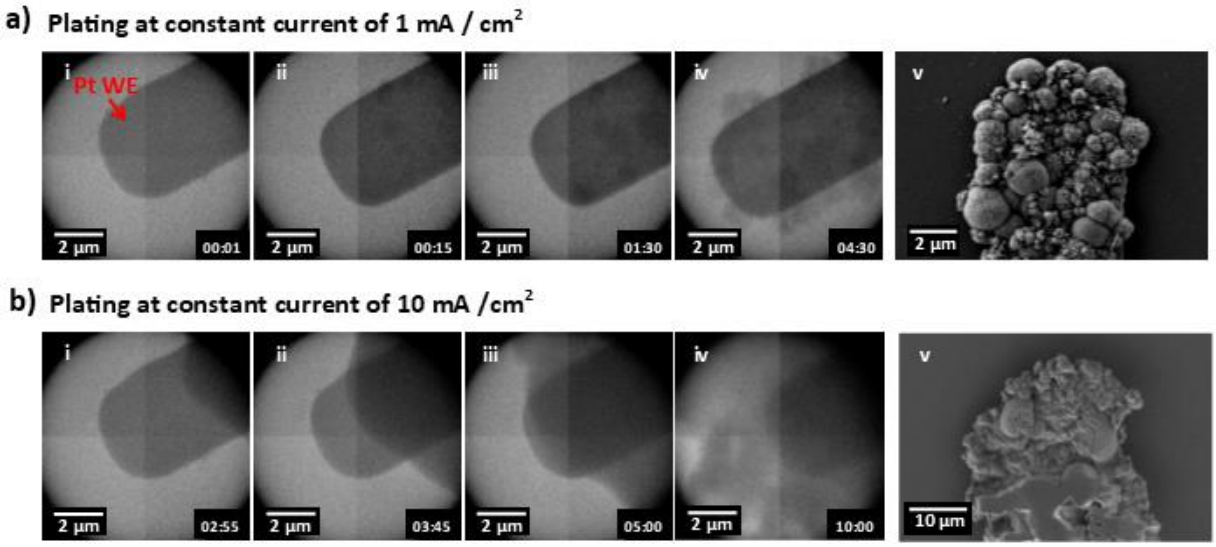


Figure 5.3.3.1 *Globular Ca plating at lower current densities. Ca plating at (a) -1 mA cm^{-2} and (b) -10 mA cm^{-2}. Panels i-iv show the in-situ electrochemical TEM recording, panel v show SEM images of the electrode after disassembling the liquid-cell.*

The corresponding charging curves of (a) and (b) are shown in Figure 5.3.3.2 and Figure 5.3.3.3:

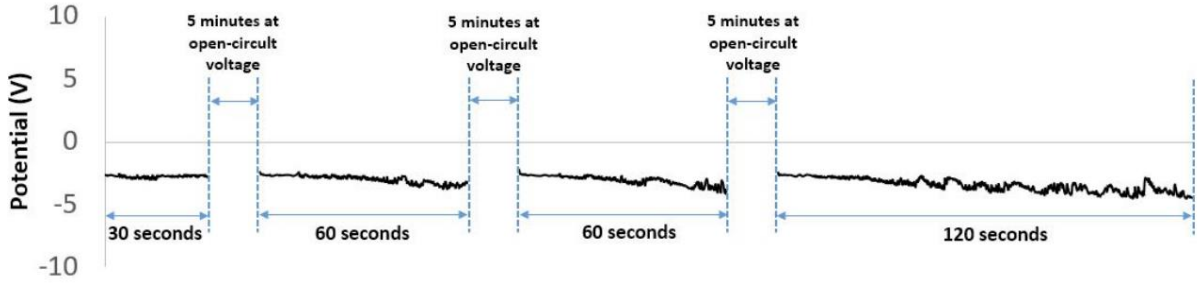


Figure 5.3.3.2 Galvanostatic plating at -1 mA cm-2 with a total plating time of 270 seconds and total passed charge of 0.8 µC.

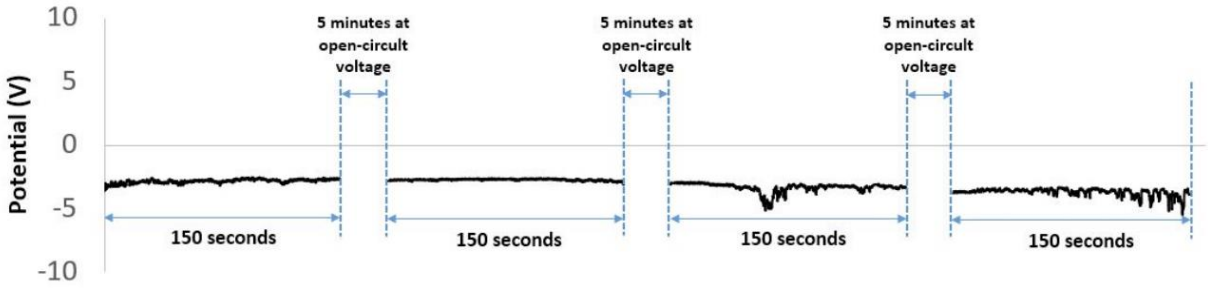


Figure 5.3.3.3 *Galvanostatic plating at -10 mA cm-2 with a total plating time of 600 seconds and total passed charge of 18 µC.*

Figure 5.3.3.1 a shows that, unlike in the 100 mA cm^{-2} case, gradual globular growth occurs with a more uniform coverage of the Pt electrode when plating at 1 mA cm^{-2}, with no dendrite formation observed. When an intermediate current density of 10 mA cm^{-2} was applied, the electroplated Ca still exhibited globular growth with larger size than that in the 1 mA cm^{-2} case, with no clear dendrites observed. These observations show that plating morphology is highly dependent on current density.

5.3.4 Current density dependent globular-to-dendritic plating morphology transition

To construct a comprehensive understanding of this current-density dependent morphology transition, several in-situ TEM cells plated with the same capacity at different current densities were disassembled and their post-mortem deposits were studied under SEM. The results are shown in Figure 5.3.4.1:

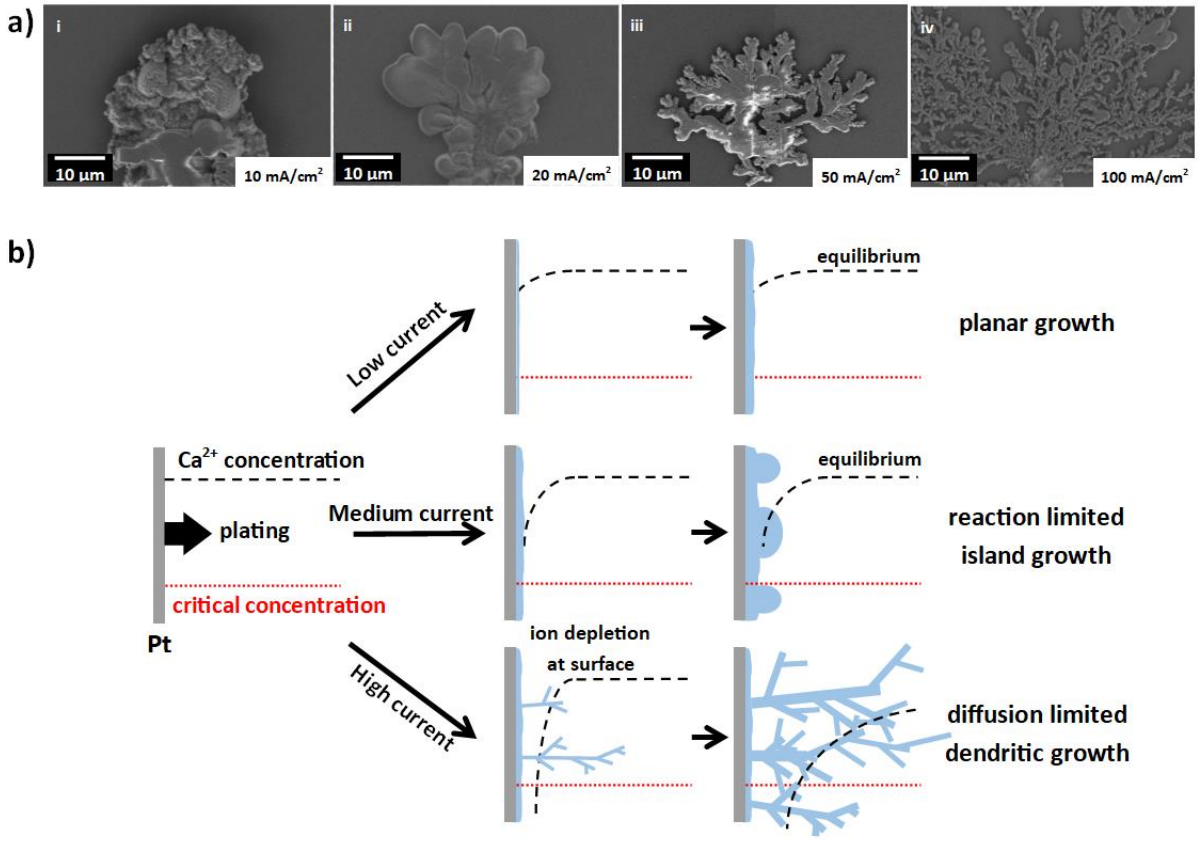


Figure 5.3.4.1 *Current-density dependent plating morphology transition. (a) i-iv: SEM images of the Ca plating morphology for 10m 20, 50, and 100 mA cm^{-2}, showing a change from globular to dendritic deposition with increased current density. (b) Illustration showing a model for expected electrodeposition growth.*

Figure 5.3.4.1 a shows that a gradual transition from globular/island to dendritic growth as the plating current density was increased from 10 to 20, 50 and 100 mA cm^{-2} (i-iv). Each study passed 18 µC total

charge, with different amounts of Ca deposition imaged due to losses during cell disassembly. This current density dependent transition from globular/island to dendritic growth is consistent with the conventional model used to describe electrodeposition growth (Figure 5.3.4.1 b), and is also consistent with the previous theory proposed for Li-ion battery systems. At lower rates, the ion diffusion rate towards the plating interface is at equilibrium with the Ca^{2+} ion reduction/depletion rate. However, at higher current densities, the ion diffusion rate is not fast enough to compensate the ion depletion rate due to reduction and deposition, with this loss of equilibrium leading to dendrite formation.[17]

Based on this morphology-current relation, a critical current density limit for ion depletion, and thus dendrite formation, can be roughly estimated for our in-situ TEM electrochemical cell. With a flow rate of 80 µL hr^{-1}, it takes less than a second to replace all the electrolyte within the enclosed cell, which allows the ion concentration to be restored to the nominal value of 1 M. Using the diffusion length equation $d = \sqrt[2]{4 \cdot D_{\mathrm{Ca}} \cdot t}$ (*d* is the diffusion length, *t* is the time allowed for diffusion, D_{Ca} is the Ca ion diffusion coefficient, which is estimated to be 7.4×10^{-7} $cm^2\,s^{-1}$ for this system by Kim, *et al*.[171]), we can estimate the limiting Ca deposition rate at the surface to be 1.7×10^{-6} mol cm^{-2} s^{-1}, which corresponds to a limiting plating current density of 55 mA cm^{-2}. (Note: We took into account that the current density at the edge of the electrode is three times higher than the nominal applied current density.[365]) This value is comparable to some of the reported values in Li-ion battery systems.[17], [385] It should be noted that this value is estimated specifically for our system (1 M $Ca(BH_4)_2$ in THF within the electrochemical liquid-cell TEM set-up) and cannot be directly applied to other systems. The critical current density is expected to be lower for most other systems, as there is no constant electrolyte replenishment, and the overall applied current is larger due to their bigger electrode size. Even within our system, this value is somewhat overestimated since we do see evidence of dendrite formation at 50 mA cm^{-2}, as shown in Figure 5.3.4.1 a iii. This is most likely because the diffusion of the

Ca ions is limited within the confined sub-micron space between the encapsulating cell membranes, a phenomenon that has been previous reported in liquid-cell TEM set-ups.[265], [381], [386], [387]

5.3.5 Dendrite formation at lower current densities

Our in-situ TEM studies are mostly consistent with the expected model for the current density dependence of electroplating morphology, however deviations from it were also observed, as shown in Figure 5.3.5.1:

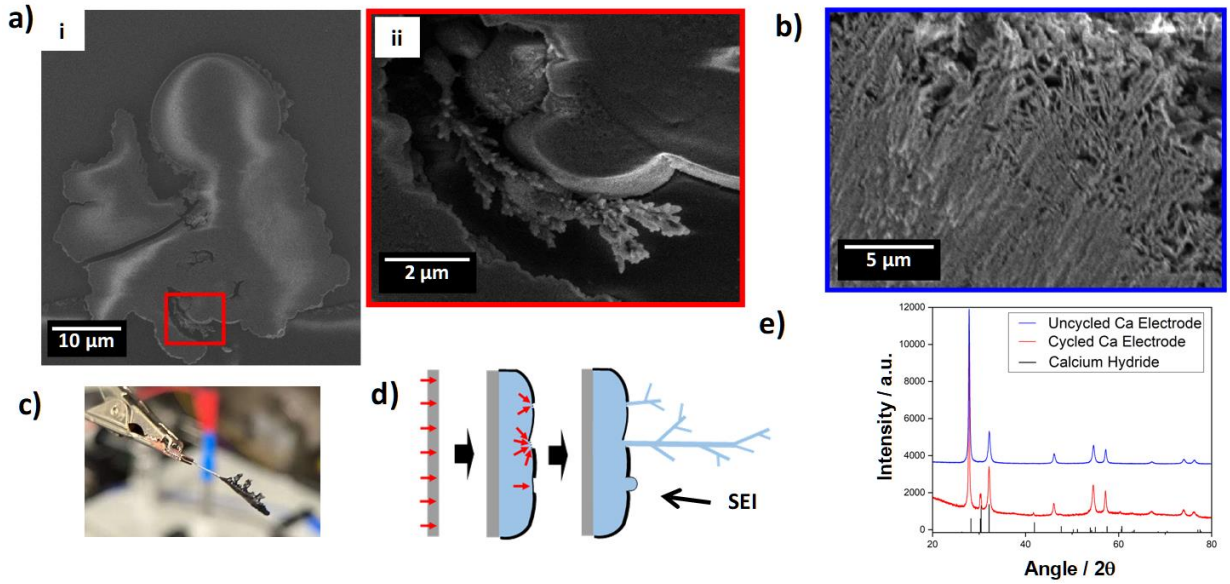


Figure 5.3.5.1 *(a) i: SEM image of a Ca globular plating deposit formed at 10 mA cm^{-2}. ii: Magnified view of the indicated area reveals that a dendrite has formed, potentially due to localized high-current density caused by a heterogeneous SEI layer. (b) SEM cross-section image of potentiostatically plated Ca on a Pt foil working electrode from an electrolytic cell reveals localized dendrites (see also Supporting Figure S7). (c) Post-mortem photograph of dendritic deposition after galvanostatic plating at 5 mA cm^{-2} for 5 hrs. (d) The influence of SEI inhomogeneity on dendrite nucleation (plated Ca blue, SEI layer black, current red). (e) XRD showing the formation of CaH_2 on the metallic Ca plate after cycling for 10 hours.*

Figure 5.3.5.1 a shows the morphology of a further Ca deposit plated under the same conditions as the 10 mA cm^{-2} deposition in Figure 5.3.4.1. Despite the overall globular morphology being consistent with our previous results, upon closer examination of the region highlighted by the red box dendrite

formation can be seen (ii). This is unexpected at such a relatively low current density according to the standard electroplating model, which is even lower than the typically reported current density for dendrite formation in Li-ion systems.[17], [385] This observation suggests an additional factor governing the conditions for dendrite growth when cycling a Ca electrolyte. We propose that the presence of an irregular solid electrolyte interface (SEI) layer explains our observations. The irregularity of this SEI leads to the presence of local current density inhomogeneities during plating,[33], [171] and thus yields local high-current concentration spots. These 'hot spots' could exhibit current densities significantly higher than the nominal current density, and so dendrites could potentially nucleate from these spots. Post-mortem cross-sectional SEM imaging of Ca deposition reveals similar localized dendrite formation at low current densities (Figure 5.3.5.1 e). This phenomenon is illustrated schematically in Figure 5.3.5.1 d. We suggest that this 'hot-spot' dendrite formation can result in failures in standard Ca cells; we observe heavy and irregular Ca plating in an electrolytic cell operated under relevant current densities (Figure 5.3.5.1 c), using a Pt foil working electrode with 1 cm^2 surface area and a Ca counter electrode with galvanostatic plating at 5 mA cm^{-2}. Dendrite-like Ca deposits can be seen, concentrating at the Pt foil edge. This indicates that dendrite formation is not necessarily a consequence of plating within a confined nanoscale space at high current density, but can also occur in macroscopic spaces under relatively low current density.

X-ray diffraction (XRD) was employed to explore the existence of any crystallized species in the SEI, using a conventional two-electrode beaker cell cycled at 1 mA cm^{-2} for 10 hours with metallic Ca plates as both electrodes, each with a surface area of around 20 mm^2. Additional peaks appeared on the working electrode after cycling (blue line), Figure 4e, corresponding to the formation of CaH_2, whose reference XRD pattern is shown for comparison. The formation of the additional chemical component on the foil after cycling is likely attributable to the formation of a CaH_2 containing SEI layer, suggested by

previous studies with this electrolyte,[33] however it is likely that it is accompanied by additional organic components.

5.3.6 Quantifying the CaH_2 SEI formation process

To better understand CaH_2 formation in the SEI and its relationship with current density and capacity, differential electrochemical mass spectrometry (DEMS) was used to quantify the plating at different conditions as shown in Figure 5.3.6.1:

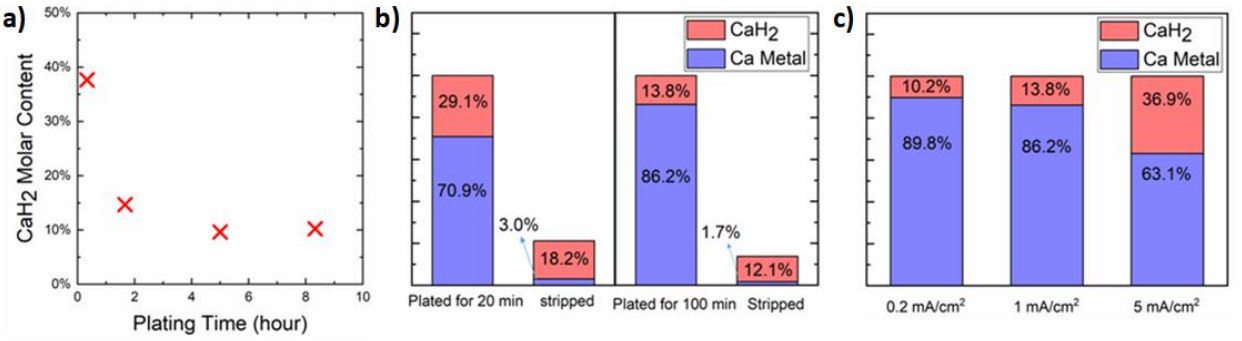


Figure 5.3.6.1 *Characterizing the passivating SEI layer by DEMS measurements for Ca/CaH_2 ratio plated onto Pt foils. (a) The mol% CaH_2 content of the deposit with respect to plating time at constant plating current of 0.2 mA cm^{-2}. (b) Comparison of the Ca/CaH_2 ratio after plating at 1 mA cm^{-2} for 20 min and 100 min, and after stripping. (c) The Ca/CaH_2 ratio after plating at different current densities but with constant total charge; 0.2 mA cm^{-2} for 500 min, 1 mA cm^{-2} for 100 min, 5 mA cm^{-2} for 20 min.*

Figure 5.3.6.1 a shows that, when plated at 0.2 mA cm^{-2}, the CaH_2/Ca ratio declined with increasing deposition time and stabilized at around 10%. This suggests that most of the CaH_2 formed at the beginning of the plating with fresh Ca deposits, and that the presence of CaH_2 prevented the newly deposited Ca from undergoing further side reactions with the electrolyte. A similar trend was observed at 1 mA cm^{-2} during plating, as shown in Figure 5.3.6.1 b with 70.9 % of Ca deposited in 20 mins and 86.2 % deposited in 100 mins. The relatively high CaH_2 content compared to previous work could be due

to the lower electrolyte concentration and therefore less dissociation of $Ca(BH4)_2$ used in this work, suggesting the effect of electrolyte concentration in determining the cell performance. Figure 5.3.6.1 b also shows that, when a reversed current was supplied to strip the plated deposit, the majority of the CaH_2 content remained while most of the Ca content disappeared. The remaining metallic Ca content after stripping is likely the 'dead calcium' electrically isolated from the electrode, consistent with our previous TEM observations. This also suggests that the CaH_2 SEI does not inhibit the stripping process of the metallic Ca, unlike passivating SEI layers previously reported in other Ca-ion systems.[32], [169], [374], [375] We further increased the current density and compared the plating process under different current densities while keeping the total passed charge the same; i.e., plating at 0.2 mA cm^{-2} for 500 minutes, 1 mA cm^{-2} for 100 minutes and 5 mA cm^{-2} for 20 minutes. This is shown in Figure Figure 5.3.6.1 c. Similar amounts of CaH_2 were found at relatively low current densities, while a clear increase of the CaH_2 content from 10.2 % to 36.9 % was observed at 5 mA cm^{-2}. This could be due to the higher overpotential applied for plating at 5 mA cm^{-2}, which could lead to the faster decomposition of THF that in turn may accelerate the formation of CaH_2, as suggested in ref. [4].

The formation of CaH_2 and the SEI has benefits and drawbacks. The presence of an SEI stops further reactions between the deposited Ca and the electrolyte, allowing extended plating at room temperature. However, despite not completely inhibiting the plating or stripping processes, the formation of the SEI led to slowing/partial blocking of Ca ion transport, which caused local current density inhomogeneity and unexpected dendrite growth. Therefore, it is important to consider the role of the SEI in Ca deposition, and its influence in instigating dendritic growth, when studying and developing Ca-ion electrolytes, which has been somewhat overlooked by previous studies.

5.3.7 Ca electroplating systematic study project summary

We performed a systematic study of Ca plating morphology with a Ca-ion electrolyte that shows great potential for developing Ca-ion batteries as a next-generation battery system. By using in situ TEM, we showed the real-time Ca plating processes with different current density regimes for the first time. A transition from globular to dendritic growth was observed as we increased the plating current density, which is in agreement with the expected behavior of an electroplated metal, and we observed the real-time formation of electrochemically isolated dead Ca deposits during stripping. Dendrite growth was occasionally observed under current density conditions that were well below that expected from the standard electroplating model, which we propose was due to the presence of an irregular SEI layer. The inhomogeneous nature of the SEI led to the presence of localized high current density regions that promoted dendritic deposition. Our work highlights that while Ca-ion batteries hold promise, challenges remain in understanding and managing their chemistry before they can be considered viable. Compared with other systems, Ca batteries suffer from issues like anode surface passivation, limited electrochemical window, relatively low CE etc. For future work, Ca electrolyte needs to be further optimized to achieve better anode reversibility and wider electrochemical window. Potential approaches include electrolyte modification, additives, protective layers etc.

6 Perspectives and Future Work

Batteries based on multivalent ions have been widely believed to be promising next-generation energy storage systems. Apart from their low cost, another key advantage of these systems is their anodes' relatively high stability. In this thesis, we looked specifically at two of these multivalent systems, the aqueous zinc battery and the calcium-ion battery. We systematically studied these systems' metallic anodes. In Chapter 3 we looked at the aging-induced degradation in $ZnSO_4$-based aqueous zinc battery (AZB). We found that cell aging can lead to significant anode capacity loss, in some cases over 70% efficiency loss after only 24 hours of aging. This phenomena was aggravated by use of longer aging time, higher anode loading, and lower charging rates, and ultimately led to poor post-aging reversibility and short cell shelf life. We also found that while the loss was partly from the irreversible Zn loss due to the formation of corrosion products like ZHS, it was mostly due to the presence of 'inactive Zn'. We also revealed that 'inactive Zn' formed due to gas bubble formation and accumulation at the anode interface during aging, ionically insulating Zn from the electrolyte and thus unable to be dissolved during electrostripping. And by simply degassing the cells, these 'inactive Zn' can be 'reactivated' to restore a significant portion of the lost capacity. Apart from the aging problem, in Chapter 4, we have also looked at a possible anode strategy to mitigate the dendrite problem in the $ZnSO_4$-based AZBs. By employing single-crystal (002) Zn as an ideal model anode, we have shown that, via promoting textured planar deposition and defect-suppression, the dendrite problem can be resolved and excellent cell performance can be achieved in AZBs at an unprecedented high rate of 200 mA cm^{-2} and after prolonged cycling (>1,200 cycles). This presents a new strategy to preventing dendrites in aqueous zinc batteries and potentially in other battery systems as well. In Chapter 5, we turned to look at the relatively new room temperature Ca-ion organic electrolyte system. by using in situ TEM, we revealed the plating morphology transition from globular to dendritic as we increased the plating current density. We also found that dendrite growth can also occur under low current density conditions, which was found to be

due to the presence of an irregular SEI layer. The inhomogeneous nature of the SEI led to the presence of localized high current density regions that promoted dendritic deposition. Overall, our work has shown that despite being relatively stable, metallic anodes in AZB and Ca-ion battery systems do still suffer from issues like aging-induced 'inactive Zn' and low-rate Ca dendrite formation which have been largely overlooked in the past. My work has demonstrated the root cause of these problems, based on which more strategies should be designed accordingly to try to mitigate these problems to further optimize the anode performance in these batteries. For AZBs, to reduce the aging-induced 'inactive Zn', electrolyte additive, protective layer, anode engineering and degassing mechanisms could be employed to reduce the gas formation and to remove the aging-induced gas. We have demonstrated that single-crystal Zn anode can be used to achieve less corrosion and planar Zn deposition. However, it is not yet commercially viable due to its current high cost. So, we can look at ways to reduce its cost and look at alternative anode materials and methods to achieve such planar deposition in AZB. For Ca batteries, the electrolyte should be further optimized to widen its electrochemical window, and to avoid anode passivation to achieve better anode stability and reversibility. Only when these obstacles have been properly tackled will these systems be commercialized as stable and safe energy storage systems.

7 Bibliography

[1] M. Winter, B. Barnett, and K. Xu, "Before Li Ion Batteries," *Chemical Reviews*, vol. 118, no. 23. American Chemical Society, pp. 11433–11456, Dec. 12, 2018. doi: 10.1021/acs.chemrev.8b00422.

[2] B. Scrosati, "History of lithium batteries," *Journal of Solid State Electrochemistry*, vol. 15, no. 7–8. Springer, pp. 1623–1630, Jul. 04, 2011. doi: 10.1007/s10008-011-1386-8.

[3] F. Schipper and D. Aurbach, “A brief review: Past, present and future of lithium ion batteries,” *Russ. J. Electrochem.*, vol. 52, no. 12, pp. 1095–1121, Dec. 2016, doi: 10.1134/S1023193516120120.

[4] G. N. Lewis and F. G. Keyes, “The potential of the lithium electrode,” *J. Am. Chem. Soc.*, vol. 35, no. 4, pp. 340–344, 1913, doi: 10.1021/ja02193a004.

[5] M. V. Reddy, A. Mauger, C. M. Julien, A. Paolella, and K. Zaghib, “Brief history of early lithium-battery development,” *Materials (Basel).*, vol. 13, no. 8, Apr. 2020, doi: 10.3390/MA13081884.

[6] D. Deng, “Li-ion batteries: Basics, progress, and challenges,” *Energy Science and Engineering*, vol. 3, no. 5. John Wiley & Sons, Ltd, pp. 385–418, Sep. 01, 2015. doi: 10.1002/ese3.95.

[7] N. Nitta, F. Wu, J. T. Lee, and G. Yushin, “Li-ion battery materials: Present and future,” *Materials Today*, vol. 18, no. 5. Elsevier, pp. 252–264, Jun. 01, 2015. doi: 10.1016/j.mattod.2014.10.040.

[8] A. Masias, J. Marcicki, and W. A. Paxton, “Opportunities and Challenges of Lithium Ion Batteries in Automotive Applications,” *ACS Energy Letters*, vol. 6, no. 2. American Chemical Society, pp. 621–630, Feb. 12, 2021. doi: 10.1021/acsenergylett.0c02584.

[9] G. Pistoia and B. Liaw, *Behaviour of Lithium-Ion Batteries in Electric Vehicles*, no. July. 2018. [Online]. Available: https://link.springer.com/content/pdf/10.1007%2F978-3-319-69950-9.pdf

[10] B. Liu, J. G. Zhang, and W. Xu, “Advancing Lithium Metal Batteries,” *Joule*, vol. 2, no. 5. Cell Press, pp. 833–845, May 16, 2018. doi: 10.1016/j.joule.2018.03.008.

[11] X. Gao *et al.*, “Thermodynamic Understanding of Li-Dendrite Formation,” *Joule*, vol. 4, no. 9. Cell Press, pp. 1864–1879, Sep. 16, 2020. doi: 10.1016/j.joule.2020.06.016.

[12] C. Fang *et al.*, “Quantifying inactive lithium in lithium metal batteries,” *Nature*, vol. 572, no. 7770, pp. 511–515, Aug. 2019, doi: 10.1038/s41586-019-1481-z.

[13] A. J. Louli *et al.*, “Diagnosing and correcting anode-free cell failure via electrolyte and morphological analysis,” *Nat. Energy*, vol. 5, no. 9, pp. 693–702, Aug. 2020, doi: 10.1038/s41560-020-0668-8.

[14] J. W. Choi and D. Aurbach, “Promise and reality of post-lithium-ion batteries with high energy densities,” *Nat. Rev. Mater.*, vol. 1, 2016, doi: 10.1038/natrevmats.2016.13.

[15] A. Kushima *et al.*, “Liquid cell transmission electron microscopy observation of lithium metal growth and dissolution: Root growth, dead lithium and lithium flotsams,” *Nano Energy*, vol. 32, pp. 271–279, Feb. 2017, doi: 10.1016/j.nanoen.2016.12.001.

[16] B. L. Mehdi *et al.*, “Observation and quantification of nanoscale processes in lithium batteries by operando electrochemical (S)TEM,” *Nano Lett.*, vol. 15, no. 3, pp. 2168–2173, Mar. 2015, doi: 10.1021/acs.nanolett.5b00175.

[17] P. Bai, J. Li, F. R. Brushett, and M. Z. Bazant, “Transition of lithium growth mechanisms in liquid electrolytes,” *Energy Environ. Sci.*, vol. 9, no. 10, pp. 3221–3229, Oct. 2016, doi: 10.1039/c6ee01674j.

[18] A. Ponrouch, J. Bitenc, R. Dominko, N. Lindahl, P. Johansson, and M. R. Palacin, “Multivalent rechargeable batteries,” *Energy Storage Materials*, vol. 20. Elsevier B.V., pp. 253–262, Jul. 01, 2019. doi: 10.1016/j.ensm.2019.04.012.

[19] D. Aurbach *et al.*, “Prototype systems for rechargeable magnesium batteries,” *Nature*, vol. 407, no. 6805, pp. 724–727, Oct. 2000, doi: 10.1038/35037553.

[20] H. Song and C. Wang, “Current Status and Challenges of Calcium Metal Batteries,” *Adv. Energy Sustain. Res.*, vol. 3, no. 3, p. 2100192, Mar. 2022, doi: 10.1002/aesr.202100192.

[21] A. Ponrouch and M. Rosa Palacín, “Post-Li batteries: Promises and challenges,” *Philosophical Transactions of the Royal Society A: Mathematical, Physical and Engineering Sciences*, vol. 377, no. 2152. Royal Society Publishing, Aug. 26, 2019. doi: 10.1098/rsta.2018.0297.

[22] J. Muldoon, C. B. Bucur, and T. Gregory, “Quest for nonaqueous multivalent secondary batteries: Magnesium and beyond,” *Chemical Reviews*, vol. 114, no. 23. American Chemical Society, pp. 11683–11720, Dec. 10, 2014. doi: 10.1021/cr500049y.

[23] E. M. Erickson *et al.*, “Review—Development of Advanced Rechargeable Batteries: A Continuous Challenge in the Choice of Suitable Electrolyte Solutions,” *J. Electrochem. Soc.*, vol. 162, no. 14, pp. A2424–A2438, Oct. 2015, doi: 10.1149/2.0051514jes.

[24] N. Xiao, W. D. McCulloch, and Y. Wu, “Reversible Dendrite-Free Potassium Plating and Stripping Electrochemistry for Potassium Secondary Batteries,” *J. Am. Chem. Soc.*, vol. 139, no. 28, pp. 9475–9478, Jul. 2017, doi: 10.1021/jacs.7b04945.

[25] H. Moriwake, A. Kuwabara, C. A. J. Fisher, and Y. Ikuhara, “Why is sodium-intercalated graphite unstable?,” *RSC Adv.*, vol. 7, no. 58, pp. 36550–36554, Jul. 2017, doi: 10.1039/c7ra06777a.

[26] Y. Kondo, T. Fukutsuka, K. Miyazaki, Y. Miyahara, and T. Abe, “Investigation of Electrochemical Sodium-Ion Intercalation Behavior into Graphite-Based Electrodes,” *J. Electrochem. Soc.*, vol. 166, no. 3, pp. A5323–A5327, Jan. 2019, doi: 10.1149/2.0431903jes.

[27] D. Datta, J. Li, and V. B. Shenoy, “Defective graphene as a high-capacity anode material for Na- and Ca-ion batteries,” *ACS Appl. Mater. Interfaces*, vol. 6, no. 3, pp. 1788–1795, Feb. 2014, doi: 10.1021/am404788e.

[28] X. Lu *et al.*, “Germanium as a Sodium Ion Battery Material: In Situ TEM Reveals Fast Sodiation Kinetics with High Capacity,” *Chem. Mater.*, vol. 28, no. 4, pp. 1236–1242, 2016, doi: 10.1021/acs.chemmater.6b00200.

[29] B. Lee, E. Paek, D. Mitlin, and S. W. Lee, “Sodium Metal Anodes: Emerging Solutions to Dendrite Growth,” *Chemical Reviews*. American Chemical Society, 2019. doi: 10.1021/acs.chemrev.8b00642.

[30] M. Song, H. Tan, D. Chao, and H. J. Fan, “Recent Advances in Zn-Ion Batteries,” *Adv. Funct. Mater.*, vol. 28, no. 41, pp. 1–27, 2018, doi: 10.1002/adfm.201802564.

[31] S. Hou *et al.*, “Solvation sheath reorganization enables divalent metal batteries with fast interfacial charge transfer kinetics,” *Science (80-.).*, vol. 374, no. 6564, pp. 172–178, Oct. 2021, doi: 10.1126/science.abg3954.

[32] A. Ponrouch, C. Frontera, F. Bardé, and M. R. Palacín, “Towards a calcium-based rechargeable battery,” *Nat. Mater.*, vol. 15, no. 2, pp. 169–172, Oct. 2016, doi: 10.1038/nmat4462.

[33] D. Wang, X. Gao, Y. Chen, L. Jin, C. Kuss, and P. G. Bruce, “Plating and stripping calcium in an organic electrolyte,” *Nat. Mater.*, vol. 17, no. 1, pp. 16–20, 2018, doi: 10.1038/NMAT5036.

[34] Y. Sun *et al.*, “Recent advances and challenges in divalent and multivalent metal electrodes for metal-air batteries,” *Journal of Materials Chemistry A*, vol. 7, no. 31. pp. 18183–18208, 2019. doi: 10.1039/c9ta05094a.

[35] Y. Liang, H. Dong, D. Aurbach, and Y. Yao, “Current status and future directions of multivalent metal-ion batteries,” *Nature Energy*, vol. 5, no. 9. Nature Publishing Group, pp. 646–656, Jul. 16, 2020. doi: 10.1038/s41560-020-0655-0.

[36] H. Pan *et al.*, “Reversible aqueous zinc/manganese oxide energy storage from conversion reactions,” *Nat. Energy*, vol. 1, no. 5, pp. 1–7, Apr. 2016, doi: 10.1038/nenergy.2016.39.

[37] Y. Zhang, H. Geng, W. Wei, J. Ma, L. Chen, and C. C. Li, “Challenges and recent progress in the design of advanced electrode materials for rechargeable Mg batteries,” *Energy Storage Materials*, vol. 20. Elsevier B.V., pp. 118–138, Jul. 01, 2019. doi: 10.1016/j.ensm.2018.11.033.

[38] J. Huang, Z. Guo, Y. Ma, D. Bin, Y. Wang, and Y. Xia, “Recent Progress of Rechargeable Batteries Using Mild Aqueous Electrolytes,” *Small Methods*, vol. 3, no. 1. John Wiley & Sons, Ltd, p. 1800272, Jan. 01, 2019. doi: 10.1002/smtd.201800272.

[39] C. Li, X. Xie, S. Liang, and J. Zhou, “Issues and Future Perspective on Zinc Metal Anode for Rechargeable Aqueous Zinc-ion Batteries,” *Energy and Environmental Materials*, vol. 3, no. 2. John Wiley & Sons, Ltd, pp. 146–159, Jun. 01, 2020. doi: 10.1002/eem2.12067.

[40] H. Jia *et al.*, “Recent advances in zinc anodes for high-performance aqueous Zn-ion batteries,” *Nano Energy*, vol. 70. Elsevier Ltd, p. 104523, Apr. 01, 2020. doi: 10.1016/j.nanoen.2020.104523.

[41] Z. Li, O. Fuhr, M. Fichtner, and Z. Zhao-Karger, “Towards stable and efficient electrolytes for room-temperature rechargeable calcium batteries,” *Energy Environ. Sci.*, 2019, doi: 10.1039/c9ee01699f.

[42] A. Shyamsunder, L. E. Blanc, A. Assoud, and L. F. Nazar, “Reversible Calcium Plating and Stripping at Room Temperature Using a Borate Salt,” *ACS Energy Lett.*, vol. 4, no. 9, pp. 2271–2276, Sep. 2019, doi: 10.1021/acsenergylett.9b01550.

[43] M. C. Lin *et al.*, “An ultrafast rechargeable aluminium-ion battery,” *Nature*, vol. 520, no. 7547, pp. 325–328, Apr. 2015, doi: 10.1038/nature14340.

[44] Y. Song, G. Jiang, Y. Chen, P. Zhao, and Y. Tian, “Effects of chloride ions on corrosion of ductile iron and carbon steel in soil environments,” *Sci. Rep.*, vol. 7, no. 1, pp. 1–13, Jul. 2017, doi: 10.1038/s41598-017-07245-1.

[45] F. R. McLarnon and E. J. Cairns, “The Secondary Alkaline Zinc Electrode,” *J. Electrochem. Soc.*, vol. 138, no. 2, pp. 645–656, 1991, doi: 10.1149/1.2085653.

[46] D. E. Turney *et al.*, “Rechargeable Zinc Alkaline Anodes for Long-Cycle Energy Storage,” *Chem. Mater.*, vol. 29, no. 11, pp. 4819–4832, Jun. 2017, doi: 10.1021/acs.chemmater.7b00754.

[47] V. Yufit *et al.*, “Operando Visualization and Multi-scale Tomography Studies of Dendrite Formation and Dissolution in Zinc Batteries,” *Joule*, vol. 3, no. 2, pp. 485–502, 2019, doi: 10.1016/j.joule.2018.11.002.

[48] J. Hao *et al.*, “Designing Dendrite-Free Zinc Anodes for Advanced Aqueous Zinc Batteries,” *Adv. Funct. Mater.*, vol. 30, no. 30, p. 2001263, Jul. 2020, doi: 10.1002/adfm.202001263.

[49] J. Hao, X. Li, X. Zeng, D. Li, J. Mao, and Z. Guo, “Deeply understanding the Zn anode behaviour and corresponding improvement strategies in different aqueous Zn-based batteries,” *Energy Environ. Sci.*, vol. 13, no. 11, pp. 3917–3949, 2020, doi: 10.1039/d0ee02162h.

[50] J. Zhou, L. Shan, Z. Wu, X. Guo, G. Fang, and S. Liang, “Investigation of V2O5 as a low-cost rechargeable aqueous zinc ion battery cathode,” *Chem. Commun.*, vol. 54, no. 35, pp. 4457–4460, Apr. 2018, doi: 10.1039/c8cc02250j.

[51] G. Kasiri, R. Trócoli, A. Bani Hashemi, and F. La Mantia, “An electrochemical investigation of the aging of copper hexacyanoferrate during the operation in zinc-ion batteries,” *Electrochim. Acta*, vol. 222, pp. 74–83, Dec. 2016, doi: 10.1016/j.electacta.2016.10.155.

[52] C. Zhang *et al.*, "A ZnCl2 water-in-salt electrolyte for a reversible Zn metal anode," *Chem. Commun.*, vol. 54, no. 100, pp. 14097–14099, Dec. 2018, doi: 10.1039/c8cc07730d.

[53] L. Wang *et al.*, "A Zn(ClO4)2 Electrolyte Enabling Long-Life Zinc Metal Electrodes for Rechargeable Aqueous Zinc Batteries," *ACS Appl. Mater. Interfaces*, 2019, doi: 10.1021/acsami.9b10905.

[54] N. Zhang *et al.*, "Cation-Deficient Spinel ZnMn2O4 Cathode in Zn(CF3SO3)2 Electrolyte for Rechargeable Aqueous Zn-Ion Battery," *J. Am. Chem. Soc.*, vol. 138, no. 39, pp. 12894–12901, Oct. 2016, doi: 10.1021/jacs.6b05958.

[55] L. Suo *et al.*, "Advanced High-Voltage Aqueous Lithium-Ion Battery Enabled by 'Water-in-Bisalt' Electrolyte," *Angew. Chemie - Int. Ed.*, vol. 55, no. 25, pp. 7136–7141, Jun. 2016, doi: 10.1002/anie.201602397.

[56] G. Li *et al.*, "Towards polyvalent ion batteries: A zinc-ion battery based on NASICON structured Na3V2(PO4)3," *Nano Energy*, vol. 25, pp. 211–217, Jul. 2016, doi: 10.1016/j.nanoen.2016.04.051.

[57] A. Naveed *et al.*, "A Highly Reversible Zn Anode with Intrinsically Safe Organic Electrolyte for Long-Cycle-Life Batteries," *Adv. Mater.*, vol. 31, no. 36, p. 1900668, Sep. 2019, doi: 10.1002/adma.201900668.

[58] C. Zhong *et al.*, "Decoupling electrolytes towards stable and high-energy rechargeable aqueous zinc–manganese dioxide batteries," *Nat. Energy*, vol. 5, no. 6, pp. 440–449, Mar. 2020, doi: 10.1038/s41560-020-0584-y.

[59] W. Sun *et al.*, "Zn/MnO2 Battery Chemistry with H+ and Zn2+ Coinsertion," *J. Am. Chem. Soc.*, vol. 139, no. 29, pp. 9775–9778, Jul. 2017, doi: 10.1021/jacs.7b04471.

[60] C. Wei, C. Xu, B. Li, H. Du, and F. Kang, “Preparation and characterization of manganese dioxides with nano-sized tunnel structures for zinc ion storage,” in *Journal of Physics and Chemistry of Solids*, Dec. 2012, vol. 73, no. 12, pp. 1487–1491. doi: 10.1016/j.jpcs.2011.11.038.

[61] N. Zhang *et al.*, “Rechargeable aqueous zinc-manganese dioxide batteries with high energy and power densities,” *Nat. Commun.*, vol. 8, no. 1, pp. 1–9, Sep. 2017, doi: 10.1038/s41467-017-00467-x.

[62] M. H. Alfaruqi *et al.*, “Electrochemically induced structural transformation in a γ-MnO2 cathode of a high capacity zinc-ion battery system,” *Chem. Mater.*, vol. 27, no. 10, pp. 3609–3620, May 2015, doi: 10.1021/cm504717p.

[63] B. Lee, C. S. Yoon, H. R. Lee, K. Y. Chung, B. W. Cho, and S. H. Oh, “Electrochemically-induced reversible transition from the tunneled to layered polymorphs of manganese dioxide,” *Sci. Rep.*, vol. 4, no. 1, pp. 1–8, Aug. 2014, doi: 10.1038/srep06066.

[64] B. Jiang, C. Xu, C. Wu, L. Dong, J. Li, and F. Kang, “Manganese Sesquioxide as Cathode Material for Multivalent Zinc Ion Battery with High Capacity and Long Cycle Life,” *Electrochim. Acta*, vol. 229, pp. 422–428, Mar. 2017, doi: 10.1016/j.electacta.2017.01.163.

[65] B. Zhang *et al.*, “An aqueous rechargeable battery based on zinc anode and Na0.95MnO2,” *Chem. Commun.*, vol. 50, no. 10, pp. 1209–1211, Jan. 2014, doi: 10.1039/c3cc48382g.

[66] V. Soundharrajan *et al.*, “Aqueous Magnesium Zinc Hybrid Battery: An Advanced High-Voltage and High-Energy MgMn2O4 Cathode,” *ACS Energy Lett.*, vol. 3, no. 8, pp. 1998–2004, Aug. 2018, doi: 10.1021/acsenergylett.8b01105.

[67] C. Zhu *et al.*, “Binder-free stainless steel@Mn3O4 nanoflower composite: A high-activity aqueous zinc-ion battery cathode with high-capacity and long-cycle-life,” *J. Mater. Chem. A*, vol. 6, no. 20, pp. 9677–9683, May 2018, doi: 10.1039/c8ta01198b.

[68] J. Hao *et al.*, “Electrochemically induced spinel-layered phase transition of Mn3O4 in high performance neutral aqueous rechargeable zinc battery,” *Electrochim. Acta*, vol. 259, pp. 170–178, Jan. 2018, doi: 10.1016/j.electacta.2017.10.166.

[69] N. Zhang *et al.*, “Rechargeable Aqueous Zn-V2O5 Battery with High Energy Density and Long Cycle Life,” *ACS Energy Lett.*, vol. 3, no. 6, pp. 1366–1372, Jun. 2018, doi: 10.1021/acsenergylett.8b00565.

[70] P. Hu *et al.*, “Zn/V2O5 Aqueous Hybrid-Ion Battery with High Voltage Platform and Long Cycle Life,” *ACS Appl. Mater. Interfaces*, vol. 9, no. 49, pp. 42717–42722, Dec. 2017, doi: 10.1021/acsami.7b13110.

[71] M. Yan *et al.*, “Water-Lubricated Intercalation in V2O5·nH2O for High-Capacity and High-Rate Aqueous Rechargeable Zinc Batteries,” *Adv. Mater.*, vol. 30, no. 1, p. 1703725, Jan. 2018, doi: 10.1002/adma.201703725.

[72] D. Kundu, S. Hosseini Vajargah, L. Wan, B. Adams, D. Prendergast, and L. F. Nazar, “Aqueous: Vs. nonaqueous Zn-ion batteries: Consequences of the desolvation penalty at the interface,” *Energy Environ. Sci.*, vol. 11, no. 4, pp. 881–892, Apr. 2018, doi: 10.1039/c8ee00378e.

[73] Q. Pang *et al.*, “H2V3O8 Nanowire/Graphene Electrodes for Aqueous Rechargeable Zinc Ion Batteries with High Rate Capability and Large Capacity,” *Adv. Energy Mater.*, vol. 8, no. 19, p. 1800144, Jul. 2018, doi: 10.1002/aenm.201800144.

[74] B. Sambandam *et al.*, “Aqueous rechargeable Zn-ion batteries: An imperishable and high-energy Zn2V2O7 nanowire cathode through intercalation regulation,” *J. Mater. Chem. A*, vol. 6, no. 9, pp. 3850–3856, Feb. 2018, doi: 10.1039/c7ta11237h.

[75] D. Kundu, B. D. Adams, V. Duffort, S. H. Vajargah, and L. F. Nazar, “A high-capacity and long-life aqueous rechargeable zinc battery using a metal oxide intercalation cathode,” *Nat. Energy*, vol. 1, no. 10, pp. 1–8, Aug. 2016, doi: 10.1038/nenergy.2016.119.

[76] C. Xia, J. Guo, Y. Lei, H. Liang, C. Zhao, and H. N. Alshareef, “Rechargeable Aqueous Zinc-Ion Battery Based on Porous Framework Zinc Pyrovanadate Intercalation Cathode,” *Adv. Mater.*, vol. 30, no. 5, p. 1705580, Feb. 2018, doi: 10.1002/adma.201705580.

[77] F. Wan, L. Zhang, X. Dai, X. Wang, Z. Niu, and J. Chen, “Aqueous rechargeable zinc/sodium vanadate batteries with enhanced performance from simultaneous insertion of dual carriers,” *Nat. Commun.*, vol. 9, no. 1, pp. 1–11, Dec. 2018, doi: 10.1038/s41467-018-04060-8.

[78] C. Xia, J. Guo, P. Li, X. Zhang, and H. N. Alshareef, “Highly Stable Aqueous Zinc-Ion Storage Using a Layered Calcium Vanadium Oxide Bronze Cathode,” *Angew. Chemie - Int. Ed.*, vol. 57, no. 15, pp. 3943–3948, Apr. 2018, doi: 10.1002/anie.201713291.

[79] P. Hu *et al.*, “Highly Durable Na2V6O16·1.63H2O Nanowire Cathode for Aqueous Zinc-Ion Battery,” *Nano Lett.*, vol. 18, no. 3, pp. 1758–1763, Mar. 2018, doi: 10.1021/acs.nanolett.7b04889.

[80] P. He *et al.*, “Sodium Ion Stabilized Vanadium Oxide Nanowire Cathode for High-Performance Zinc-Ion Batteries,” *Adv. Energy Mater.*, vol. 8, no. 10, p. 1702463, Apr. 2018, doi: 10.1002/aenm.201702463.

[81] X. Guo *et al.*, “Mechanistic Insights of Zn2+ Storage in Sodium Vanadates,” *Adv. Energy Mater.*, vol. 8, no. 27, p. 1801819, Sep. 2018, doi: 10.1002/aenm.201801819.

[82] B. Tang *et al.*, “Potassium vanadates with stable structure and fast ion diffusion channel as cathode for rechargeable aqueous zinc-ion batteries,” *Nano Energy*, vol. 51, pp. 579–587, Sep. 2018, doi: 10.1016/j.nanoen.2018.07.014.

[83] Z. Hou, X. Zhang, X. Li, Y. Zhu, J. Liang, and Y. Qian, “Surfactant widens the electrochemical window of an aqueous electrolyte for better rechargeable aqueous sodium/zinc battery,” *J. Mater. Chem. A*, vol. 5, no. 2, pp. 730–738, Jan. 2017, doi: 10.1039/c6ta08736a.

[84] T. Gupta *et al.*, “Improving the cycle life of a high-rate, high-potential aqueous dual-ion battery using hyper-dendritic zinc and copper hexacyanoferrate,” *J. Power Sources*, vol. 305, pp. 22–29, Feb. 2016, doi: 10.1016/j.jpowsour.2015.11.065.

[85] Z. Jia, B. Wang, and Y. Wang, “Copper hexacyanoferrate with a well-defined open framework as a positive electrode for aqueous zinc ion batteries,” *Mater. Chem. Phys.*, vol. 149, pp. 601–606, Jan. 2015, doi: 10.1016/j.matchemphys.2014.11.014.

[86] L. Zhang, L. Chen, X. Zhou, and Z. Liu, “Towards high-voltage aqueous metal-ion batteries beyond 1.5 V: The zinc/zinc hexacyanoferrate system,” *Adv. Energy Mater.*, vol. 5, no. 2, p. 1400930, Jan. 2015, doi: 10.1002/aenm.201400930.

[87] M. S. Chae, J. W. Heo, S. C. Lim, and S. T. Hong, “Electrochemical Zinc-Ion Intercalation Properties and Crystal Structures of ZnMo6S8 and Zn2Mo6S8 Chevrel Phases in Aqueous Electrolytes,” *Inorg. Chem.*, vol. 55, no. 7, pp. 3294–3301, Apr. 2016, doi: 10.1021/acs.inorgchem.5b02362.

[88] Y. Cheng *et al.*, “Highly Reversible Zinc-Ion Intercalation into Chevrel Phase Mo6S8 Nanocubes and Applications for Advanced Zinc-Ion Batteries,” *ACS Appl. Mater. Interfaces*, vol. 8, no. 22, pp. 13673–13677, Jun. 2016, doi: 10.1021/acsami.6b03197.

[89] Z. Liu, G. Pulletikurthi, and F. Endres, “A Prussian Blue/Zinc Secondary Battery with a Bio-Ionic Liquid-Water Mixture as Electrolyte,” *ACS Appl. Mater. Interfaces*, vol. 8, no. 19, pp. 12158–12164, May 2016, doi: 10.1021/acsami.6b01592.

[90] R. Trócoli and F. La Mantia, “An aqueous zinc-ion battery based on copper hexacyanoferrate,” *ChemSusChem*, vol. 8, no. 3, pp. 481–485, Feb. 2015, doi: 10.1002/cssc.201403143.

[91] W. Li, K. Wang, S. Cheng, and K. Jiang, “A long-life aqueous Zn-ion battery based on Na3V2(PO4)2F3 cathode,” *Energy Storage Mater.*, vol. 15, pp. 14–21, Nov. 2018, doi: 10.1016/j.ensm.2018.03.003.

[92] G. Li, Z. Yang, Y. Jiang, W. Zhang, and Y. Huang, “Hybrid aqueous battery based on Na3V2(PO4)3/C cathode and zinc anode for potential large-scale energy storage,” *J. Power Sources*, vol. 308, pp. 52–57, Mar. 2016, doi: 10.1016/j.jpowsour.2016.01.058.

[93] J. Zhao *et al.*, “High-voltage Zn/LiMn0.8Fe0.2PO4 aqueous rechargeable battery by virtue of ‘water-in-salt’ electrolyte,” *Electrochem. commun.*, vol. 69, pp. 6–10, Aug. 2016, doi: 10.1016/j.elecom.2016.05.014.

[94] H. B. Zhao *et al.*, “Novel rechargeable M3V2(PO4)3//Zinc (M = Li, Na) hybrid aqueous batteries with excellent cycling performance,” *Sci. Rep.*, vol. 6, no. 1, pp. 1–10, May 2016, doi: 10.1038/srep25809.

[95] G. Fang, J. Zhou, A. Pan, and S. Liang, “Recent Advances in Aqueous Zinc-Ion Batteries,” *ACS Energy Lett.*, vol. 3, no. 10, pp. 2480–2501, Oct. 2018, doi: 10.1021/acsenergylett.8b01426.

[96] L. Ma *et al.*, “Toward Practical High-Areal-Capacity Aqueous Zinc-Metal Batteries: Quantifying Hydrogen Evolution and a Solid-Ion Conductor for Stable Zinc Anodes,” *Adv. Mater.*, vol. 33, no. 12, 2021, doi: 10.1002/adma.202007406.

[97] X. Guo *et al.*, “Alleviation of Dendrite Formation on Zinc Anodes via Electrolyte Additives,” *ACS Energy Lett.*, vol. 6, no. 2, pp. 395–403, Jan. 2021, doi: 10.1021/acsenergylett.0c02371.

[98] H. He *et al.*, “Engineering interfacial layers to enable Zn metal anodes for aqueous zinc-ion batteries,” *Energy Storage Mater.*, vol. 43, no. August, pp. 317–336, 2021, doi: 10.1016/j.ensm.2021.09.012.

[99] J. Shin, J. Lee, Y. Park, and J. W. Choi, “Aqueous zinc ion batteries: Focus on zinc metal anodes,” *Chemical Science*, vol. 11, no. 8. Royal Society of Chemistry, pp. 2028–2044, Feb. 28, 2020. doi: 10.1039/d0sc00022a.

[100] J. Yang *et al.*, “Zinc Anode for Mild Aqueous Zinc-Ion Batteries: Challenges, Strategies, and Perspectives,” *Nano-Micro Letters*, vol. 14, no. 1. Springer, pp. 1–47, Jan. 03, 2022. doi: 10.1007/s40820-021-00782-5.

[101] G. Zampardi and F. La Mantia, “Open challenges and good experimental practices in the research field of aqueous Zn-ion batteries,” *Nature Communications*, vol. 13, no. 1. p. 687, Dec. 2022. doi: 10.1038/s41467-022-28381-x.

[102] L. Ma *et al.*, “Realizing high zinc reversibility in rechargeable batteries,” *Nat. Energy*, vol. 5, no. 10, pp. 743–749, Aug. 2020, doi: 10.1038/s41560-020-0674-x.

[103] V. Verma, S. Kumar, W. Manalastas, and M. Srinivasan, “Undesired Reactions in Aqueous Rechargeable Zinc Ion Batteries,” *ACS Energy Letters*, vol. 13. American Chemical Society, pp. 1773–1785, 2021. doi: 10.1021/acsenergylett.1c00393.

[104] T. K. A. Hoang, T. N. L. Doan, K. E. K. Sun, and P. Chen, “Corrosion chemistry and protection of zinc & zinc alloys by polymer-containing materials for potential use in rechargeable aqueous batteries,” *RSC Adv.*, vol. 5, no. 52, pp. 41677–41691, May 2015, doi: 10.1039/c5ra00594a.

[105] F. Wang *et al.*, “Highly reversible zinc metal anode for aqueous batteries,” *Nat. Mater.*, vol. 17, no. 6, pp. 543–549, Apr. 2018, doi: 10.1038/s41563-018-0063-z.

[106] C. Deng *et al.*, “A Sieve-Functional and Uniform-Porous Kaolin Layer toward Stable Zinc Metal Anode,” *Adv. Funct. Mater.*, vol. 30, no. 21, p. 2000599, May 2020, doi: 10.1002/adfm.202000599.

[107] C. Xie, Y. Li, Q. Wang, D. Sun, Y. Tang, and H. Wang, “Issues and solutions toward zinc anode in aqueous zinc-ion batteries: A mini review,” *Carbon Energy*, vol. 2, no. 4, pp. 540–560, 2020, doi: 10.1002/cey2.67.

[108] J. Hao *et al.*, “An In-Depth Study of Zn Metal Surface Chemistry for Advanced Aqueous Zn-Ion Batteries,” *Adv. Mater.*, vol. 32, no. 34, p. 2003021, Aug. 2020, doi: 10.1002/adma.202003021.

[109] J. Zhao *et al.*, “‘Water-in-deep eutectic solvent’ electrolytes enable zinc metal anodes for rechargeable aqueous batteries,” *Nano Energy*, vol. 57, no. 7, pp. 625–634, Jul. 2019, doi: 10.1016/j.nanoen.2018.12.086.

[110] L. Droguet, A. Grimaud, O. Fontaine, and J. M. Tarascon, “Water-in-Salt Electrolyte (WiSE) for Aqueous Batteries: A Long Way to Practicality,” *Adv. Energy Mater.*, vol. 10, no. 43, p. 2002440, Nov. 2020, doi: 10.1002/aenm.202002440.

[111] W. Manalastas, S. Kumar, V. Verma, L. Zhang, D. Yuan, and M. Srinivasan, “Water in Rechargeable Multivalent-Ion Batteries: An Electrochemical Pandora’s Box,” *ChemSusChem*, vol. 12, no. 2. John Wiley & Sons, Ltd, pp. 379–396, Jan. 24, 2019. doi: 10.1002/cssc.201801523.

[112] S. Kumar *et al.*, “Multiscalar Investigation of FeVO4 Conversion Cathode for a Low Concentration Zn(CF3SO3)2 Rechargeable Zn-Ion Aqueous Battery,” *Batter. Supercaps*, vol. 3, no. 7, pp. 619–630, Jul. 2020, doi: 10.1002/batt.202000018.

[113] Q. Yang *et al.*, “Dendrites in Zn-Based Batteries,” *Advanced Materials*, vol. 32, no. 48. John Wiley & Sons, Ltd, p. 2001854, Dec. 01, 2020. doi: 10.1002/adma.202001854.

[114] Q. Yang *et al.*, “Do Zinc Dendrites Exist in Neutral Zinc Batteries: A Developed Electrohealing Strategy to In Situ Rescue In-Service Batteries,” *Adv. Mater.*, vol. 31, no. 43, p. 1903778, Oct. 2019, doi: 10.1002/adma.201903778.

[115] H. Qiu *et al.*, “Zinc anode-compatible in-situ solid electrolyte interphase via cation solvation modulation,” *Nat. Commun.*, vol. 10, no. 1, pp. 1–12, Nov. 2019, doi: 10.1038/s41467-019-13436-3.

[116] N. Zhang *et al.*, “Ultrafast Rechargeable Zinc Battery Based on High-Voltage Graphite Cathode and Stable Nonaqueous Electrolyte,” *ACS Appl. Mater. Interfaces*, vol. 11, no. 36, pp. 32978–32986, Sep. 2019, doi: 10.1021/acsami.9b10399.

[117] X. Zhou *et al.*, “Exploring the Interfacial Chemistry between Zinc Anodes and Aqueous Electrolytes via an in Situ Visualized Characterization System,” *ACS Appl. Mater. Interfaces*, vol. 12, no. 49, pp. 55476–55482, Dec. 2020, doi: 10.1021/acsami.0c17023.

[118] D. Desai, D. E. Turney, B. Anantharaman, D. A. Steingart, and S. Banerjee, “Morphological evolution of nanocluster aggregates and single crystals in alkaline zinc electrodeposition,” *J. Phys. Chem. C*, vol. 118, no. 16, pp. 8656–8666, Apr. 2014, doi: 10.1021/jp411104a.

[119] B. D. Adams, J. Zheng, X. Ren, W. Xu, and J. G. Zhang, “Accurate Determination of Coulombic Efficiency for Lithium Metal Anodes and Lithium Metal Batteries,” *Adv. Energy Mater.*, vol. 8, no. 7, p. 1702097, Mar. 2018, doi: 10.1002/aenm.201702097.

[120] X. Ren *et al.*, “High-concentration ether electrolytes for stable high-voltage lithium metal batteries,” *ACS Energy Lett.*, vol. 4, no. 4, pp. 896–902, Apr. 2019, doi: 10.1021/acsenergylett.9b00381.

[121] J. Qian *et al.*, “High rate and stable cycling of lithium metal anode,” *Nat. Commun.*, vol. 6, no. 1, pp. 1–9, Feb. 2015, doi: 10.1038/ncomms7362.

[122] X. Wu *et al.*, “Reverse Dual-Ion Battery via a ZnCl2 Water-in-Salt Electrolyte,” *J. Am. Chem. Soc.*, vol. 141, no. 15, pp. 6338–6344, Apr. 2019, doi: 10.1021/jacs.9b00617.

[123] Z. Hou *et al.*, “A High-Energy and Long-Life Aqueous Zn/Birnessite Battery via Reversible Water and Zn2+ Coinsertion,” *Small*, vol. 16, no. 26, p. 2001228, Jul. 2020, doi: 10.1002/smll.202001228.

[124] J. Hao *et al.*, “Toward High-Performance Hybrid Zn-Based Batteries via Deeply Understanding Their Mechanism and Using Electrolyte Additive,” *Adv. Funct. Mater.*, vol. 29, no. 34, p. 1903605, Aug. 2019, doi: 10.1002/adfm.201903605.

[125] A. Mitha, A. Z. Yazdi, M. Ahmed, and P. Chen, “Surface Adsorption of Polyethylene Glycol to Suppress Dendrite Formation on Zinc Anodes in Rechargeable Aqueous Batteries,” *ChemElectroChem*, vol. 5, no. 17, pp. 2409–2418, Sep. 2018, doi: 10.1002/celc.201800572.

[126] K. E. K. Sun *et al.*, “Suppression of Dendrite Formation and Corrosion on Zinc Anode of Secondary Aqueous Batteries,” *ACS Appl. Mater. Interfaces*, vol. 9, no. 11, pp. 9681–9687, Mar. 2017, doi: 10.1021/acsami.6b16560.

[127] W. Xu *et al.*, "Diethyl ether as self-healing electrolyte additive enabled long-life rechargeable aqueous zinc ion batteries," *Nano Energy*, vol. 62, pp. 275–281, Aug. 2019, doi: 10.1016/j.nanoen.2019.05.042.

[128] K. E. K. Sun, T. K. A. Hoang, T. N. L. Doan, Y. Yu, and P. Chen, "Highly Sustainable Zinc Anodes for a Rechargeable Hybrid Aqueous Battery," *Chem. - A Eur. J.*, vol. 24, no. 7, pp. 1667–1673, Feb. 2018, doi: 10.1002/chem.201704440.

[129] Y. Tang *et al.*, "Ion-confinement effect enabled by gel electrolyte for highly reversible dendrite-free zinc metal anode," *Energy Storage Mater.*, vol. 27, pp. 109–116, May 2020, doi: 10.1016/j.ensm.2020.01.023.

[130] X. Li *et al.*, "Interfacing MXene flakes on fiber fabric as an ultrafast electron transport layer for high performance textile electrodes," *Energy Storage Mater.*, vol. 33, pp. 62–70, Dec. 2020, doi: 10.1016/j.ensm.2020.05.004.

[131] D. Chao *et al.*, "A High-Rate and Stable Quasi-Solid-State Zinc-Ion Battery with Novel 2D Layered Zinc Orthovanadate Array," *Adv. Mater.*, vol. 30, no. 32, p. 1803181, Aug. 2018, doi: 10.1002/adma.201803181.

[132] H. Li *et al.*, "Waterproof and Tailorable Elastic Rechargeable Yarn Zinc Ion Batteries by a Cross-Linked Polyacrylamide Electrolyte," *ACS Nano*, vol. 12, no. 4, pp. 3140–3148, Apr. 2018, doi: 10.1021/acsnano.7b09003.

[133] D. Wang *et al.*, "A Nanofibrillated Cellulose/Polyacrylamide Electrolyte-Based Flexible and Sewable High-Performance Zn–MnO2 Battery with Superior Shear Resistance," *Small*, vol. 14, no. 51, p. 1803978, Dec. 2018, doi: 10.1002/smll.201803978.

[134] H. Li *et al.*, “An extremely safe and wearable solid-state zinc ion battery based on a hierarchical structured polymer electrolyte,” *Energy Environ. Sci.*, vol. 11, no. 4, pp. 941–951, Apr. 2018, doi: 10.1039/c7ee03232c.

[135] Z. Zhao *et al.*, “Long-life and deeply rechargeable aqueous Zn anodes enabled by a multifunctional brightener-inspired interphase,” *Energy Environ. Sci.*, vol. 12, no. 6, pp. 1938–1949, Jun. 2019, doi: 10.1039/c9ee00596j.

[136] C. Shen *et al.*, “Graphene-Boosted, High-Performance Aqueous Zn-Ion Battery,” *ACS Appl. Mater. Interfaces*, vol. 10, no. 30, pp. 25446–25453, Aug. 2018, doi: 10.1021/ACSAMI.8B07781/ASSET/IMAGES/LARGE/AM-2018-07781S_0006.JPEG.

[137] W. Li, K. Wang, M. Zhou, H. Zhan, S. Cheng, and K. Jiang, “Advanced Low-Cost, High-Voltage, Long-Life Aqueous Hybrid Sodium/Zinc Batteries Enabled by a Dendrite-Free Zinc Anode and Concentrated Electrolyte,” *ACS Appl. Mater. Interfaces*, vol. 10, no. 26, pp. 22059–22066, Jul. 2018, doi: 10.1021/ACSAMI.8B04085/ASSET/IMAGES/LARGE/AM-2018-04085R_0006.JPEG.

[138] L. Kang *et al.*, “Nanoporous CaCO3 Coatings Enabled Uniform Zn Stripping/Plating for Long-Life Zinc Rechargeable Aqueous Batteries,” *Adv. Energy Mater.*, vol. 8, no. 25, p. 1801090, Sep. 2018, doi: 10.1002/aenm.201801090.

[139] P. Liang *et al.*, “Highly Reversible Zn Anode Enabled by Controllable Formation of Nucleation Sites for Zn-Based Batteries,” *Adv. Funct. Mater.*, vol. 30, no. 13, p. 1908528, Mar. 2020, doi: 10.1002/adfm.201908528.

[140] K. Zhao *et al.*, “Ultrathin Surface Coating Enables Stabilized Zinc Metal Anode,” *Adv. Mater. Interfaces*, vol. 5, no. 16, p. 1800848, Aug. 2018, doi: 10.1002/admi.201800848.

[141] X. Xie *et al.*, “Manipulating the ion-transfer kinetics and interface stability for high-performance zinc metal anodes,” *Energy Environ. Sci.*, vol. 13, no. 2, pp. 503–510, Feb. 2020, doi: 10.1039/c9ee03545a.

[142] Y. Cheng, X. Xi, D. Li, X. Li, Q. Lai, and H. Zhang, “Performance and potential problems of high power density zinc-nickel single flow batteries,” *RSC Adv.*, vol. 5, no. 3, pp. 1772–1776, Dec. 2015, doi: 10.1039/c4ra12812e.

[143] M. Bockelmann, U. Kunz, and T. Turek, “Electrically rechargeable zinc-oxygen flow battery with high power density,” *Electrochem. commun.*, vol. 69, pp. 24–27, Aug. 2016, doi: 10.1016/j.elecom.2016.05.013.

[144] Y. Zeng *et al.*, “Dendrite-Free Zinc Deposition Induced by Multifunctional CNT Frameworks for Stable Flexible Zn-Ion Batteries,” *Adv. Mater.*, vol. 31, no. 36, p. 1903675, Sep. 2019, doi: 10.1002/adma.201903675.

[145] W. Dong, J. L. Shi, T. S. Wang, Y. X. Yin, C. R. Wang, and Y. G. Guo, “3D zinc@carbon fiber composite framework anode for aqueous Zn-MnO2 batteries,” *RSC Adv.*, vol. 8, no. 34, pp. 19157–19163, May 2018, doi: 10.1039/c8ra03226b.

[146] Y. Zeng *et al.*, “Achieving Ultrahigh Energy Density and Long Durability in a Flexible Rechargeable Quasi-Solid-State Zn–MnO2 Battery,” *Adv. Mater.*, vol. 29, no. 26, p. 1700274, Jul. 2017, doi: 10.1002/adma.201700274.

[147] X. Jia, C. Liu, Z. G. Neale, J. Yang, and G. Cao, “Active Materials for Aqueous Zinc Ion Batteries: Synthesis, Crystal Structure, Morphology, and Electrochemistry,” *Chemical Reviews*, vol. 120, no. 15. American Chemical Society, pp. 7795–7866, Aug. 12, 2020. doi: 10.1021/acs.chemrev.9b00628.

[148] J. Zheng *et al.*, “Reversible epitaxial electrodeposition of metals in battery anodes,” *Science (80-.).*, vol. 366, no. 6465, pp. 645–648, Nov. 2019, doi: 10.1126/science.aax6873.

[149] T. Foroozan, V. Yurkiv, S. Sharifi-Asl, R. Rojaee, F. Mashayek, and R. Shahbazian-Yassar, “Non-Dendritic Zn Electrodeposition Enabled by Zincophilic Graphene Substrates,” *ACS Appl. Mater. Interfaces*, 2019, doi: 10.1021/acsami.9b13174.

[150] S. Li *et al.*, “Toward Planar and Dendrite-Free Zn Electrodepositions by Regulating Sn-Crystal Textured Surface,” *Adv. Mater.*, vol. 33, no. 21, p. 2008424, May 2021, doi: 10.1002/adma.202008424.

[151] J. Cao *et al.*, “Manipulating Crystallographic Orientation of Zinc Deposition for Dendrite-free Zinc Ion Batteries,” *Adv. Energy Mater.*, vol. 11, no. 29, p. 2101299, Aug. 2021, doi: 10.1002/aenm.202101299.

[152] R. J. Gummow, G. Vamvounis, M. B. Kannan, and Y. He, “Calcium-Ion Batteries: Current State-of-the-Art and Future Perspectives,” *Advanced Materials*, vol. 30, no. 39. John Wiley & Sons, Ltd, p. 1801702, Sep. 01, 2018. doi: 10.1002/adma.201801702.

[153] M. E. Arroyo-De Dompablo, A. Ponrouch, P. Johansson, and M. R. Palacín, “Achievements, Challenges, and Prospects of Calcium Batteries,” *Chemical Reviews*. American Chemical Society, 2019. doi: 10.1021/acs.chemrev.9b00339.

[154] B. Ji, H. He, W. Yao, and Y. Tang, “Recent Advances and Perspectives on Calcium-Ion Storage: Key Materials and Devices,” *Advanced Materials*, vol. 33, no. 2. John Wiley & Sons, Ltd, p. 2005501, Jan. 01, 2021. doi: 10.1002/adma.202005501.

[155] S. M. Selis, J. P. Wondowski, and R. F. Justus, “A High-Rate, High-Energy Thermal Battery System,” *J. Electrochem. Soc.*, vol. 111, no. 1, p. 6, Jan. 1964, doi: 10.1149/1.2426065.

[156] R. P. Clark and K. R. Grothaus, “An Improved Calcium Anode for Thermal Batteries,” *J. Electrochem. Soc.*, vol. 118, no. 10, p. 1680, Oct. 1971, doi: 10.1149/1.2407811.

[157] M. H. Miles, D. A. Fine, and A. N. Fletcher, “The Calcium Anode in Molten Nitrate Electrolytes,” *J. Electrochem. Soc.*, vol. 125, no. 8, pp. 1209–1214, Aug. 1978, doi: 10.1149/1.2131651.

[158] J. Schoonman and A. Wolfert, “Alloy-Anodes in Fluoride Solid-State Batteries,” *J. Electrochem. Soc.*, vol. 128, no. 7, pp. 1522–1523, Jul. 1981, doi: 10.1149/1.2127674/XML.

[159] G. E. McManis, M. H. Miles, and A. N. Fletcher, “Performance and Discharge Characteristics of Ca / LiCl , LiNO3 / LiNO3, AgNO3 / Ni Thermal Battery Cells,” *J. Electrochem. Soc.*, vol. 131, no. 2, pp. 283–286, Feb. 1984, doi: 10.1149/1.2115563.

[160] A. F. Sammells, B. Schumacher, R. L. Cook, and S. K. Schmidt, “CALCIUM SOLID ELECTROLYTE HIGH TEMPERATURE BATTERY.,” in *Electrochemical Society Extended Abstracts*, Jan. 1985, vol. 85–2, no. 1, p. 59. doi: 10.1149/1.2108533/XML.

[161] R. J. Staniewicz, “A Study of the Calcium-Thionyl Chloride Electrochemical System,” *J. Electrochem. Soc.*, vol. 127, no. 4, pp. 782–789, Apr. 1980, doi: 10.1149/1.2129758.

[162] E. Peled, A. Meitav, and M. Brand, “Calcium Thionyl Chloride High-Rate Reserve Cell,” *J. Electrochem. Soc.*, vol. 128, no. 9, pp. 1936–1938, Sep. 1981, doi: 10.1149/1.2127768.

[163] A. Meitav and E. Peled, “Calcium - Ca (AlCl4) 2 - Thionyl Chloride Cell: Performance and Safety,” *J. Electrochem. Soc.*, vol. 129, no. 3, pp. 451–457, Mar. 1982, doi: 10.1149/1.2123879.

[164] E. Peled, E. Elster, R. Tulman, and J. Kimel, “Calcium/Ca(AlCl4)2-thionyl chloride (TC) cell. Effect of temperature and cell parameters on performance,” *J. Power Sources*, vol. 14, no. 1–3, pp. 93–98, Jan. 1985, doi: 10.1016/0378-7753(85)88017-4.

[165] A. Meitav and E. Peled, “Solid electrolyte interphase (SEI) electrode-V. the formation and properties of the solid electrolyte interphase on calcium in thionyl chloride solutions,” *Electrochim. Acta*, vol. 33, no. 8, pp. 1111–1121, Aug. 1988, doi: 10.1016/0013-4686(88)80202-0.

[166] W. L. Wade, C. W. Walker, and M. Binder, “Performance of calcium/thionyl chloride cells containing Sr(AlCl4)2 electrolyte,” *J. Power Sources*, vol. 28, no. 3, pp. 295–300, Jan. 1989, doi: 10.1016/0378-7753(89)80057-6.

[167] M. Binder, W. Wade, and S. Gilman, “CALCIUM-SULFURYL CHLORIDE PRIMARY CELL.,” in *Proceedings of the Power Sources Symposium*, Apr. 1982, vol. 129, no. 4, pp. 154–156. doi: 10.1149/1.2123998.

[168] E. Elster, R. Cohen, and E. Peled, “Solid electrolyte interphase (SEI) electrodes part VII. The electrochemical behaviour of calcium in Ba(AlCl4)2 and Sr(AlCl4)2thionyl chloride solutions (extended abstract),” *J. Power Sources*, vol. 26, no. 3–4, pp. 423–425, May 1989, doi: 10.1016/0378-7753(89)80157-0.

[169] D. Aurbach, R. Skaletsky, and Y. Gofer, “The Electrochemical Behavior of Calcium Electrodes in a Few Organic Electrolytes,” *J. Electrochem. Soc.*, vol. 138, no. 12, pp. 3536–3545, 1991, doi: 10.1149/1.2085455.

[170] J. Young and M. Smeu, “Ethylene Carbonate-Based Electrolyte Decomposition and Solid-Electrolyte Interphase Formation on Ca Metal Anodes,” *J. Phys. Chem. Lett.*, vol. 9, no. 12, pp. 3295–3300, Jun. 2018, doi: 10.1021/acs.jpclett.8b01261.

[171] K. Ta, R. Zhang, M. Shin, R. T. Rooney, E. K. Neumann, and A. A. Gewirth, “Understanding Ca Electrodeposition and Speciation Processes in Nonaqueous Electrolytes for Next-Generation Ca-

Ion Batteries," *ACS Appl. Mater. Interfaces*, vol. 11, no. 24, pp. 21536–21542, Jun. 2019, doi: 10.1021/acsami.9b04926.

[172] S. D. Pu *et al.*, "Current-Density-Dependent Electroplating in Ca Electrolytes: From Globules to Dendrites," *ACS Energy Lett.*, vol. 5, no. 7, pp. 2283–2290, Jul. 2020, doi: 10.1021/acsenergylett.0c01153.

[173] Y. Jie *et al.*, "Electrolyte Solvation Manipulation Enables Unprecedented Room-Temperature Calcium-Metal Batteries," *Angew. Chemie - Int. Ed.*, vol. 59, no. 31, pp. 12689–12693, Jul. 2020, doi: 10.1002/anie.202002274.

[174] J. Forero-Saboya, C. Davoisne, R. Dedryvère, I. Yousef, P. Canepa, and A. Ponrouch, "Understanding the nature of the passivation layer enabling reversible calcium plating," *Energy Environ. Sci.*, vol. 13, no. 10, pp. 3423–3431, Oct. 2020, doi: 10.1039/d0ee02347g.

[175] K. V. Nielson, J. Luo, and T. L. Liu, "Optimizing Calcium Electrolytes by Solvent Manipulation for Calcium Batteries," *Batter. Supercaps*, vol. 3, no. 8, pp. 766–772, Aug. 2020, doi: 10.1002/batt.202000005.

[176] H. Song, J. Su, and C. Wang, "Hybrid Solid Electrolyte Interphases Enabled Ultralong Life Ca–Metal Batteries Working at Room Temperature," *Adv. Mater.*, vol. 33, no. 2, p. 2006141, Jan. 2020, doi: 10.1002/adma.202006141.

[177] H. Song and C. Wang, "Artificial Hybrid Solid Electrolyte-Mediated Ca Metal for Ultradurable Room Temperature 5 V Calcium Batteries," *ENERGY Environ. Mater.*, Mar. 2022, doi: 10.1002/eem2.12325.

[178] T. T. Tran and M. N. Obrovac, "Alloy Negative Electrodes for High Energy Density Metal-Ion Cells," *J. Electrochem. Soc.*, vol. 158, no. 12, p. A1411, Nov. 2011, doi: 10.1149/2.083112jes.

[179] Z. Yao, V. I. Hegde, A. Aspuru-Guzik, and C. Wolverton, “Discovery of Calcium-Metal Alloy Anodes for Reversible Ca-Ion Batteries,” *Adv. Energy Mater.*, vol. 9, no. 9, p. 1802994, Mar. 2019, doi: 10.1002/aenm.201802994.

[180] A. Ponrouch, D. Tchitchekova, C. Frontera, F. Bardé, M. E. A. De Dompablo, and M. R. Palacín, “Assessing Si-based anodes for Ca-ion batteries: Electrochemical decalciation of CaSi2,” *Electrochem. commun.*, vol. 66, pp. 75–78, May 2016, doi: 10.1016/j.elecom.2016.03.004.

[181] A. L. Lipson, B. Pan, S. H. Lapidus, C. Liao, J. T. Vaughey, and B. J. Ingram, “Rechargeable Ca-Ion Batteries: A New Energy Storage System,” *Chem. Mater.*, vol. 27, no. 24, pp. 8442–8447, Dec. 2015, doi: 10.1021/acs.chemmater.5b04027.

[182] M. Wang, C. Jiang, S. Zhang, X. Song, Y. Tang, and H. M. Cheng, “Reversible calcium alloying enables a practical room-temperature rechargeable calcium-ion battery with a high discharge voltage,” *Nat. Chem.*, vol. 10, no. 6, pp. 667–672, Apr. 2018, doi: 10.1038/s41557-018-0045-4.

[183] N. Wu *et al.*, “A Calcium-Ion Hybrid Energy Storage Device with High Capacity and Long Cycling Life under Room Temperature,” *Adv. Energy Mater.*, vol. 9, no. 16, p. 1803865, Apr. 2019, doi: 10.1002/aenm.201803865.

[184] B. Mortazavi, A. Dianat, O. Rahaman, G. Cuniberti, and T. Rabczuk, “Borophene as an anode material for Ca, Mg, Na or Li ion storage: A first-principle study,” *J. Power Sources*, vol. 329, pp. 456–461, Oct. 2016, doi: 10.1016/j.jpowsour.2016.08.109.

[185] H. Ishikawa, H. Higuchi, and M. Kawaguchi, “Intercalation of calcium into a graphite-like layered material,” *Chem. Lett.*, vol. 47, no. 7, pp. 891–893, May 2018, doi: 10.1246/cl.180236.

[186] A. H. Farokh Niaei, T. Hussain, M. Hankel, and D. J. Searles, “Hydrogenated defective graphene as an anode material for sodium and calcium ion batteries: A density functional theory study,” *Carbon N. Y.*, vol. 136, pp. 73–84, Sep. 2018, doi: 10.1016/j.carbon.2018.04.034.

[187] J. Park *et al.*, “Stable and High-Power Calcium-Ion Batteries Enabled by Calcium Intercalation into Graphite,” *Adv. Mater.*, vol. 32, no. 4, p. 1904411, Jan. 2020, doi: 10.1002/adma.201904411.

[188] X. Deng, X. Chen, Y. Huang, B. Xiao, and H. Du, “Two-Dimensional GeP 3 as a High Capacity Anode Material for Non-Lithium-Ion Batteries,” *J. Phys. Chem. C*, vol. 123, no. 8, pp. 4721–4728, Feb. 2019, doi: 10.1021/acs.jpcc.8b11574.

[189] D. Er, J. Li, M. Naguib, Y. Gogotsi, and V. B. Shenoy, “Ti3C2 MXene as a high capacity electrode material for metal (Li, Na, K, Ca) ion batteries,” *ACS Appl. Mater. Interfaces*, vol. 6, no. 14, pp. 11173–11179, Jul. 2014, doi: 10.1021/am501144q.

[190] Y. Xie *et al.*, “Prediction and characterization of mxene nanosheet anodes for non-lithium-ion batteries,” *ACS Nano*, vol. 8, no. 9, pp. 9606–9615, Sep. 2014, doi: 10.1021/nn503921j.

[191] M. Liu *et al.*, “Spinel compounds as multivalent battery cathodes: A systematic evaluation based on ab initio calculations,” *Energy Environ. Sci.*, vol. 8, no. 3, pp. 964–974, Mar. 2015, doi: 10.1039/c4ee03389b.

[192] Z. Rong *et al.*, “Materials Design Rules for Multivalent Ion Mobility in Intercalation Structures,” *Chem. Mater.*, vol. 27, no. 17, pp. 6016–6021, Sep. 2015, doi: 10.1021/acs.chemmater.5b02342.

[193] A. Torres, J. L. Casals, and M. E. Arroyo-De Dompablo, “Enlisting Potential Cathode Materials for Rechargeable Ca Batteries,” *Chem. Mater.*, vol. 33, no. 7, pp. 2488–2497, Apr. 2021, doi: 10.1021/acs.chemmater.0c04741.

[194] M. Hayashi, H. Arai, H. Ohtsuka, and Y. Sakurai, “Electrochemical characteristics of calcium in organic electrolyte solutions and vanadium oxides as calcium hosts,” in *Journal of Power Sources*, Jun. 2003, vol. 119–121, pp. 617–620. doi: 10.1016/S0378-7753(03)00307-0.

[195] M. Hayashi, H. Arai, H. Ohtsuka, and Y. Sakurai, “Electrochemical insertion/extraction of calcium ions using crystalline vanadium oxide,” *Electrochem. Solid-State Lett.*, vol. 7, no. 5, 2004, doi: 10.1149/1.1675951.

[196] M. Bervas, L. C. Klein, and G. G. Amatucci, “Vanadium oxide-propylene carbonate composite as a host for the intercalation of polyvalent cations,” *Solid State Ionics*, vol. 176, no. 37–38, pp. 2735–2747, Nov. 2005, doi: 10.1016/j.ssi.2005.09.009.

[197] M. Cabello *et al.*, “Advancing towards a veritable calcium-ion battery: CaCo2O4 positive electrode material,” *Electrochem. commun.*, vol. 67, pp. 59–64, Jun. 2016, doi: 10.1016/j.elecom.2016.03.016.

[198] D. S. Tchitchekova, C. Frontera, A. Ponrouch, C. Krich, F. Bardé, and M. R. Palacín, “Electrochemical calcium extraction from 1D-Ca3Co2O6,” *Dalt. Trans.*, vol. 47, no. 33, pp. 11298–11302, Aug. 2018, doi: 10.1039/c8dt01754a.

[199] M. Cabello, F. Nacimiento, R. Alcántara, P. Lavela, C. Pérez Vicente, and J. L. Tirado, “Applicability of Molybdite as an Electrode Material in Calcium Batteries: A Structural Study of Layer-type CaxMoO3,” *Chem. Mater.*, vol. 30, no. 17, pp. 5853–5861, Sep. 2018, doi: 10.1021/acs.chemmater.8b01116.

[200] T. N. Vo, H. Kim, J. Hur, W. Choi, and I. T. Kim, “Surfactant-assisted ammonium vanadium oxide as a superior cathode for calcium-ion batteries,” *J. Mater. Chem. A*, vol. 6, no. 45, pp. 22645–22654, Nov. 2018, doi: 10.1039/c8ta07831a.

[201] X. Xu *et al.*, “Bilayered Mg0.25V2O5·H2O as a Stable Cathode for Rechargeable Ca-Ion Batteries,” *ACS Energy Lett.*, vol. 4, no. 6, pp. 1328–1335, Jun. 2019, doi: 10.1021/acsenergylett.9b00830.

[202] M. S. Chae, H. H. Kwak, and S. T. Hong, “Calcium Molybdenum Bronze as a Stable High-Capacity Cathode Material for Calcium-Ion Batteries,” *ACS Appl. Energy Mater.*, vol. 3, no. 6, pp. 5107–5112, Jun. 2020, doi: 10.1021/acsaem.0c00567.

[203] A. L. Lipson, S. Kim, B. Pan, C. Liao, T. T. Fister, and B. J. Ingram, “Calcium intercalation into layered fluorinated sodium iron phosphate,” *J. Power Sources*, vol. 369, pp. 133–137, Nov. 2017, doi: 10.1016/j.jpowsour.2017.09.081.

[204] B. Jeon, J. W. Heo, J. Hyoung, H. H. Kwak, D. M. Lee, and S. T. Hong, “Reversible calcium-ion insertion in NaSICON-type NaV2(PO4)3,” *Chem. Mater.*, vol. 32, no. 20, pp. 8772–8780, Oct. 2020, doi: 10.1021/ACS.CHEMMATER.0C01112/ASSET/IMAGES/LARGE/CM0C01112_0006.JPEG.

[205] S. Kim *et al.*, “High-Voltage Phosphate Cathodes for Rechargeable Ca-Ion Batteries,” *ACS Energy Lett.*, vol. 5, no. 10, pp. 3203–3211, Oct. 2020, doi: 10.1021/acsenergylett.0c01663.

[206] Z. L. Xu *et al.*, “A new high-voltage calcium intercalation host for ultra-stable and high-power calcium rechargeable batteries,” *Nat. Commun.*, vol. 12, no. 1, pp. 1–9, Jun. 2021, doi: 10.1038/s41467-021-23703-x.

[207] D. S. Tchitchekova *et al.*, “Electrochemical Intercalation of Calcium and Magnesium in TiS2: Fundamental Studies Related to Multivalent Battery Applications,” *Chem. Mater.*, vol. 30, no. 3, pp. 847–856, Feb. 2018, doi: 10.1021/acs.chemmater.7b04406.

[208] W. Ren, F. Xiong, Y. Fan, Y. Xiong, and Z. Jian, “Hierarchical Copper Sulfide Porous Nanocages for Rechargeable Multivalent-Ion Batteries,” *ACS Appl. Mater. Interfaces*, vol. 12, no. 9, pp. 10471–10478, Mar. 2020, doi: 10.1021/acsami.9b21999.

[209] A. L. Lipson *et al.*, “Nickel hexacyanoferrate, a versatile intercalation host for divalent ions from nonaqueous electrolytes,” *J. Power Sources*, vol. 325, pp. 646–652, Sep. 2016, doi: 10.1016/j.jpowsour.2016.06.019.

[210] P. Padigi, N. Kuperman, J. Thiebes, G. Goncher, D. Evans, and R. Solanki, “Calcium cobalt hexacyanoferrate cathodes for rechargeable divalent ion batteries,” *J. New Mater. Electrochem. Syst.*, vol. 19, no. 2, pp. 57–64, 2016, doi: 10.14447/jnmes.v19i2.231.

[211] T. Tojo, Y. Sugiura, R. Inada, and Y. Sakurai, “Reversible Calcium Ion Batteries Using a Dehydrated Prussian Blue Analogue Cathode,” *Electrochim. Acta*, vol. 207, pp. 22–27, Jul. 2016, doi: 10.1016/j.electacta.2016.04.159.

[212] N. Kuperman, P. Padigi, G. Goncher, D. Evans, J. Thiebes, and R. Solanki, “High performance Prussian Blue cathode for nonaqueous Ca-ion intercalation battery,” *J. Power Sources*, vol. 342, pp. 414–418, Feb. 2017, doi: 10.1016/j.jpowsour.2016.12.074.

[213] T. N. Vo, J. Hur, and I. T. Kim, “Enabling High Performance Calcium-Ion Batteries from Prussian Blue and Metal-Organic Compound Materials,” *ACS Sustain. Chem. Eng.*, vol. 8, no. 7, pp. 2596–2601, Feb. 2020, doi: 10.1021/acssuschemeng.9b07374.

[214] J. Rogosic, “Towards the Development of Ca Ion Batteries,” 2014. Accessed: Jul. 27, 2022. [Online]. Available: https://dspace.mit.edu/handle/1721.1/89961

[215] J. Bitenc *et al.*, “Electrochemical Performance and Mechanism of Calcium Metal-Organic Battery,” *Batter. Supercaps*, vol. 4, no. 1, pp. 214–220, Jan. 2021, doi: 10.1002/batt.202000197.

[216] M. S. Chae, A. Nimkar, N. Shpigel, Y. Gofer, and D. Aurbach, “High Performance Aqueous and Nonaqueous Ca-Ion Cathodes Based on Fused-Ring Aromatic Carbonyl Compounds,” *ACS Energy Lett.*, vol. 6, no. 8, pp. 2659–2665, Aug. 2021, doi: 10.1021/acsenergylett.1c01010.

[217] K. A. See, J. A. Gerbec, Y. S. Jun, F. Wudl, G. D. Stucky, and R. Seshadri, “A high capacity calcium primary cell based on the Ca-S system,” *Adv. Energy Mater.*, vol. 3, no. 8, pp. 1056–1061, Aug. 2013, doi: 10.1002/aenm.201300160.

[218] X. Tang *et al.*, “A universal strategy towards high–energy aqueous multivalent–ion batteries,” *Nat. Commun. 2021 121*, vol. 12, no. 1, pp. 1–11, May 2021, doi: 10.1038/s41467-021-23209-6.

[219] X. Yu, M. J. Boyer, G. S. Hwang, and A. Manthiram, “Toward a Reversible Calcium-Sulfur Battery with a Lithium-Ion Mediation Approach,” *Adv. Energy Mater.*, vol. 9, no. 14, p. 1803794, Apr. 2019, doi: 10.1002/aenm.201803794.

[220] Z. Li, B. P. Vinayan, T. Diemant, R. J. Behm, M. Fichtner, and Z. Zhao-Karger, “Rechargeable Calcium–Sulfur Batteries Enabled by an Efficient Borate-Based Electrolyte,” *Small*, vol. 16, no. 39, p. 2001806, Oct. 2020, doi: 10.1002/smll.202001806.

[221] A. Scafuri *et al.*, “Spectroscopic Insights into the Electrochemical Mechanism of Rechargeable Calcium/Sulfur Batteries,” *Chem. Mater.*, vol. 32, no. 19, pp. 8266–8275, Oct. 2020, doi: 10.1021/acs.chemmater.0c02074.

[222] P. Reinsberg, C. J. Bondue, and H. Baltruschat, “Calcium-oxygen batteries as a promising alternative to sodium-oxygen batteries,” *J. Phys. Chem. C*, vol. 120, no. 39, pp. 22179–22185, Oct. 2016, doi: 10.1021/acs.jpcc.6b06674.

[223] T. Shiga, Y. Kato, and Y. Hase, “Coupling of nitroxyl radical as an electrochemical charging catalyst and ionic liquid for calcium plating/stripping toward a rechargeable calcium-oxygen battery,” *J. Mater. Chem. A*, vol. 5, no. 25, pp. 13212–13219, Jun. 2017, doi: 10.1039/c7ta03422a.

[224] H. Kim, D. A. Boysen, T. Ouchi, and D. R. Sadoway, “Calcium-bismuth electrodes for large-scale energy storage (liquid metal batteries),” *J. Power Sources*, vol. 241, pp. 239–248, Nov. 2013, doi: 10.1016/j.jpowsour.2013.04.052.

[225] T. Ouchi, H. Kim, X. Ning, and D. R. Sadoway, “Calcium-Antimony Alloys as Electrodes for Liquid Metal Batteries,” *J. Electrochem. Soc.*, vol. 161, no. 12, pp. A1898–A1904, Sep. 2014, doi: 10.1149/2.0801412jes.

[226] T. Ouchi, H. Kim, B. L. Spatocco, and D. R. Sadoway, “Calcium-based multi-element chemistry for grid-scale electrochemical energy storage,” *Nat. Commun.*, vol. 7, no. 1, pp. 1–5, Mar. 2016, doi: 10.1038/ncomms10999.

[227] F. S. Genier, C. V. Burdin, S. Biria, and I. D. Hosein, “A novel calcium-ion solid polymer electrolyte based on crosslinked poly(ethylene glycol) diacrylate,” *J. Power Sources*, vol. 414, pp. 302–307, Feb. 2019, doi: 10.1016/j.jpowsour.2019.01.017.

[228] X. Tang *et al.*, “A universal strategy towards high–energy aqueous multivalent–ion batteries,” *Nat. Commun.*, vol. 12, no. 1, pp. 1–11, May 2021, doi: 10.1038/s41467-021-23209-6.

[229] Z. Lu and F. Ciucci, “Metal Borohydrides as Electrolytes for Solid-State Li, Na, Mg, and Ca Batteries: A First-Principles Study,” *Chem. Mater.*, vol. 29, no. 21, pp. 9308–9319, Nov. 2017, doi: 10.1021/acs.chemmater.7b03284.

[230] R. Y. Wang, C. D. Wessells, R. A. Huggins, and Y. Cui, “Highly reversible open framework nanoscale electrodes for divalent ion batteries,” *Nano Lett.*, vol. 13, no. 11, pp. 5748–5752, Nov. 2013, doi: 10.1021/nl403669a.

[231] S. Gheytani *et al.*, “An Aqueous Ca-Ion Battery,” *Adv. Sci.*, vol. 4, no. 12, p. 1700465, Dec. 2017, doi: 10.1002/advs.201700465.

[232] J. Hyoung, J. W. Heo, and S. T. Hong, “Investigation of electrochemical calcium-ion energy storage mechanism in potassium birnessite,” *J. Power Sources*, vol. 390, pp. 127–133, Jun. 2018, doi: 10.1016/j.jpowsour.2018.04.050.

[233] C. H. Lee and S. K. Jeong, “A novel superconcentrated aqueous electrolyte to improve the electrochemical performance of calcium-ion batteries,” *Chem. Lett.*, vol. 45, no. 12, pp. 1447–1449, 2016, doi: 10.1246/cl.160769.

[234] C. Lee and S. K. Jeong, “Modulating the hydration number of calcium ions by varying the electrolyte concentration: Electrochemical performance in a Prussian blue electrode/aqueous electrolyte system for calcium-ion batteries,” *Electrochim. Acta*, vol. 265, pp. 430–436, Mar. 2018, doi: 10.1016/j.electacta.2018.01.172.

[235] I. A. Rodríguez-Pérez *et al.*, “Mg-Ion Battery Electrode: An Organic Solid’s Herringbone Structure Squeezed upon Mg-Ion Insertion,” *J. Am. Chem. Soc.*, vol. 139, no. 37, pp. 13031–13037, Sep. 2017, doi: 10.1021/jacs.7b06313.

[236] T. Shiga, H. Kondo, Y. Kato, and M. Inoue, “Insertion of Calcium Ion into Prussian Blue Analogue in Nonaqueous Solutions and Its Application to a Rechargeable Battery with Dual Carriers,” *J. Phys. Chem. C*, vol. 119, no. 50, pp. 27946–27953, Nov. 2015, doi: 10.1021/acs.jpcc.5b10245.

[237] R. Dugas, J. D. Forero-Saboya, and A. Ponrouch, “Methods and Protocols for Reliable Electrochemical Testing in Post-Li Batteries (Na, K, Mg, and Ca),” *Chem. Mater.*, 2019, doi: 10.1021/acs.chemmater.9b02776.

[238] Z. Chen *et al.*, “Overpotential analysis of graphite-based Li-ion batteries seen from a porous electrode modeling perspective,” *J. Power Sources*, vol. 509, p. 230345, Oct. 2021, doi: 10.1016/j.jpowsour.2021.230345.

[239] A. Jossen, “Fundamentals of battery dynamics,” *J. Power Sources*, vol. 154, no. 2, pp. 530–538, Mar. 2006, doi: 10.1016/j.jpowsour.2005.10.041.

[240] J. Vetter *et al.*, “Ageing mechanisms in lithium-ion batteries,” *J. Power Sources*, vol. 147, no. 1–2, pp. 269–281, Sep. 2005, doi: 10.1016/j.jpowsour.2005.01.006.

[241] N. Elgrishi, K. J. Rountree, B. D. McCarthy, E. S. Rountree, T. T. Eisenhart, and J. L. Dempsey, “A Practical Beginner’s Guide to Cyclic Voltammetry,” *J. Chem. Educ.*, vol. 95, no. 2, pp. 197–206, Feb. 2018, doi: 10.1021/ACS.JCHEMED.7B00361/ASSET/IMAGES/LARGE/ED-2017-00361M_0003.JPEG.

[242] E. S. Ameh, “A review of basic crystallography and x-ray diffraction applications,” *Int. J. Adv. Manuf. Technol.*, vol. 105, no. 7–8, pp. 3289–3302, Dec. 2019, doi: 10.1007/s00170-019-04508-1.

[243] M. Henini, “Scanning electron microscopy: An introduction,” *III-Vs Rev.*, vol. 13, no. 4, pp. 40–44, Jul. 2000, doi: 10.1016/S0961-1290(00)80006-X.

[244] W. Zhou, R. Apkarian, Z. L. Wang, and D. Joy, “Fundamentals of scanning electron microscopy (SEM),” in *Scanning Microscopy for Nanotechnology: Techniques and Applications*, Springer New York, 2007, pp. 1–40. doi: 10.1007/978-0-387-39620-0_1.

[245] D. E. Newbury and N. W. M. Ritchie, “Elemental mapping of microstructures by scanning electron microscopy-energy dispersive X-ray spectrometry (SEM-EDS): Extraordinary advances with the silicon drift detector (SDD),” *J. Anal. At. Spectrom.*, vol. 28, no. 7, pp. 973–988, Jun. 2013, doi: 10.1039/c3ja50026h.

[246] Í. Carneiro and S. Simões, “Recent advances in ebsd characterization of metals,” *Metals*, vol. 10, no. 8. Multidisciplinary Digital Publishing Institute, pp. 1–32, Aug. 13, 2020. doi: 10.3390/met10081097.

[247] I. Gutierrez-Urrutia, S. Zaefferer, and D. Raabe, “Coupling of electron channeling with EBSD: Toward the quantitative characterization of deformation structures in the sem,” *JOM*, vol. 65, no. 9, pp. 1229–1236, Sep. 2013, doi: 10.1007/s11837-013-0678-0.

[248] L. N. Brewer, D. P. Field, and C. C. Merriman, “Mapping and assessing plastic deformation using EBSD,” in *Electron Backscatter Diffraction in Materials Science*, Springer US, 2009, pp. 251–262. doi: 10.1007/978-0-387-88136-2_18.

[249] J. D. Andrade, “X-ray Photoelectron Spectroscopy (XPS),” *Surf. Interfacial Asp. Biomed. Polym.*, pp. 105–195, 1985, doi: 10.1007/978-1-4684-8610-0_5.

[250] M. P. Seah, “The quantitative analysis of surfaces by XPS: A review,” *Surf. Interface Anal.*, vol. 2, no. 6, pp. 222–239, Dec. 1980, doi: 10.1002/sia.740020607.

[251] P. S. Bagus, E. S. Ilton, and C. J. Nelin, “The interpretation of XPS spectra: Insights into materials properties,” *Surface Science Reports*, vol. 68, no. 2. North-Holland, pp. 273–304, Jun. 01, 2013. doi: 10.1016/j.surfrep.2013.03.001.

[252] F. J. Santos and M. T. Galceran, “Modern developments in gas chromatography-mass spectrometry-based environmental analysis,” *Journal of Chromatography A*, vol. 1000, no. 1–2. Elsevier, pp. 125–151, Jun. 06, 2003. doi: 10.1016/S0021-9673(03)00305-4.

[253] W. W. Christie, “Gas chromatography-mass spectrometry methods for structural analysis of fatty acids,” *Lipids*, vol. 33, no. 4. Springer, pp. 343–353, 1998. doi: 10.1007/s11745-998-0214-x.

[254] K. Maštovská and S. J. Lehotay, “Practical approaches to fast gas chromatography-mass spectrometry,” *Journal of Chromatography A*, vol. 1000, no. 1–2. Elsevier, pp. 153–180, Jun. 06, 2003. doi: 10.1016/S0021-9673(03)00448-5.

[255] R. A. Oliver, “Advances in AFM for the electrical characterization of semiconductors,” *Reports Prog. Phys.*, vol. 71, no. 7, p. 076501, Jun. 2008, doi: 10.1088/0034-4885/71/7/076501.

[256] T. Ando, “High-speed AFM imaging,” *Current Opinion in Structural Biology*, vol. 28, no. 1. Elsevier Current Trends, pp. 63–68, Oct. 01, 2014. doi: 10.1016/j.sbi.2014.07.011.

[257] N. A. Geisse, “AFM and combined optical techniques,” *Materials Today*, vol. 12, no. 7–8. Elsevier, pp. 40–45, Jul. 01, 2009. doi: 10.1016/S1369-7021(09)70201-9.

[258] L. Gu, N. Wang, X. Tang, and H. G. Changela, “Application of FIB-SEM Techniques for the Advanced Characterization of Earth and Planetary Materials,” *Scanning*, vol. 2020. Hindawi Limited, 2020. doi: 10.1155/2020/8406917.

[259] M. W. Phaneuf, “FIB for materials science applications - A review,” in *Introduction to Focused Ion Beams: Instrumentation, Theory, Techniques and Practice*, Springer US, 2005, pp. 143–172. doi: 10.1007/0-387-23313-X_8.

[260] C. Kizilyaprak, Y. D. Stierhof, and B. M. Humbel, “Volume microscopy in biology: FIB-SEM tomography,” *Tissue and Cell*, vol. 57. Churchill Livingstone, pp. 123–128, Apr. 01, 2019. doi: 10.1016/j.tice.2018.09.006.

[261] P. J. Withers *et al.*, “X-ray computed tomography,” *Nature Reviews Methods Primers*, vol. 1, no. 1. Nature Publishing Group, pp. 1–21, Feb. 25, 2021. doi: 10.1038/s43586-021-00015-4.

[262] V. Wood, “X-ray tomography for battery research and development,” *Nature Reviews Materials*, vol. 3, no. 9. Nature Publishing Group, pp. 293–295, Aug. 28, 2018. doi: 10.1038/s41578-018-0053-4.

[263] L. Zhang and S. Wang, “Correlation of materials property and performance with internal structures evolvement revealed by laboratory X-ray tomography,” *Materials*, vol. 11, no. 10. Multidisciplinary Digital Publishing Institute, p. 1795, Sep. 21, 2018. doi: 10.3390/ma11101795.

[264] T. M. M. Heenan, C. Tan, J. Hack, D. J. L. Brett, and P. R. Shearing, “Developments in X-ray tomography characterization for electrochemical devices,” *Materials Today*, vol. 31. Elsevier, pp. 69–85, Dec. 01, 2019. doi: 10.1016/j.mattod.2019.05.019.

[265] M. J. Williamson, R. M. Tromp, P. M. Vereecken, R. Hull, and F. M. Ross, “Dynamic microscopy of nanoscale cluster growth at the solid–liquid interface,” *Nat. Mater.*, vol. 2, no. 8, pp. 532–536, Aug. 2003, doi: 10.1038/nmat944.

[266] F. M. Ross, J. Tersoff, and M. C. Reuter, “Sawtooth faceting in silicon nanowires,” *Phys. Rev. Lett.*, vol. 95, no. 14, 2005, doi: 10.1103/PhysRevLett.95.146104.

[267] H. Zheng, R. K. Smith, Y. -w. Jun, C. Kisielowski, U. Dahmen, and A. P. Alivisatos, “Observation of Single Colloidal Platinum Nanocrystal Growth Trajectories,” *Science (80-.).*, vol. 324, no. 5932, pp. 1309–1312, Jun. 2009, doi: 10.1126/science.1172104.

[268] H. Zheng, S. A. Claridge, A. M. Minor, A. P. Alivisatos, and U. Dahmen, “Nanocrystal Diffusion in a Liquid Thin Film Observed by in Situ Transmission Electron Microscopy,” *Nano Lett.*, vol. 9, no. 6, pp. 2460–2465, Jun. 2009, doi: 10.1021/nl9012369.

[269] K. Nishijima, J. Yamasaki, H. Orihara, and N. Tanaka, “Development of microcapsules for electron microscopy and their application to dynamical observation of liquid crystals in transmission electron microscopy,” *Nanotechnology*, vol. 15, no. 6, pp. S329–S332, Jun. 2004, doi: 10.1088/0957-4484/15/6/001.

[270] J. E. Evans, K. L. Jungjohann, N. D. Browning, and I. Arslan, “Controlled Growth of Nanoparticles from Solution with In Situ Liquid Transmission Electron Microscopy,” *Nano Lett.*, vol. 11, no. 7, pp. 2809–2813, Jul. 2011, doi: 10.1021/nl201166k.

[271] D. F. Parsons, V. R. Matricardi, R. C. Moretz, and J. N. Turner, “Electron Microscopy and Diffraction of Wet Unstained and Unfixed Biological Objects,” in *Advances in Biological and Medical Physics*, vol. 15, 1974, pp. 161–270. doi: 10.1016/B978-0-12-005215-8.50012-7.

[272] N. d. Jonge, D. B. Peckys, G. J. Kremers, and D. W. Piston, “Electron microscopy of whole cells in liquid with nanometer resolution,” *Proc. Natl. Acad. Sci.*, vol. 106, no. 7, pp. 2159–2164, Feb. 2009, doi: 10.1073/pnas.0809567106.

[273] T. L. Daulton, B. J. Little, K. Lowe, and J. Jones-Meehan, “In Situ Environmental Cell-Transmission Electron Microscopy Study of Microbial Reduction of Chromium(VI) Using Electron Energy Loss Spectroscopy.,” *Microsc. Microanal.*, vol. 7, no. 6, pp. 470–485, 2001, doi: 10.1017.S1431927601010467.

[274] N. Mohanty, M. Fahrenholtz, A. Nagaraja, D. Boyle, and V. Berry, “Impermeable Graphenic Encasement of Bacteria,” *Nano Lett.*, vol. 11, no. 3, pp. 1270–1275, Mar. 2011, doi: 10.1021/nl104292k.

[275] D. B. Peckys and N. De Jonge, “Visualizing gold nanoparticle uptake in live cells with liquid scanning transmission electron microscopy,” *Nano Lett.*, vol. 11, no. 4, pp. 1733–1738, 2011, doi: 10.1021/nl200285r.

[276] D. B. Peckys, P. Mazur, K. L. Gould, and N. De Jonge, “Fully hydrated yeast cells imaged with electron microscopy,” *Biophys. J.*, vol. 100, no. 10, pp. 2522–2529, May 2011, doi: 10.1016/j.bpj.2011.03.045.

[277] C.-M. Wang, “In situ transmission electron microscopy and spectroscopy studies of rechargeable batteries under dynamic operating conditions: A retrospective and perspective view,” *J. Mater. Res.*, vol. 30, no. 3, pp. 326–339, 2015, doi: 10.1557/jmr.2014.281.

[278] R. L. Sacci *et al.*, “Direct visualization of initial SEI morphology and growth kinetics during lithium deposition by in situ electrochemical transmission electron microscopy,” *Chem. Commun.*, vol. 50, no. 17, pp. 2104–2107, Jan. 2014, doi: 10.1039/c3cc49029g.

[279] Z. Zeng, W. I. Liang, H. G. Liao, H. L. Xin, Y. H. Chu, and H. Zheng, “Visualization of electrode-electrolyte interfaces in LiPF 6/EC/DEC electrolyte for lithium ion batteries via in situ TEM,” *Nano Lett.*, vol. 14, no. 4, pp. 1745–1750, Apr. 2014, doi: 10.1021/nl403922u.

[280] S. W. Chee, S. H. Pratt, K. Hattar, D. Duquette, F. M. Ross, and R. Hull, “Studying localized corrosion using liquid cell transmission electron microscopy,” *Chem. Commun.*, vol. 51, no. 1, pp. 168–171, Dec. 2015, doi: 10.1039/c4cc06443g.

[281] S. W. Chee, D. J. Duquette, F. M. Ross, and R. Hull, “Metastable Structures in Al Thin Films Before the Onset of Corrosion Pitting as Observed using Liquid Cell Transmission Electron Microscopy,” *Microsc. Microanal.*, vol. 20, no. 2, pp. 462–468, 2014, doi: 10.1017/s1431927614000221.

[282] H. G. Liao, K. Niu, and H. Zheng, “Observation of growth of metal nanoparticles,” *Chem. Commun.*, vol. 49, no. 100, pp. 11720–11727, 2013, doi: 10.1039/c3cc47473a.

[283] K. L. Jungjohann, J. E. Evans, J. A. Aguiar, I. Arslan, and N. D. Browning, “Atomic-Scale Imaging and Spectroscopy for In Situ Liquid Scanning Transmission Electron Microscopy,” *Microsc. Microanal.*, vol. 18, pp. 621–627, 2012, doi: 10.1017/S1431927612000104.

[284] E. A. Lewis *et al.*, “Real-time imaging and local elemental analysis of nanostructures in liquids,” *Chem. Commun.*, vol. 50, no. 70, pp. 10019–10022, 2014, doi: 10.1039/c4cc02743d.

[285] J. M. Howe and H. Saka, “In situ transmission electron microscopy studies of the solid-liquid interface,” *MRS Bull.*, vol. 29, no. 12, pp. 951–957, Dec. 2004, doi: 10.1557/mrs2004.266.

[286] S. K. Eswaramoorthy, J. M. Howe, and G. Muralidharan, “In situ determination of the nanoscale chemistry and behavior of solid-liquid systems,” *Science (80-.).*, vol. 318, no. 5855, pp. 1437–1440, Nov. 2007, doi: 10.1126/science.1146511.

[287] J.-G. Lee and H. Mori †, “In-situ observation of alloy phase formation in nanometre-sized particles in the Sn–Bi system,” *Philos. Mag.*, vol. 84, no. 25–26, pp. 2675–2686, Sep. 2004, doi: 10.1080/14786430410001671421.

[288] J. Y. Huang *et al.*, “In Situ Observation of the Electrochemical Lithiation of a Single SnO 2 Nanowire Electrode,” *Science (80-.).*, vol. 330, no. 6010, pp. 1515–1520, Dec. 2010, doi: 10.1126/science.1195628.

[289] T. W. Hansen, J. B. Wagner, and R. E. Dunin-Borkowski, “Aberration corrected and monochromated environmental transmission electron microscopy: challenges and prospects for materials science,” *Mater. Sci. Technol.*, vol. 26, no. 11, pp. 1338–1344, 2010, doi: 10.1179/026708310x12756557336355.

[290] L. L. Dai, R. Sharma, and C. Wu, “Self-Assembled Structure of Nanoparticles at a Liquid−Liquid Interface,” *Langmuir*, vol. 21, no. 7, pp. 2641–2643, Mar. 2005, doi: 10.1021/la047256t.

[291] T. Miyata and T. Mizoguchi, “Fabrication of thin TEM sample of ionic liquid for high-resolution ELNES measurements,” *Ultramicroscopy*, vol. 178, pp. 81–87, Jul. 2017, doi: 10.1016/j.ultramic.2016.10.009.

[292] C. M. Wang *et al.*, "In situ transmission electron microscopy and spectroscopy studies of interfaces in Li ion batteries: Challenges and opportunities," *J. Mater. Res.*, vol. 25, no. 8, pp. 1541–1547, Aug. 2010, doi: 10.1557/jmr.2010.0198.

[293] J. M. Yuk, H. K. Seo, J. W. Choi, and J. Y. Lee, "Anisotropic lithiation onset in silicon nanoparticle anode revealed by in situ graphene liquid cell electron microscopy," *ACS Nano*, vol. 8, no. 7, pp. 7478–7485, 2014, doi: 10.1021/nn502779n.

[294] K.-L. Liu *et al.*, "Novel microchip for in situ TEM imaging of living organisms and bio-reactions in aqueous conditions," *Lab Chip*, vol. 8, no. 11, p. 1915, 2008, doi: 10.1039/b804986f.

[295] E. A. Ring and N. de Jonge, "Microfluidic System for Transmission Electron Microscopy," *Microsc. Microanal.*, vol. 16, no. 5, pp. 622–629, Oct. 2010, doi: 10.1017/s1431927610093669.

[296] K. Tai, Y. Liu, and S. J. Dillon, "In Situ Cryogenic Transmission Electron Microscopy for Characterizing the Evolution of Solidifying Water Ice in Colloidal Systems," *Microsc. Microanal.*, vol. 20, no. 2, pp. 330–337, Apr. 2014, doi: 10.1017/S1431927613014128.

[297] T. J. Woehl, J. E. Evans, I. Arslan, W. D. Ristenpart, and N. D. Browning, "Direct in situ determination of the mechanisms controlling nanoparticle nucleation and growth," *ACS Nano*, vol. 6, no. 10, pp. 8599–8610, 2012, doi: 10.1021/nn303371y.

[298] Dongsheng Li, M. H. Nielsen, J. R. I. Lee, C. Frandsen, J. F. Banfield, and J. J. De Yoreo, "Direction-Specific Interactions Control Crystal Growth by Oriented Attachment," *Science*, vol. 336, pp. 1014–1018, Aug. 2012, doi: 10.1126/science.289.5480.751.

[299] H. G. Liao, L. Cui, S. Whitelam, and H. Zheng, "Real-time imaging of Pt3Fe nanorod growth in solution," *Science (80-.).*, vol. 336, no. 6084, pp. 1011–1014, May 2012, doi: 10.1126/science.1219185.

[300] K. L. Jungjohann, S. Bliznakov, P. W. Sutter, E. A. Stach, and E. A. Sutter, “In situ liquid cell electron microscopy of the solution growth of Au-Pd core-shell nanostructures,” *Nano Lett.*, vol. 13, no. 6, pp. 2964–2970, 2013, doi: 10.1021/nl4014277.

[301] Y. Jiang *et al.*, “In situ study of oxidative etching of palladium nanocrystals by liquid cell electron microscopy,” *Nano Lett.*, vol. 14, no. 7, pp. 3761–3765, 2014, doi: 10.1021/nl500670q.

[302] D. Alloyeau *et al.*, “Unravelling Kinetic and Thermodynamic Effects on the Growth of Gold Nanoplates by Liquid Transmission Electron Microscopy,” *Nano Lett.*, vol. 15, no. 4, pp. 2574–2581, 2015, doi: 10.1021/acs.nanolett.5b00140.

[303] W. I. Liang *et al.*, “In Situ Study of Fe 3 Pt-Fe 2 O 3 Core-Shell Nanoparticle Formation,” *J. Am. Chem. Soc.*, vol. 137, no. 47, pp. 14850–14853, 2015, doi: 10.1021/jacs.5b10076.

[304] J. Wu *et al.*, “Growth of Au on Pt Icosahedral Nanoparticles Revealed by Low-Dose in Situ TEM,” *Nano Lett.*, vol. 15, no. 4, pp. 2711–2715, 2015, doi: 10.1021/acs.nanolett.5b00414.

[305] M. Ge, M. Lu, Y. Chu, and H. Xin, “Anomalous Growth Rate of Ag Nanocrystals Revealed by in situ STEM,” *Sci. Rep.*, vol. 7, no. 1, p. 16420, Dec. 2017, doi: 10.1038/s41598-017-15140-y.

[306] J. Wu, W. Gao, H. Yang, and J.-M. Zuo, “Imaging Shape-Dependent Corrosion Behavior of Pt Nanoparticles over Extended Time Using a Liquid Flow Cell and TEM,” *Microsc. Microanal.*, vol. 20, pp. 1508–1509, 2014, doi: 10.1017/S1431927614009271.

[307] J. Wu, W. Gao, H. Yang, and J. M. Zuo, “Dissolution Kinetics of Oxidative Etching of Cubic and Icosahedral Platinum Nanoparticles Revealed by in Situ Liquid Transmission Electron Microscopy,” *ACS Nano*, vol. 11, no. 2, pp. 1696–1703, 2017, doi: 10.1021/acsnano.6b07541.

[308] M. J. Dukes, D. B. Peckys, and N. De Jonge, “Correlative fluorescence microscopy and scanning transmission electron microscopy of quantum-dot-labeled proteins in whole cells in liquid,” *ACS Nano*, vol. 4, no. 7, pp. 4110–4116, 2010, doi: 10.1021/nn1010232.

[309] N. De Jonge and D. B. Peckys, “Live Cell Electron Microscopy Is Probably Impossible,” *ACS Nano*, vol. 10, no. 10, pp. 9061–9063, 2016, doi: 10.1021/acsnano.6b02809.

[310] D. B. Peckys and N. de Jonge, “Liquid Scanning Transmission Electron Microscopy: Imaging Protein Complexes in their Native Environment in Whole Eukaryotic Cells,” *Microsc. Microanal.*, vol. 20, no. 2, pp. 346–365, 2014, doi: 10.1017/s1431927614000099.

[311] E. S. Pohlmann, K. Patel, S. Guo, M. J. Dukes, Z. Sheng, and D. F. Kelly, “Real-Time Visualization of Nanoparticles Interacting with Glioblastoma Stem Cells,” *Nano Lett.*, vol. 15, no. 4, pp. 2329–2335, 2015, doi: 10.1021/nl504481k.

[312] V. Beermann, M. E. Holtz, E. Padgett, J. Ferreira de Araujo, D. A. Muller, and P. Strasser, “Real-time Imaging of Activation and Degradation of Carbon Supported Octahedral Pt-Ni Alloy Fuel Cell Catalysts at the Nanoscale Using in situ Electrochemical Liquid Cell STEM,” *Energy Environ. Sci.*, 2019, doi: 10.1039/c9ee01185d.

[313] Z. W. Yin *et al.*, “Visualization of facet-dependent pseudo-photocatalytic behavior of TiO2 nanorods for water splitting using In situ liquid cell TEM,” *Nano Energy*, vol. 62, pp. 507–512, Aug. 2019, doi: 10.1016/j.nanoen.2019.05.068.

[314] Z. Zeng, W. I. Liang, Y. H. Chu, and H. Zheng, “In situ TEM study of the Li-Au reaction in an electrochemical liquid cell,” *Faraday Discuss.*, vol. 176, pp. 95–107, 2014, doi: 10.1039/c4fd00145a.

[315] J. Qian *et al.*, “Dendrite-free Li deposition using trace-amounts of water as an electrolyte additive,” *Nano Energy*, vol. 15, pp. 135–144, Jul. 2015, doi: 10.1016/j.nanoen.2015.04.009.

[316] J. H. Park, N. M. Schneider, D. A. Steingart, H. Deligianni, S. Kodambaka, and F. M. Ross, “Control of Growth Front Evolution by Bi Additives during ZnAu Electrodeposition,” *Nano Lett.*, vol. 18, no. 2, pp. 1093–1098, 2018, doi: 10.1021/acs.nanolett.7b04640.

[317] B. L. Mehdi *et al.*, “Understanding the Effect of Additives in Li-Sulfur Batteries by Operando ec-(S)TEM,” *Microsc. Microanal.*, vol. 22, no. S3, pp. 836–837, Jul. 2016, doi: 10.1017/S143192761600502X.

[318] B. L. Mehdi *et al.*, “The Impact of Li Grain Size on Coulombic Efficiency in Li Batteries,” *Sci. Rep.*, vol. 6, 2016, doi: 10.1038/srep34267.

[319] B. L. Mehdi *et al.*, “Multi-Modal Characterization of New Battery Technologies by Operando ec-STEM,” *Microsc. Microanal.*, vol. 23, no. S1, pp. 886–887, 2017, doi: 10.1017/s1431927617005098.

[320] T. Zhang *et al.*, “Fundamentals and perspectives in developing zinc-ion battery electrolytes: A comprehensive review,” *Energy and Environmental Science*, vol. 13, no. 12. Royal Society of Chemistry, pp. 4625–4665, Dec. 16, 2020. doi: 10.1039/d0ee02620d.

[321] C. Liu, X. Xie, B. Lu, J. Zhou, and S. Liang, “Electrolyte Strategies toward Better Zinc-Ion Batteries,” *ACS Energy Lett.*, vol. 6, no. 3, pp. 1015–1033, 2021, doi: 10.1021/acsenergylett.0c02684.

[322] W. Lu, C. Zhang, H. Zhang, and X. Li, “Anode for Zinc-Based Batteries: Challenges, Strategies, and Prospects,” *ACS Energy Lett.*, vol. 6, no. 8, pp. 2765–2785, 2021, doi: 10.1021/acsenergylett.1c00939.

[323] L. Ma *et al.*, “Initiating a mild aqueous electrolyte Co3O4/Zn battery with 2.2 V-high voltage and 5000-cycle lifespan by a Co(iii) rich-electrode,” *Energy Environ. Sci.*, vol. 11, no. 9, pp. 2521–2530, Sep. 2018, doi: 10.1039/c8ee01415a.

[324] B. Tang, L. Shan, S. Liang, and J. Zhou, “Issues and opportunities facing aqueous zinc-ion batteries,” *Energy and Environmental Science*, vol. 12, no. 11. Royal Society of Chemistry, pp. 3288–3304, Nov. 01, 2019. doi: 10.1039/c9ee02526j.

[325] L. E. Blanc, D. Kundu, and L. F. Nazar, “Scientific Challenges for the Implementation of Zn-Ion Batteries,” *Joule*, vol. 4, no. 4. Cell Press, pp. 771–799, Apr. 15, 2020. doi: 10.1016/j.joule.2020.03.002.

[326] V. P. H. Huy, L. T. Hieu, and J. Hur, “Zn metal anodes for Zn-ion batteries in mild aqueous electrolytes: Challenges and strategies,” *Nanomaterials*, vol. 11, no. 10, 2021, doi: 10.3390/nano11102746.

[327] J. Xiao *et al.*, “Understanding and applying coulombic efficiency in lithium metal batteries,” *Nat. Energy*, vol. 5, no. 8, pp. 561–568, Aug. 2020, doi: 10.1038/s41560-020-0648-z.

[328] A. A. Sagüés and R. G. Powers, “Sprayed-Zinc Sacrificial Anodes for Reinforced Concrete in Marine Service,” *Corrosion*, vol. 52, no. 7, pp. 508–522, Jul. 1996, doi: 10.5006/1.3292141.

[329] A. Farooq, M. Hamza, Q. Ahmed, and K. M. Deen, “Evaluating the performance of zinc and aluminum sacrificial anodes in artificial seawater,” *Electrochim. Acta*, vol. 314, pp. 135–141, Aug. 2019, doi: 10.1016/j.electacta.2019.05.067.

[330] H. Wang, M. Du, H. Liang, and Q. Gao, “Study on Al-Zn-In Alloy as Sacrificial Anodes in Seawater Environment,” *J. Ocean Univ. China*, vol. 18, no. 4, pp. 889–895, Jul. 2019, doi: 10.1007/s11802-019-3788-7.

[331] M. SADAWY, S. SAAD, and R. ABDEL-KARIM, “Effect of Zn/Mg ratio on cathodic protection of carbon steel using Al–Zn–Mg sacrificial anodes,” *Trans. Nonferrous Met. Soc. China (English Ed.*, vol. 30, no. 8, pp. 2067–2078, Aug. 2020, doi: 10.1016/S1003-6326(20)65361-4.

[332] H. Glatz, E. Tervoort, and D. Kundu, “Unveiling Critical Insight into the Zn Metal Anode Cyclability in Mildly Acidic Aqueous Electrolytes: Implications for Aqueous Zinc Batteries,” *ACS Appl. Mater. Interfaces*, vol. 12, no. 3, pp. 3522–3530, Jan. 2020, doi: 10.1021/acsami.9b16125.

[333] C. Jin *et al.*, “Rejuvenating dead lithium supply in lithium metal anodes by iodine redox,” *Nat. Energy*, vol. 6, no. 4, pp. 378–387, Mar. 2021, doi: 10.1038/s41560-021-00789-7.

[334] K. H. Chen *et al.*, “Dead lithium: Mass transport effects on voltage, capacity, and failure of lithium metal anodes,” *J. Mater. Chem. A*, vol. 5, no. 23, pp. 11671–11681, Jun. 2017, doi: 10.1039/c7ta00371d.

[335] H. Sun *et al.*, “In Situ Visualization of Lithium Penetration through Solid Electrolyte and Dead Lithium Dynamics in Solid-State Lithium Metal Batteries,” *ACS Nano*, vol. 15, no. 12, pp. 19070–19079, Dec. 2021, doi: 10.1021/acsnano.1c04864.

[336] C. Gong *et al.*, “Revealing the Role of Fluoride-Rich Battery Electrode Interphases by Operando Transmission Electron Microscopy,” *Adv. Energy Mater.*, vol. 11, no. 10, p. 2003118, Mar. 2021, doi: 10.1002/aenm.202003118.

[337] J. Guo *et al.*, “Artificial Solid Electrolyte Interphase for Suppressing Surface Reactions and Cathode Dissolution in Aqueous Zinc Ion Batteries,” *ACS Energy Lett.*, vol. 4, no. 12, pp. 2776–2781, 2019, doi: 10.1021/acsenergylett.9b02029.

[338] S. Guo *et al.*, “Fundamentals and perspectives of electrolyte additives for aqueous zinc-ion batteries,” *Energy Storage Mater.*, vol. 34, no. September 2020, pp. 545–562, 2021, doi: 10.1016/j.ensm.2020.10.019.

[339] Y. Li *et al.*, “A progressive nucleation mechanism enables stable zinc stripping-plating behavior,” *Energy Environ. Sci.*, vol. 14, no. 10, pp. 5563–5571, 2021, doi: 10.1039/d1ee01861b.

[340] Q. Han *et al.*, “Durable, flexible self-standing hydrogel electrolytes enabling high-safety rechargeable solid-state zinc metal batteries,” *J. Mater. Chem. A*, vol. 6, no. 45, pp. 23046–23054, Nov. 2018, doi: 10.1039/c8ta08314b.

[341] Q. Han *et al.*, “An inorganic salt reinforced Zn2+-conducting solid-state electrolyte for ultra-stable Zn metal batteries,” *J. Mater. Chem. A*, vol. 7, no. 39, pp. 22287–22295, Oct. 2019, doi: 10.1039/c9ta07218g.

[342] B. Wang, J. Li, C. Hou, Q. Zhang, Y. Li, and H. Wang, “Stable Hydrogel Electrolytes for Flexible and Submarine-Use Zn-Ion Batteries,” *ACS Appl. Mater. Interfaces*, vol. 12, no. 41, pp. 46005–46014, Oct. 2020, doi: 10.1021/acsami.0c12313.

[343] H. Zhang, X. Liu, H. Li, B. Qin, and S. Passerini, “High-Voltage Operation of a V2O5 Cathode in a Concentrated Gel Polymer Electrolyte for High-Energy Aqueous Zinc Batteries,” *ACS Appl. Mater. Interfaces*, vol. 12, no. 13, pp. 15305–15312, Apr. 2020, doi: 10.1021/acsami.0c02102.

[344] L. Ma *et al.*, “Hydrogen-Free and Dendrite-Free All-Solid-State Zn-Ion Batteries,” *Adv. Mater.*, vol. 32, no. 14, p. 1908121, Apr. 2020, doi: 10.1002/adma.201908121.

[345] *Surface and Interface Science*. Wiley-VCH Verlag GmbH & Co. KGaA, 2013. doi: 10.1002/9783527680566.

[346] S. J. Banik and R. Akolkar, “Suppressing Dendrite Growth during Zinc Electrodeposition by PEG-200 Additive,” *J. Electrochem. Soc.*, vol. 160, no. 11, pp. D519–D523, Sep. 2013, doi: 10.1149/2.040311jes.

[347] T. Otani, Y. Fukunaka, and T. Homma, “Effect of lead and tin additives on surface morphology evolution of electrodeposited zinc,” *Electrochim. Acta*, vol. 242, pp. 364–372, Jul. 2017, doi: 10.1016/j.electacta.2017.04.130.

[348] Z. Liu *et al.*, “Dendrite-Free Nanocrystalline Zinc Electrodeposition from an Ionic Liquid Containing Nickel Triflate for Rechargeable Zn-Based Batteries,” *Angew. Chemie - Int. Ed.*, vol. 55, no. 8, pp. 2889–2893, Feb. 2016, doi: 10.1002/anie.201509364.

[349] J. Abdulla *et al.*, “Elimination of Zinc Dendrites by Graphene Oxide Electrolyte Additive for Zinc-Ion Batteries,” *ACS Appl. Energy Mater.*, vol. 4, no. 5, pp. 4602–4609, May 2021, doi: 10.1021/acsaem.1c00224.

[350] A. Bayaguud, X. Luo, Y. Fu, and C. Zhu, “Cationic surfactant-type electrolyte additive enables three-dimensional dendrite-free zinc anode for stable zinc-ion batteries,” *ACS Energy Lett.*, vol. 5, no. 9, pp. 3012–3020, Sep. 2020, doi: 10.1021/acsenergylett.0c01792.

[351] Z. Kang *et al.*, “3D Porous Copper Skeleton Supported Zinc Anode toward High Capacity and Long Cycle Life Zinc Ion Batteries,” *ACS Sustain. Chem. Eng.*, vol. 7, no. 3, pp. 3364–3371, Feb. 2019, doi: 10.1021/acssuschemeng.8b05568.

[352] Z. Yan, E. Wang, L. Jiang, and G. Sun, “Superior cycling stability and high rate capability of three-dimensional Zn/Cu foam electrodes for zinc-based alkaline batteries,” *RSC Adv.*, vol. 5, no. 102, pp. 83781–83787, Oct. 2015, doi: 10.1039/c5ra16264e.

[353] J. F. Parker, C. N. Chervin, E. S. Nelson, D. R. Rolison, and J. W. Long, “Wiring zinc in three dimensions re-writes battery performance - Dendrite-free cycling,” *Energy Environ. Sci.*, vol. 7, no. 3, pp. 1117–1124, Feb. 2014, doi: 10.1039/c3ee43754j.

[354] J. Zheng and L. A. Archer, “Controlling electrochemical growth of metallic zinc electrodes: Toward affordable rechargeable energy storage systems,” *Science Advances*, vol. 7, no. 2. p. eabe0219, Jan. 2021. doi: 10.1126/sciadv.abe0219.

[355] V. N. Perevezentsev, V. V. Rybin, and V. N. Chuvil’deev, “The theory of structural superplasticity-II. Accumulation of defects on the intergranular and interphase boundaries. Accomodation of the grain-boundary sliding. The upper bound of the superplastic strain rate,” *Acta Metall. Mater.*, vol. 40, no. 5, pp. 895–905, May 1992, doi: 10.1016/0956-7151(92)90066-N.

[356] B. Kuhr, D. Farkas, I. M. Robertson, D. Johnson, and G. Was, “Stress Localization Resulting from Grain Boundary Dislocation Interactions in Relaxed and Defective Grain Boundaries,” *Metall. Mater. Trans. A Phys. Metall. Mater. Sci.*, vol. 51, no. 2, pp. 667–683, Feb. 2020, doi: 10.1007/s11661-019-05534-0.

[357] B. N. Singh and S. J. Zinkle, “Defect accumulation in pure fcc metals in the transient regime: a review,” *J. Nucl. Mater.*, vol. 206, no. 2–3, pp. 212–229, Nov. 1993, doi: 10.1016/0022-3115(93)90125-I.

[358] B. P. Uberuaga, L. J. Vernon, E. Martinez, and A. F. Voter, “The relationship between grain boundary structure, defect mobility, and grain boundary sink efficiency,” *Sci. Rep.*, vol. 5, no. 1, pp. 1–9, Mar. 2015, doi: 10.1038/srep09095.

[359] J. Steiger, D. Kramer, and R. Mönig, “Mechanisms of dendritic growth investigated by in situ light microscopy during electrodeposition and dissolution of lithium,” *J. Power Sources*, vol. 261, pp. 112–119, Sep. 2014, doi: 10.1016/j.jpowsour.2014.03.029.

[360] K. J. Harry, D. T. Hallinan, D. Y. Parkinson, A. A. MacDowell, and N. P. Balsara, “Detection of subsurface structures underneath dendrites formed on cycled lithium metal electrodes,” *Nat. Mater.*, vol. 13, no. 1, pp. 69–73, Nov. 2014, doi: 10.1038/nmat3793.

[361] T. Hurlen, K. Schrøder, R. Havanka, T. Briggs, G. A. D. Haslewood, and H. Flood, “Corrosion of Zinc. Effect of pH.,” *Acta Chem. Scand.*, vol. 16, pp. 1346–1352, 1962, doi: 10.3891/acta.chem.scand.16-1346.

[362] T. Nishinaga, *Handbook of Crystal Growth: Bulk Crystal Growth: Second Edition*, vol. 2. Elsevier Inc., 2014. doi: 10.1016/C2013-0-09791-5.

[363] M. Chamoun *et al.*, “Hyper-dendritic nanoporous zinc foam anodes,” *NPG Asia Mater.*, vol. 7, no. 4, pp. e178–e178, Apr. 2015, doi: 10.1038/am.2015.32.

[364] Z. Ning *et al.*, “Visualizing plating-induced cracking in lithium-anode solid-electrolyte cells,” *Nat. Mater.*, pp. 1–9, Apr. 2021, doi: 10.1038/s41563-021-00967-8.

[365] R. Davidson *et al.*, “Formation of Magnesium Dendrites during Electrodeposition,” *ACS Energy Lett.*, vol. 4, no. 2, pp. 375–376, Feb. 2019, doi: 10.1021/acsenergylett.8b02470.

[366] W. Xiong *et al.*, “Controlling the sustainability and shape change of the zinc anode in rechargeable aqueous Zn/LiMn2O4 battery,” *Energy Storage Mater.*, vol. 15, pp. 131–138, Nov. 2018, doi: 10.1016/j.ensm.2018.03.023.

[367] H. D. Yoo, I. Shterenberg, Y. Gofer, G. Gershinsky, N. Pour, and D. Aurbach, “Mg rechargeable batteries: An on-going challenge,” *Energy and Environmental Science*, vol. 6, no. 8. pp. 2265–2279, Aug. 2013. doi: 10.1039/c3ee40871j.

[368] S. B. Son *et al.*, “An artificial interphase enables reversible magnesium chemistry in carbonate electrolytes,” *Nat. Chem.*, vol. 10, no. 5, pp. 532–539, May 2018, doi: 10.1038/s41557-018-0019-6.

[369] D. Aurbach, Y. Cohen, and M. Moshkovich, “The study of reversible magnesium deposition by in situ scanning tunneling microscopy,” *Electrochem. Solid-State Lett.*, vol. 4, no. 8, Aug. 2001, doi: 10.1149/1.1379828.

[370] M. Matsui, “Study on electrochemically deposited Mg metal,” *J. Power Sources*, vol. 196, no. 16, pp. 7048–7055, Aug. 2011, doi: 10.1016/j.jpowsour.2010.11.141.

[371] X. Yu and A. Manthiram, “Performance Enhancement and Mechanistic Studies of Magnesium-Sulfur Cells with an Advanced Cathode Structure,” *ACS Energy Lett.*, vol. 1, no. 2, pp. 431–437, Aug. 2016, doi: 10.1021/acsenergylett.6b00213.

[372] E. N. Keyzer *et al.*, “Mg(PF6)2-Based Electrolyte Systems: Understanding Electrolyte-Electrode Interactions for the Development of Mg-Ion Batteries,” *J. Am. Chem. Soc.*, vol. 138, no. 28, pp. 8682–8685, Jul. 2016, doi: 10.1021/jacs.6b04319.

[373] P. Canepa *et al.*, “Odyssey of Multivalent Cathode Materials: Open Questions and Future Challenges,” *Chem. Rev.*, vol. 117, no. 5, pp. 4287–4341, Mar. 2017, doi: 10.1021/acs.chemrev.6b00614.

[374] R. J. Staniewicz, “A Study of the Calcium-Thionyl Chloride Electrochemical System,” *J. Electrochem. Soc.*, vol. 127, no. 4, pp. 782–789, 1980, doi: 10.1149/1.2129758.

[375] A. Meitav and E. Peled, “Calcium-Ca(AICI4)2-Thionyl Chloride Cell: Performance and Safety,” *J. Electrochem. Soc.*, vol. 129, no. 3, pp. 451–457, 1982, doi: 10.1149/1.2123879.

[376] M. Shakourian-Fard, G. Kamath, S. M. Taimoory, and J. F. Trant, “Calcium-Ion Batteries: Identifying Ideal Electrolytes for Next-Generation Energy Storage Using Computational Analysis,” *J. Phys. Chem. C*, vol. 123, no. 26, pp. 15885–15896, Jul. 2019, doi: 10.1021/acs.jpcc.9b01655.

[377] A. Ponrouch and M. R. Palacin, “On the road toward calcium-based batteries,” *Current Opinion in Electrochemistry*, vol. 9. Elsevier B.V., pp. 1–7, Jun. 01, 2018. doi: 10.1016/j.coelec.2018.02.001.

[378] N. Sa *et al.*, “Concentration dependent electrochemical properties and structural analysis of a simple magnesium electrolyte: magnesium bis(trifluoromethane sulfonyl)imide in diglyme,” *RSC Adv.*, vol. 6, no. 114, pp. 113663–113670, 2016, doi: 10.1039/c6ra22816j.

[379] R. R. Unocic *et al.*, “Quantitative electrochemical measurements using in situ ec-S/TEM devices,” *Microsc. Microanal.*, vol. 20, no. 2, pp. 452–461, Apr. 2014, doi: 10.1017/S1431927614000166.

[380] R. F. Egerton, P. Li, and M. Malac, “Radiation damage in the TEM and SEM,” in *Micron*, Aug. 2004, vol. 35, no. 6, pp. 399–409. doi: 10.1016/j.micron.2004.02.003.

[381] S. Pu, C. Gong, and A. W. Robertson, “Liquid cell transmission electron microscopy and its applications,” *R. Soc. Open Sci.*, vol. 7, no. 1, p. 191204, 2020, doi: 10.1098/rsos.191204.

[382] E. R. White *et al.*, “In situ transmission electron microscopy of lead dendrites and lead ions in aqueous solution,” *ACS Nano*, vol. 6, no. 7, pp. 6308–6317, 2012, doi: 10.1021/nn3017469.

[383] N. M. Schneider, J. H. Park, J. M. Grogan, D. A. Steingart, H. H. Bau, and F. M. Ross, “Nanoscale evolution of interface morphology during electrodeposition,” *Nat. Commun.*, vol. 8, no. 1, p. 2174, Dec. 2017, doi: 10.1038/s41467-017-02364-9.

[384] T. Kraus and N. De Jonge, “Dendritic gold nanowire growth observed in liquid with transmission electron microscopy,” *Langmuir*, vol. 29, no. 26, pp. 8427–8432, 2013, doi: 10.1021/la401584z.

[385] B. Song *et al.*, “Dynamic Lithium Distribution upon Dendrite Growth and Shorting Revealed by Operando Neutron Imaging,” *ACS Energy Lett.*, vol. 4, no. 10, pp. 2402–2408, Oct. 2019, doi: 10.1021/acsenergylett.9b01652.

[386] A. Radisic, F. M. Ross, and P. C. Searson, “In Situ Study of the Growth Kinetics of Individual Island Electrodeposition of Copper,” *J. Phys. Chem. B*, vol. 110, no. 15, pp. 7862–7868, Apr. 2006, doi: 10.1021/jp057549a.

[387] F. M. Ross, “Opportunities and challenges in liquid cell electron microscopy,” *Science (80-.).*, vol. 350, no. 6267, p. 1490, 2015, doi: 10.1126/science.aaa9886.